UTPP–36

Measurement of Jet Fragmentation Properties in $\bar{p}p$ Collisions at $\sqrt{s} = 1.8$ TeV

June 1990

SHUN–ICHI KANDA

Submitted in partial fulfillment of the requitements
for the Degree of Doctor of Science
in the Doctoral program in
University of Tsukuba

Abstract

The fragmentation properties of jets in $\bar{p}p$ collisions at $\sqrt{s} = 1.8$ TeV have been studied by the CDF experiment at Fermilab. A method based on the QCD-inspired fragmentation models is proposed for the experimental distinction of two types of partons–quarks and gluons. A number of variables, such as mechanical/electric moments, multiplicity, and EM fraction, are calculated for Monte Carlo (reference) jets. Their resulting distributions suggest that gluon jets are softer and broader than quark jets, reflecting the nature of the double color charge of the gluon. The reference jets are compared with real dijet events of the CDF experiment. The real data show strong preference for gluon-like behaviour. This is consistent with the QCD prediction: The gluon jet is dominant at the CDF energy.

In order to integrate the information on variables of jets, each jet is characterized in global likelihood which is a simple sum of all log-likelihood functions derived from 30 different variables. This results in a bigger quark/gluon discrimination power than that of a single most effective variable. The global likelihood for real dijet events are distributed much like gluons, and that for γ_{cand}+jet events, in which the jet is associated with a photon candidate, are distributed like the mixture of gluons and quarks.

The gluon fraction in a given sample is determined by fitting its global likelihood distribution to the superposition of two distributions for quark and gluon samples. The CDF dijet data shows approximately 80% gluon fraction, and the γ_{cand}+jet data shows about 40% gluon fraction in the jet transverse energy (E_t) range of 10–30 GeV. These results agree within the error with the gluon fraction determined from theoretical prediction and the expected π^0/γ ratio in the CDF photon candidates, except that some disagreement for dijet event is observed at low energy.

To my father and mother

Acknowledgement

I would like to acknowledge to University of Tsukuba High Energy Physics group for their help. In particular I would like to thank my advisor, Prof. Kondo, for giving me the opportunity to work on CDF and suggesting the topic of this analysis. He has excited my academic curiosity and always guided me in the right direction. Without his support and encouragement, this thesis would not have been possible. There is Dr. Kim who got me involved in the PEM calorimeter works and jet physics. He taught me not only how to build and test chambers and also how to play hooky from school. I also thank Dr. Mishina and Dr. Fukui for their great help in maintenance and beam test of chambers.

I wish to acknowledge the contributions of the CDF Jet group. I have been especially benefitted from the works of Dave Brown, Steve Kuhlmann, Tim Hessing, Brad Hubbard, and Marge Shapiro. I also thank John Huth for valuable suggestions and encouragement. My deep thanks go to the members of the CDF Tracking group. My analysis relied heavily on their careful studies of track reconstruction. In particular Adam Para and Aesook Byon have been helpful in teaching me good solutions when I got into trouble. I also thank co-workers of the CDF Gas-gain group. It has been pleasure to work with them. There is Melissa Franklin who is a bigwig of the Gas-gain group. She often gave me a good suggestion and a heavy blow.

I would like to thank Dr. Iso and Dr. Webber for their developing and maintaining Monte Carlo event generators. Their sophisticated and effective software have been advantages for studying the jet fragmentation.

I would like to thank my parents for their constant encouragement throughout the years.

The success of this CDF experiment is the results of hard and patient work of many collaborators. I wish to thank all of them. This work was supported by

the U.S. Department of Energy; U.S. National Science Foundation; A. P. Sloan Foundation; Istituto Nazionale di Fisica Nucleare; Ministry of Education, Science and Culture of Japan.

Contents

THE CDF COLLABORATION

F. Abe,[8] D. Amidei,[4] G. Apollinari,[11] M. Atac,[4] P. Auchincloss,[14] A. R. Baden,[6] A. Bamberger,[19] A. Barbaro-Galtieri,[9] V. E. Barnes,[12] F. Bedeschi,[11] S. Behrends,[2] S. Belforte,[11] G. Bellettini,[11] J. Bellinger,[18] J. Bensinger,[2] A. Beretvas,[4] J. P. Berge,[4] S. Bertolucci,[5] S. Bhadra,[7] M. Binkley,[4] R. Blair,[1] C. Blocker,[2] A. W. Booth,[4] G. Brandenburg,[6] D. Brown,[6] E. Buckley,[14] A. Byon,[12] K. L. Byrum,[18] C. Campagnari,[3] M. Campbell,[3] R. Carey,[6] W. Carithers,[9] D. Carlsmith,[18] J. T. Carroll,[4] R. Cashmore,[19] F. Cervelli,[11] K. Chadwick,[4] G. Chiarelli,[5] W. Chinowsky,[9] S. Cihangir,[4] A. G. Clark,[4] D. Connor,[10] M. Contreras,[2] J. Cooper,[4] M. Cordelli,[5] D. Crane,[4] M. Curatolo,[5] C. Day,[4] S. Dell'Agnello,[11] M. Dell'Orso,[11] L. Demortier,[2] P. F. Derwent,[3] T. Devlin,[14] D. DiBitonto,[15] R. B. Drucker,[9] J. E. Elias,[4] R. Ely,[9] S. Errede,[7] B. Esposito,[5] B. Flaugher,[14] G. W. Foster,[4] M. Franklin,[6] J. Freeman,[4] H. Frisch,[3] Y. Fukui,[8] Y. Funayama,[16] A. F. Garfinkel,[12] A. Gauthier,[7] S. Geer,[6] P. Giannetti,[11] N. Giokaris,[13] P. Giromini,[5] L. Gladney,[10] M. Gold,[9] K. Goulianos,[13] H. Grassmann,[11] C. Grosso-Pilcher,[3] C. Haber,[9] S. R. Hahn,[4] R. Handler,[18] K. Hara,[16] R. M. Harris,[9] J. Hauser,[3] T. Hessing,[15] R. Hollebeek,[10] L. Holloway,[7] P. Hu,[14] B. Hubbard,[9] B. T. Huffman,[12] R. Hughes,[10] P. Hurst,[7] J. Huth,[4] M. Incagli,[11] T. Ino,[16] H. Iso,[16] H. Jensen,[4] C. P. Jessop,[6] R. P. Johnson,[4] U. Joshi,[4] R. W. Kadel,[4] T. Kamon,[15] S. Kanda,[16] D. A. Kardelis,[7] I. Karliner,[7] E. Kearns,[6] R. Kephart,[4] P. Kesten,[2] R. M. Keup,[7] H. Keutelian,[7] S. Kim,[16] L. Kirsch,[2] K. Kondo,[16] S. E. Kuhlmann,[1] E. Kuns,[14] A. T. Laasanen,[12] J. I. Lamoureux,[18] W. Li,[1] T. M. Liss,[7] N. Lockyer,[10] C. B. Luchini,[7] P. Maas,[4] M. Mangano[11] J. P. Marriner,[4] R. Markeloff,[18] L. A. Markosky,[18] R. Mattingly,[2] P. McIntyre,[15] A. Menzione,[11] T. Meyer,[15] S. Mikamo,[8] M. Miller,[3] T. Mimashi,[16] S. Miscetti,[5] M. Mishina,[8] S. Miyashita,[16] Y. Morita,[16] S. Moulding,[2] A. Mukherjee,[4] L. F. Nakae,[2] I. Nakano,[16] C. Nelson,[4] C. Newman-Holmes,[4] J. S. T. Ng,[6] M. Ninomiya,[16] L. Nodulman,[1] S. Ogawa,[16] R. Paoletti,[11] A. Para,[4] E. Pare,[6] J. Patrick,[4] T. J. Phillips,[6] R. Plunkett,[4] L. Pondrom,[18] J. Proudfoot,[1] G. Punzi,[11] D. Quarrie,[4] K. Ragan,[10] G. Redlinger,[3] J. Rhoades,[18] M. Roach,[17] F. Rimondi,[19] L. Ristori,[11] T. Rohaly,[10] A. Roodman,[3] A. Sansoni,[5] R. D. Sard,[7] A. Savoy-Navarro,[4] V. Scarpine,[7] P. Schlabach,[7] E. E. Schmidt,[4] M. H. Schub,[12] R. Schwitters,[6] A. Scribano,[11] S. Segler,[4] Y. Seiya,[16] M. Sekiguchi,[16] P. Sestini,[11] M. Shapiro,[6] M. Sheaff,[18] M. Shochet,[3] J. Siegrist,[9] P. Sinervo,[10] J. Skarha,[18] K. Sliwa,[17] D. A. Smith,[11] F. D. Snider,[3] R. St. Denis,[6] A. Stefanini,[11] R. L. Swartz, Jr.,[7] M. Takano,[16] K. Takikawa,[16] S. Tarem,[2] D. Theriot,[4] M. Timko,[15] P. Tipton,[9] S. Tkaczyk,[4] A. Tollestrup,[4] G. Tonelli,[11] J. Tonnison,[12] W. Trischuk,[6] Y. Tsay,[3] F. Ukegawa,[16] D. Underwood,[1] R. Vidal,[4] R. G. Wagner,[1] R. L. Wagner,[4] J. Walsh,[10] T. Watts,[14] R. Webb,[15] C. Wendt,[18] W. C. Wester, III,[9] T. Westhusing,[11] S. N. White,[13] A. B. Wicklund,[1] H. H. Williams,[10] B. L. Winer,[9] A. Yagil,[4] A. Yamashita,[16] K. Yasuoka,[16] G. P. Yeh,[4] J. Yoh,[4] M. Yokoyama,[16] J. C. Yun,[4] F. Zetti[11]

[1] *Argonne National Laboratory, Argonne, Illinois 60439*

[2] *Brandeis University, Waltham, Massachusetts 02254*

[3] *University of Chicago, Chicago, Illinois 60637*

[4] *Fermi National Accelerator Laboratory, Batavia, Illinois 60510*

[5] *Laboratori Nazionali di Frascati, Istituto Nazionale di Fisica Nucleare, Frascati, Italy*

[6] *Harvard University, Cambridge, Massachusetts 02138*

[7] *University of Illinois, Urbana, Illinois 61801*

[8] *National Laboratory for High Energy Physics (KEK), Tsukuba, Ibaraki 305, Japan*

[9] *Lawrence Berkeley Laboratory, Berkeley, California 94720*

[10] *University of Pennsylvania, Philadelphia, Pennsylvania 19104*

[11] *Istituto Nazionale di Fisica Nucleare, University and Scuola Normale Superiore of Pisa, I-56100 Pisa, Italy*

[12] *Purdue University, West Lafayette, Indiana 47907*

[13] *Rockefeller University, New York, New York 10021*

[14] *Rutgers University, Piscataway, New Jersey 08854*

[15] *Texas A&M University, College Station, Texas 77843*

[16] *University of Tsukuba, Tsukuba, Ibaraki 305, Japan*

[17] *Tufts University, Medford, Massachusetts 02155*

[18] *University of Wisconsin, Madison, Wisconsin 53706*

[19] *Visitor*

Chapter 1

Introduction

This introductory chapter gives a historical survey of the major steps leading to the "quark-parton" model, and the general description of the physics of deep inelastic phenomena in the theoretical framework of a non-Abelian gauge theory of strong interaction, i.e. quantum chromodynamics (QCD), and phenominological models for hadron formation. The experimental distinction of two types of partons, which are quarks and gluons in QCD, are also discussed.

1.1 Colored parton

In the 1950's and 60's, it was thought that the hadrons would not be any longer elementary particles, because a great amount of hadron resonances were found. To classify these hadrons, a number of approaches had been tried with some successes. The Sakata model, for instance, provided a good description of meson multiplicities, although it lead to difficulties with the baryons. It was because of the failure of the Sakata model that Gell-Mann and Zweig independently proposed a model which is now called "quark" model [1]. One of the novel properties of the quarks is their fractional charges. Baryons are assumed to be composed of three quarks, each quark is then given a fractional baryon number, B = 1/3. Fractional charges of 2/3 and

$-1/3$ are also given to quarks, according to the conservation of particle charge, strangeness S and the third component of isospin I_3, which relation is well known as Nakano-Nishijima-Gell-Mann formula:

$$Q/e = B/2 + S/2 + I_3. \tag{1.1}$$

The color quantum number has been introduced as an extra degree of freedom in the quark model, in order that the wave function for the Δ^{++} can be antisymmetrized[1] with keeping Pauli principle. Before that, Greenberg proposed the parafermion model[2], which is essentially equivalent to a model in which a quark can take one of three different colors (say red, blue, or green), and antiquarks carry anticolor. Han and Nambu also suggested a model [2] in which each flavor of quark comes in three varieties; it is then not need to give the quarks fractional charge. At present, we take the colored quarks with fractional charges. The subsequent measurement of the cross section for electron-positron e^+e^- annihilation into hadrons, have given strong support to the color hypotheses.

The color charge does not enter the description of hadrons, because color symmetry is not broken. SU(3) was chosen for the color symmetry group for several reasons. First it must be able to distinguish a quark from an antiquark, second hadrons must be color singlet, and finally the number of colors is three. Other candidates for the symmetry, such as SO(3) and U(3), are excluded. Thus the theory of the strong interaction among quarks, theory which is known as QCD, have been formulated based on $SU(3)_{color}$ gauge group. In QCD the gauge bosons are called gluons which are eight color-anticolor states, in other words, they belong to an octet representation of $SU(3)_{color}$. Gluons can couple directly to other gluons, because of their colors, it leads one of the particular property of QCD known as "asymptotic

[1] the wave function of a collection of identical fermions must be antisymmetric under the interchange of all coordinate of any two of them.

[2] Identical parafermions of order of three satisfy the rule that at most three of them can be put in a given state.

freedom", in which an effective interaction strength become small at short distances. This phenomenon had been already suggested by the electron nucleon scattering experiment at SLAC [3], which is widely regarded as the first evidence of Bjorken's scaling [4]. Bjorken derived his hypothesis from behavior of current commutator in the deep inelastic region. Feynman also pointed out that the scale invariance observed in the deep inelastic region can be understood in the term of the hypothesis that hadrons are made up from point-like, quasifree constituents–partons [5].

In perturbative QCD such as leading-log approximation (LLA), the asymptotic freedom can be represented by a running coupling constant, $\alpha_s(Q^2)$:

$$\alpha_s(Q^2) = \frac{12\pi}{(33-2N_f)\ln(Q^2/\Lambda^2)} = \frac{1}{b\ \ln(Q^2/\Lambda^2)} \tag{1.2}$$

where N_f is the number of flavors, and Λ, which is a parameter of the theory, is given by $\Lambda^2 = Q_0^2 exp[-1/b\alpha_s(Q_0^2)]$. Thus eq. (1.2) expresses the strength of the coupling at one Q^2, which characterizes the hardness of the interaction, in terms of that at another scale Q_0^2. At infinite Q^2, partons may be considered as free states, because α_s is zero. This also implies that in the large Q^2 interaction such as jet production, $\alpha_s(Q^2)$ may be small enough so that perturbation approach is reliable.

In the quark parton model based on QCD, partons are identified as quarks and gluons. The QCD has met so far considerable successes and no significant piece of counter evidence has ever been found. It is however true that hadron physics is still complex enough that QCD's predictive power, for instance, the explanation of fragmentation mechanism, is rather limited, as we see in later sections.

1.2 Parton-parton scattering

The hard scattering of partons from two colliding hadrons produces frequently two pairs of back-to-back jets. One is from the hadronization of the hard scattered partons, and the other, which is called "spectator" jet or "beam" jet, originates from

the fragments of the hadron remnants. The spectator jets are therefore directed approximately along the beams–a bunch of colliding hadrons. At the Tevatron $\bar{p}p$ collider, with the center of mass energy $\sqrt{s} = 1800$GeV, such jet production is the most dominant processes, which is called "dijet" event: spectator jets are usually not counted.

1.2.1 QCD jets

The cross sections of the lowest order parton-parton $-qq, qg, gg-$ scattering processes are listed in Table 1.1, in which calculations massless quarks and vector gluons are assumed.

Ignoring for now non-leading corrections (see section 1.3), the dijet cross section expected in $\bar{p}p$ collisions will be

$$\frac{d\sigma(\bar{p}p \to 2jet)}{dy_1 dy_2 dP_t^2} = \sum_{ij} f_i(x_1, Q^2) f_j(x_2, Q^2) \frac{d\sigma(ij \to kl)}{dt}, \tag{1.3}$$

where $f_i(x_1, Q^2)$,$f_j(x_2, Q^2)$ are the structure function giving densities of partons of species i,j with fraction x_1 and x_2 of the total energy-momentum of hadron a when this hadron is probed at a scale Q^2. So far, theory can not predict the absolute form of structure functions, but makes quantitative predictions about their Q^2 evolution of them. The undetermined gluon structure function and Λ parameter give statistical/systematic errors and a small amount of freedom in the application of the leading log formalism to Q^2 evolution. Therefore several slightly different parametrizations have been presented: for example, two sets of EHLQ [6] with $\Lambda = 0.2$ and 0.29, and the two sets by Duke and Owens [7] with $\Lambda = 0.2$ and 0.4, respectively.

In hadron-hadron interaction such as $\bar{p}p$ collision, there is no unique definition[3] of Q^2, although in the case of lepton-nucleon scattering Q^2 is defined by the four

[3]Other Q^2 formulations based on Mandelstam invariants are $\hat{s}$,$\hat{t}$,$\hat{u}$, and $\frac{2\hat{s}\hat{t}\hat{u}}{\hat{s}^2+\hat{t}^2+\hat{u}^2}$.

momentum transfer squared of the lepton. Throughout this paper, for Q^2, we use parton transverse momentum squared p_t^2 in the center of mass frame of two scattered partons.

The definition of jet is obviously arbitrary and found by a suitable algorithm. Several algorithms now used in CDF will be shown in chapter 3.1. Higher-order QCD processes give more elaborate configurations of partons; for example gluons will be radiated from the incoming parton lines and outgoing scattered lines. The dominant configuration however are those where there is only one high-p_t scattering and the additional radiation is approximately collimated with the incident or scattered parton. If the experimental definition of a jet is sufficiently broad (i.e. the cone over which hadron energy is summed into a single jet is wide enough), the dominant high-p_t configuration again leads to dijet production. CDF have indeed taken rather broad angular definitions for a jet.

1.2.2 Direct photons

In addition to fragments of scattered parton, the photons with large transverse momenta are directly produced in hard parton-parton interactions. The production of such high-pt "direct" photons may proceed via Compton processes: a) $\gamma q \to \gamma' q'$ and b) $qg \to \gamma q'$, and quark antiquark annihilation. In case of a), the production cross section is proportional to the square of the electromagnetic coupling constant α, while that for b),c) and d) is proportional to $\alpha\alpha_s$. The lowest-order Feynman diagrams for the direct photon production are shown in fig. 1.1. At the Tevatron energy, one can not ignore a higher-order contribution from the gluon-gluon box diagram as shown in fig. 1.2 because of the large gluon structure function at small values[4] of x. The final state of this process is $g + \gamma$, but one notices that the direct photon with relatively low E_t is still likely associated quark jet (see fig.).

[4]Momentum fraction: x_1 and x_2 in eq. (1.3).

1.3 Parton showers

The cross section for the $2 \to 2$ parton subprocesses are obtained by applying lowest order perturbation theory; thus higher order correction are unaccounted for. In e^+e^- annihilation such as PETRA [8] and PEP, three or four jets events, which are expected from higher order QCD contributions, were analysed by so-called "matrix element approach": the three-parton and four-parton contributions are calculated exactly to $O(\alpha_s^2)$. In hadron collisions, however, the exact calculation of the higher order is difficult, and the model contains several theoretically unattractive features such as its limited jet multiplicities, from which the reliable extension of the model to higher energies suffers. At present, Most Monte Calro's therefore forego a matrix element approach and adopt a "parton shower approach", in which the emission of an arbitrary number of partons is automatically included.

The parton shower approach permits the description of multi gluon radiation in terms of a cascade-like process:

$$q \to q + g, \quad g \to g + g, \quad g \to q + \bar{q}. \tag{1.4}$$

These branching process continue until predetermined cut-off scale is reached. At this point the perturbative evolution is terminated and some model will be applied to convert partons into hadrons (see section 1.4). The basic equation describing the probability that a branching $i \to j\,k$ will occur during a small change dt is Altarelli-Parisi evolution equation:

$$\frac{dP_{i\to jk}}{dt} = \int dz \frac{\alpha_s(Q^2)}{2\pi} P_{ji}(z). \tag{1.5}$$

Here z gives a sharing of energy between daughters j and k. Also the t and m_i are the evolution parameter, which is usually taken to be $\ln(m_i^2/\Lambda^2)$, and the parent parton mass, respectively. The function P_{ji}, which is well known Altarelli-Parisi splitting kernel, depends on the process considered. For instance in the quark

used in e^+e^- annihilation and $\bar{p}p$ collider experiments. The hadrons produced in a majority of e^+e^- annihilation events show a clear dijet structure with a jet angular distributions as predicted for the process $e^+e^- \to q\bar{q}$. In addition, some events show a three jet structure which resulting from hard gluon radiation: $e^+e^- \to q\bar{q}g$. The methods in e^+e^- annihilation are based on these two samples, although details of analysis are different. In some experiments such as JADE, TPC and AMY [28,31], they assigned the lowest energy jet in the three-jet event as a gluon jet and the other two-leadings as quark jets. On the other hand, for instance, MARK-II and HRS selected three-fold-symmetric three-jet events [29,30], in which all jets had nearly the same energy[5], and then compared the events with dijet events, or with Monte Carlo's. In hadron colliders, UA1 exploited the difference of the structure functions between a quark and a gluon, and performed a statistical separation [32] of quark and gluon jets, and consequently obtained a quark-enriched and a gluon-enriched sample from the dijet events. This UA1 method is unfortunately not useable for CDF, because the average momentum fraction x of CDF is much smaller than that of UA1, and the resulting probability distribution for individual jets to be gluons does not have the two-humped structure, i.e. quark and gluon peaks.

1.5.2 Differences between quark and gluon jets

It is interesting to consider what physical observables would differ if the initial partons were quarks rather than gluons. One observable that is often used is the particle multiplicity in the jet, because the multiplicities of gluon jets is expected to be higher than those of quark jets [33,34]. In the asymptotic limits, i.e. $Q^2 \to \infty$, the ratio of multiplicities of a fixed species in a quark and in a gluon jet is simply given by

$$\frac{\langle n \rangle_q}{\langle n \rangle_g} = \frac{C_F}{C_A} = \frac{1}{2}\left(1 - \frac{1}{N_c^2}\right) = \frac{4}{9}. \tag{1.10}$$

[5]The probability of identifying the gluon jet was lower accordingly; naively speaking about 1/3.

Similarly, the ratio of the angular radius of the quark jet to that of the gluon jet is also given by

$$\frac{\ln(\delta_q)}{\ln(\delta_g)} = \frac{C_F}{C_A} = \frac{9}{4}. \tag{1.11}$$

This means that gluon jets are much broader than quark jets. These predictions are however too asymptotic compared to the *real* world to agree with the experimental results well [28,29,30,32]. The higher order calculations [35] result in smaller differences between quark and gluon jets.

The differences mentioned above are related to higher color charge of the gluon. Another possible source of difference is a gluon spin. Let us first consider the analogical QED process: the annihilation of a photon into e^+e^- . If the photon is linearly polarized, the plane defined by the electron and positron momenta have strong correlation with the polarization plane of the photon. A historical example of utilization of this effect was the experimental determination of the parity of the π^0 meson. The gluon has the same spin 1 as photon. It is therefore conceivable that the plane defined by the momenta of two particles in the first stage of decay, i.e. q and $\bar{q}$, or 2 g's, has a similar correlation with the polarization plane of the original gluon. A detailed discussion and results are given in Appendix B and C.

The study of the quark/gluon fragmentation not only provides a basic information on the hadronization mechanism, but it opens a wide window for heavy particle spectroscopy. New heavy particles which we wish to find in the high energy collisions, e.g., W′, Z′, heavy flavors and leptons, higgs, technicolor, and supersymmetric particles, have decay modes to quarks, and their branching ratios are larger than those of the (semi-)leptonic modes by the color factors. Thus, the hadronic decay channel, if identified, will be quite useful in search for these new particles. In case of hadron collider experiments, however, there exists a large amount of QCD multijet background from such processes as gluon-gluon and gluon-quark scatterings. One therefore has to develop a method to get rid of background gluon jets, i.e. separate

the quark jets from the gluon jets, to put the hadronic channel to a practical use in new particle searches. This thesis presents the study of fragmentation properties and the experimental distinction of gluon and quark jets with a method based on Monte Calro's.

Chapter 2

Apparatus

2.1 CDF overview

The Fermilab Tevatron Collider is presently the world's highest energy accelerator, which provides antiproton-proton collisions at the center-of-mass energy, $\sqrt{s}$ =1.8TeV. The Collider Detector at Fermilab (CDF) is a multi-purpose detector locating at the B0 intersection region of the Tevatron. The detector consists of several components; calorimeters, tracking chambers, solenoidal magnet [36] and muon. It covers 360° in azimuthal angle ϕ and from 2° to 178° in polar angle θ . The calorimeter is divided into Central region $30° \leq \theta \leq 90°$, Plug region $10° \leq \theta \leq 30°$, and Forward region $2° \leq \theta \leq 10°$. The forward/backward calorimeter was 711 cm from the center of the CDF detector along the beam axis. A perspective view is given in fig. 2.1. There are drift chambers outside the calorimetry for muon detection in the central rapidity region, $|\eta| \leq 0.7$. The forward/backward muon chambers measure muon position and momentum for polar angles between 3° and 16° and between 164° and 177° with magnetized iron toroids. CDF has four tracking devices which provide information at the single particle level (see fig. 2.2). These are the Vertex Time Projection Chamber (VTPC) [37], the Central Tracking Chamber (CTC) [38], the Central Drift Tube (CDT) [39], and the forward Tracking

Chamber (FTC) [40] The VTPC surrounding the beam pipe was mounted along the beam direction (z-axis). The total length of 2.8 meters of the chambers assures adequate coverage of the event vertices ($\sigma_z \sim 30$ cm). The CTC occupies most of the superconducting, solenoidal 1.5 T magnet. The CTC is responsible for the accurate measurement of particle momenta in the central region $30° \leq \theta \leq 150°$. The CDT array located on the outer cylindrical surface of the CTC provides high-accuracy $r-\phi-z$ information at the radius of 1.4 meter for tracking charged particles produced in the central region. The FTC is located outside of the Plug calorimeter to cover the forward-backward tracking region of $2° \leq \theta \leq 10°$ and $170° \leq \theta \leq 178°$ cone angle. The region of Pseudo-rapidity[1], η, subtended by the tracking chambers and calorimetry are summarized in Table 2.1. Fig 2.3 shows the schematic view of the solenoid system together with the other central detector components of the CDF. The solenoid consists of a superconducting coil, an outer support cylinder, a cryostat, a chimney, and a control dewar. The control dewar is placed outside the iron return yoke and connected to the cryostat with a chimney in order to minimize the interference with the detector. The main parameters of the solenoid are summarized in Table 2.2.

2.2 Calorimetry

The central electromagnetic calorimeter (CEM) [41] are composed of 48 modules, each consisting of 31 lead-scintilator layers, *stack*, with the strip chamber embedded between the 8-th and 9-th layers, at the depth corresponding to maximum average transverse shower development. Each module is divided into projective towers, each covering 0.1 in η and 15° in ϕ . Wavelength shifters fit into a gap between machine finished surface of the *stack* and 3/16 in. thick steel cover plates, one on each side

[1] $\eta = \ln \tan(\theta/2)$

for two per tower. The gap represents 4.8% of the azimuth. The total thickness of *stack*, held under 20 psi for machining, is kept to 12.6" ± 0.1" by selective insertion of layers of 0.01" mylar. The strip chamber defines the electromagnetic shower center in the lateral shower profile. This chamber system determines the particle hit position on the chamber plane to an accuracy of 2 mm. However, the chamber system does not cover the whole area of wedge module. The effective region which the strip chamber covers in a module is $|x| \leq 22.5$ cm in ϕ and $6.0 \leq z \leq 239.4$ cm in θ , whereas the whole range of the active area extends to $|x| \leq 23.1$ cm and $4.2 \leq z \leq 246.0$ cm on the strip chamber plane. The axes x_s, y_s, and z_s are defined as shown in fig. 2.4.

The calibration of the CEM was determined with 50 GeV electrons and charged pions in Neutrino-West beam line at Fermilab, and with cosmic ray muons; for details, see references [42,43]. For the absolute energy calibration, all 48 wedge modules of the CEM were exposed to 50 GeV electrons with a beam size of roughly 2.5 cm in diameter at the center of each tower. In order to investigate the precise response map of entire tower, Five out of 48 wedges were actually scanned by 50 GeV electrons over the tower face with about 4 cm spanned in both of the horizontal and vertical directions. A wedge module is divided into 50 × 250 cells of 1 cm × 1 cm area in this scanning. The nonuniformity of the response map is defined as the fractional difference of the response in each cell from the overall average. The overall nonuniformity is 3.9%, while the uniformity at θ-boundaies and ϕ-cracks increases typically to 5% and 7% respectively. The module-to-module and tower-to-tower similarity varies from 0.7 to 0.9% depending on the tower number. At the ϕ-cracks and tower boundaries, the similarity is larger, being 1.8% and 2.0% respectively. The response function is derived using 12 parameters for each tower. The overall reproducibility of the response function is estimated to be 1.7% for the entire region of all towers and 1.3% for the main central region, $|x| \leq 20$ cm and $z \leq 234$ cm;

84% of the entire region. The response correction function, which is the inverse of the response function, is implemented from a data base and is to scale the energy at any point with respect to the absolute calibration constant at the reference points. Energy resolution for electrons centered in towers is well described by $\sigma(E)/E = 13.5\%/\sqrt{Esin\theta}$ (with E in GeV). The energy dependence for electrons from 10 to 100 GeV appears to be too large by about 4% at 100 GeV. The position resolution of 2 mm at 50 GeV has been achieved. Long term gain variations are monitored by a set of $^{137}C_s$ sources, one per wedge, which can be moved through the module under remote control. Short term gain changes are also monitored by light flasher systems. The characteristics of CEM are summarized in Table 2.3. Details of the strip chamber are also listed in Table 2.4.

The central (CHA) and endwall hadron calorimeters (WHA) [44] have cylindrical symmetry and cover polar angle between 30° and 150°. The CHA consists of 48 steel-scintillator with 2.5 cm sampling, and WHA consists of 48 steel-scintillator with 5.0 cm sampling. Each calorimeter module is divided into projective towers, each covering roughly 0.1 in pseudorapidity η and 15° in azimuthal angle ϕ , matching those of the CEM which is front of it. This segmentation is fine enough that quark and gluon jets will normally spread over more than one tower. For each 15° aximuthal slice there are 24 towers in all, of which 12 are totally in the CHA, 6 totally in the WHA, and 6 are shared. The CHA modules, covering polar angle between 45° and 135°. are 32 layers deep. They are stacked into four free standing C̈-shaped arches which can be rolled into and out of the detector. The WHA modules cover polar angles from 30° to 45° and from 135° to 150°. They are pluged into cavities in the solenoid magnet yoke and serve as part of the flux return path. Fig. 2.4 shows one quadrant of the large angle CEM and CHA segmented into 12 polar towers. Table 2.5 and 2.6 summarize various parameters of the large angle hadron calorimetry.

The end plug electromagnetic calorimeter (PEM) [45] are located at the both ends of the superconducting solenoid magnet. Each of the east/west calorimeter consists of 34 sampling layers, each of which is composed of a 2.7 mm thick lead sheet and a chamber of gas proportional tubes with cathode pad readout. The proportional layers in the calorimeter are divided into quadrants. Fig. 2.5 shows a isometric view of a quadrant showing the projective pad tower structure and longitudinal layers. The pads are ganged longitudinally into towers with two depth segmentations. Besides the pads, the first ten layers of the second segment have a strips of two types as shown in fig. 2.6. The longitudinal layer configuration is summarized in Table 2.7. The anode information is intended primarily for diagnostic purposes, but also provides a longitudinal profile of the energy deposition for each sector. The entire stack of each gas modules is contained in a round disk-shaped gas tight vessel, in which a mixture of argon-ethene 50/50 is used, for each of the east and the west PEM calorimeters. The sampling fraction of PEM for a minimum ionizing particle is, very roughly 1/1000. It means, for example, that a 1 MeV deposit in a gas is interpreted as 1 GeV.

Calibration and performance studies were carried out during 1985 in the M-Bottom beam line at Fermilab. The M-Bottom beam line provided secondary electrons and pions in energy range 20–200 GeV with a momentum bite of roughly 4% from ruins of an 800 GeV proton beam incident on a fixed target. The beam momentum was analyzed with a set of multiwire proportional chambers, which also tagged beam position, and a dipole magnet upstream of the test apparatus. The detailed setup of M-Bottom is described in [46].

The pad energy resolution, as seen in fig. 2.7, is approximately 3% at 100 GeV with 1.8 kV operation voltage. Fig. 2.8 shows the dependence of the energy resolution on the operation voltage. 1.7 kV operation voltage is determined by this plot. The position resolution is also measured. Figs. 2.9a and b show the pad resolution in

the θ-direction and ϕ resolution respectively. With θ strips, the resolution becomes 0.04° to 0.06° in θ and about 0.1° in ϕ . Table 2.8 summarizes the performance of the PEM.

The plug hadron calorimeter (PHA) consists of 20 sampling layers, each separated by 5 cm steel plate. The total average number of interaction lengths is 6.5. The proportional chambers with the same design as the PEM are operated with a gas mixture argon-ethene 50/50. The transverse segmentation follows that of the PEM calorimeter. For each tower, the longitudinal sampling layers are ganged into a single depth segment. In addition, the chambers are divided into 30° sectors in the azimuth, so called *stack*. As in the case of the PEM, all anode wires in a single chamber are ganged and read out giving longitudinal information from each plane in the 30° sector.

A subset of the *stacks* were tested at the M-Bottom beam line, whereas the entire west PEM chamber was placed in the calibration beam, because of the difficulty of moving PHA chamber *stacks*. The forward calorimeter, contains gas-tube calorimeters of similar design, although the tubes are constructed using aluminum and fiberglass instead of resistive plastic

The forward electromagnetic calorimeter (FEM) [47] consists of two modules located approximately 6.5 m from the nominal interaction point ($z = 0$), one to the forward and one to the backward. Fig. 2.10 shows a perspective view of one half of a calorimeter. Each forward/backward calorimeter which is roughly 3 m on a side and 1 m deep has 30 sampling layers of proportional tube arrays interleaved with lead absorber panels. The longitudinal layers were ganged into two depth segments, both of which are 15 layers thick. One side of each chamber in the calorimeter consists of an aluminum channel plate which forms three walls of the 124 proportional tubes. A cross sectional view of a chamber is shown in fig. 2.11. Each pad subtends 0.1 units of pseudorapidity η and 5° of azimuthal angle ϕ . The anode wires are strung

vertically and are ganged together in 5 sectors per chamber.

The measured energy response of the forward/backward calorimeter at the M-bottom beam line is linear up to 160 GeV and measured energy resolution is (25.4 ± 0.7)%$\sqrt{E}$+(0.47 ± 0.01)%. The position resolution varies between 1 mm and 4 mm depending on location in the calorimeter. The calorimeter offers good e/π discrimination, where typically the pion misidentification probability is less than 0.5% with the electron identification efficiency greater than 90%.

Each of the forward/backward hadron calorimeters [48] were segmented into four independent sections which are each composed of 27 steel plates and 27 ionizing chambers. The cathode surface of each of the ionization chambers has been segmented into 20 bins in pseudo-rapidity ($\Delta\eta = 0.1$) and 18 bins in azimuth ($\Delta\phi = 5°$). It consists of 20 layers of chambers separated by 5 cm thick iron plates, and is completely shadowed by the FEM.

High voltage is distributed to the anode wires using a system developed for CDF gas calorimeters. CAMAC controlled bulk supplies are located in the CDF counting room and feed distribution cards which are located in RABBIT crates in the collision hall. The HV distribution cards have 20 channels which provide high voltage to individual chambers. Each channel has its current monitored and is controlled by a high voltage relay. The status of the high voltage system is continuously monitored by the CDF alarms and limits system.

2.3 Tracking chambers

The VTPC, which is eight separate time projection chambers, mounted end to end along the beam axis, covers a very large wide range in polar angles ($3.5° \leq \theta \leq 176.5°$) to determine overall event topology and provide z-vertex information. The z-resolution depend on the polar angle θ averaged over the drift length. For 90° tracks the z-resolution 420 μm , rising to 1 100 μm at 11°. Two VTPC modules are

shown in fig. 2.12. Adjacent modules have a relative rotation angle of $\phi_0 = tan^{-1}0.2$ about beam axis to eliminate inefficiencies near octant boundaries and provide ϕ information from small angle stereo. Each module has a center high voltage grid that divides it into two drift regions. At the end of each drift region are proportional chamber octants. An octant consists of a cathode grid followed by a plane of field shaping wires. A summary of VTPC parameters is given in Table 2.9. Since all particles from $\bar{p}p$ interactions that are detected by the calorimeters and the other tracking chambers first pass through VTPC, the entire VTPC system must be very thin in terms of radiation lengths.

The CTC is a wire chamber with 84 layers of sense wires arranged into 9 super layers. Fig. 2.13 shows the end view of the chamber which is a cylinder of diameter 2 760.0 mm and length 3 201.3 mm. The five axial layers where 12 wires are parallel to the beam axis are interleaved with four stereo superlayers in which the angle between the sense wire and the beam axis alternates between ± 3°. The CTC's mechanical specifications are given in Table 2.10. The resolution of a stereo wire in the z-coordinate, is expected to be approximately $0.2\text{mm}/sin3° = 4$ mm, equal to the position resolution of the CTC. The double track resolution is expected to be ≤ 5 mm or 100 ns. A further requirement is that the position information from the tracking should match the position resolution of the calorimetry. Stereo wires with a resolution of 3 to 4 mm meet this requirement. The performance specification for the CTC is summarized in Table 2.11.

The CDT arrays just inside the coil will provide a $r-\phi-z$ space point for particles in the range of polar angles between 45° and 135° with respect to the beam direction. The CDT operates in the limited streamer mode to obtain the maximum possible z-resolution, $\sigma \leq 0.1\%\text{L} \sim 3$ mm. For the identification of muon candidate in the central region ($|\eta| \leq 1.$) as the trigger, the CDT is also required $r-\phi-z$ information: $\sigma \sim 1.0\%\text{L}$, $\sigma \sim 1°$. The CDT array consists of three layers

of drift tubes which are 3 m long, 12.7 mm outer diameter as shown in fig. 2.14. Tracking of charged particles in the $r-z$ view of the CDT array accomplished via charge division along the anode wires; drift-time measurements in the $r-\phi$ view. 50 μm diameter anode wire is supported near the center (in z) of the tube by a Delrin collar in order to reduce the electrostatic deflection.

The FTC covers the forward/backward regions (about 2 units of rapidity). Fig. 2.15 shows 72 wedge shaped cells of an FTC. The chamber contains planes of anode and field shaping wires that alternate with planes of cathode strip. Each plane of anode and cathode is 5° cell, where 50 μm diameter sense wire and 150 μm diameter field shaping wires are strung approximately along the radial direction (normal to the beam axis) as shown in fig. 2.16. There are 84 strips which are 25 μm thick and 6 mm wide on each side of a cathode plane. Some of the mechanical specifications of the FTC are summarized in Table 2.12. At the 1987 run, the FTC was operating with high tracking accuracy of 140 μm per wire and multitrack resolution of 2–3 mm The double track can be identified if they are separated by at least 1 mm. 15 charged particles on the average were observed in both forward/backward direction.

2.4 Muon chambers

There are two muon detectors [49,50] at the CDF for muon detection. The central muon detector (CMU) which covers $50° \leq \theta \leq 140°$ is located around the outside of the CHA at the radial distance of 3470 mm from the beam axis. The CMU is segmented in ϕ into 12.6 wedges which fit into the top of each central calorimeter wedge as shown in fig. 2.17. Each CMU wedge is further segmented in ϕ into three modules. Each of them consists of four layers of four rectangular drift cells. A stainless steel resistive 50 μm sense wire is located at the center of the cell.

At the cosmic ray test, the CMU chambers give adequate resolution in the drift

direction of $\sigma = 250$ μm (ϕ direction) and an rms resolution along the sense wire of 1.2 mm (z direction) [49]. Charge division is used to obtain the position of a track along the sense wire to reduce the number of electronics channels to enable readout of the chambers to occur at one end of the chamber only.

The forward muon detector (FMU) consists of a pair of magnetized iron toroids instrumented with three sets of drift chamber and two plane of scintillation counters. The FMU toroid magnets which are 7.6 m o.d. × 1.0 m i.d. × 1.0 m wide provide an azimuthal field of 1.8 T at a radius of 2.0 m in the steel. The field varies from 2.0 T at the inner radius to 1.6 T at the outer radius. Particle displacement due to the fields gives the momentum resolution of 13%.

Fig. 2.18 shows elements of the FMU detector plane. The plane form a 24-sided figure with each wedge-shaped detector subtending an angle 15° in azimuth. The drift chambers come in three different sizes depending on their distance from the beam crossing. The drift velocity in a 50/50 argon-ethene mixture is 5.0 cm/μs and a position resolution of 130 μm has been achieved in a test beam. Each wedge of scintillation counters is 3.3 m long and × 1.0 m × 14 cm at the large and small ends respectively as shown in fig. 2.18. The detection efficiency of the counters has been measured to be grater than 99.5% over their entire surface.

2.5 Beam-beam counter

The Beam-Beam Counter (BBC) [51] consist of two planes each with 16 time-of-flight scintillation counters, one to the east and one to the west of the interaction region. The east and west modules were placed at the forward and backward positions of 581.6 cm (19.4 nsec) from the nominal collision point ($Z = 0.$), respectively. These 16 counters were divided into four types depending on the size of the counter and on the phototube attached, as shown in fig. 2.19. Each type counter covers approximately equal range in pseudorapidity $\Delta\eta = 0.7$. The BBC system as a

whole covers the region $3.2 < |\eta| < 5.9$.

The BBC are useful in finding the interaction point, which is necessary because the bunch size at the Tevatron is expected to have $\sigma \sim 30$ cm. With a timing resolution of 200 psec, the BBC can be used to localize the interaction point to with in 10 cm at the trigger level, and also provide the tracking chambers with an accurate measure of the interaction time.

2.6 Data Acquisition

2.6.1 Overview

The Data Acquisition System (DAQ) for CDF consists of the following components: Redundant Analog Bus-Based Information Transfer (RABBIT), FASTBUS and VAX computer clusters. The RABBIT system [52] was developed to handle about 60 000 analog readouts with large dynamic range from calorimeters. The FASTBUS network [53], which contains the digital readout system for tracking chambers, coordinates the timing and transfer of data from the RABBIT and trigger system into the VAX. CDF uses MX scanners [53] to access RABBIT systems and SSP scanners [53] for tracking systems. The data are then stored on the magnetic tapes. The information on "run-condition" such as highvoltage and magnet current is stored in databases. The results of calibration performed periodically are also stored in databases and the parameters calculated are downloaded to the scanners to correct the data online.

2.6.2 Trigger

CDF has the multi-level trigger structure (Level 1,2 and 3) to select events reducing the taking rate to the one event per second so that Tape-Drivers can handle it. The Level 1 [54] first require the BBC coincidence to reject the beam-gas events.

The additional condition such as large energy deposition in calorimeters and missing energy are required. We describe the calorimeter trigger of Level 1, because they are responsible for the data used for this analysis. The Level 2 jet clustering was also described at the end of this section, although Level 2 was not functional during the 1987 collider run.

The central calorimeter consists of projective towers of 15° width in ϕ and a width of 0.1 in η . This projection geometry is preserved in the trigger, but to reduce the number of signals, four photomultiplier signals are summed together to produce logical trigger towers with a width of 0.2 in η and 15° in ϕ . This summation is done on a FASTBUS card called the Tubesum [54]. The gain of the front end electronics has been adjusted so that, for central calorimeters, a 100 GeV energy deposition in the center of a tower gives -1 V out of the Tubesum.

The gas calorimeters, which have finer azimuthal segmentation, are also summed into logical trigger towers of $\Delta\phi = 15°$ and $\Delta\eta = 0.2$. In this case, however, the summation is done at the detector on the front end amplifier cards. After summation into trigger towers, the signal are sent to the trigger counting room via cables. Gas gains are adjusted such that a 50 GeV transverse energy E_t deposition produces -1 V at the trigger. The discrepancy between central and gas calorimeter gains is compensated for by the Receive and Weight (RAW) cards [54] in the trigger system.

Eventually, entire detector is represented by 42 in $\phi \times 24$ in θ trigger towers. All trigger towers, both electromagnetic and hadron, above a single tower threshold are summed and compared to the total E_t threshold, which was set to one of four values: 20, 30, 40, or 45 GeV for the 1987 run. At the Level 2, the trigger towers are clustered by hardware using as follows. It starts by finding the seed trigger towers above a seed threshold and then gathering energy of adjacent towers above a single trigger tower threshold. Here electromagnetic and hadron towers are treated separately, and merging is not made at all. Typical thresholds of cluster E_t are 20,

40 or 60 GeV, and multijet triggers are also included.

Chapter 3

Event sample

3.1 Jet reconstruction

The parton fragmentation process with the subsequent deposition of single particle energies into the towers of the calorimeter creates the typical jet structures observed in collisions producing high transverse energy. We therefore use the energy information on calorimeter towers to reconstruct a jet, but the assignment of towers to the jet is not unique. Currently four different algorithms [55] are available in the CDF; CLUST2, CLUST3, JETCLU, and CLUST4.

Roughly speaking, the CLUST2 and the CLUST4 are neighbor searching "cluster algorithm", while the JETCLU and the CLUST3 are "cone algorithm". The cluster algorithm combines contiguous regions of energy around the highest E_t tower, with the requirement that the energy be monotonically decreasing. The energy collection of the cluster algorithm is usually limited to the core of the jet, i.e., low energy (under the tower threshold energy) towers may not be connected to the jet cluster. The founded clusters are therefore merged if they lie within a merging radius in $\eta-\phi$ space. This merging process, which improves energy collection, are contained in both CLUST2 and CLUST4, but with slightly different schemes. A priori cone algorithm, which is often called "window algorithm", assigned all

energy deposits in a rectangular window to the jet. It has been used in a trigger processor at some experiments (f.i. UA2) because of its easy implementation and very fast execution time. The rectangular shape of the windows does not reflect the expected approximate rotational symmetry of the energy flow around the jet axis. The current cone algorithm uses a cone instead of a window to collects the energy. The cones have a circular cross-section in the $\eta-\phi$ plane to account for the distortion expected form the Lorentz transformation. The JETCLU employs a fixed cone, while the CLUST3 uses variable cone sizes, i.e. the radius R varies with calculated cluster E_t. This is due to the expected picture of jets that the jet are more collimated as the jet E_t grows. In general, the cone algorithm exhibits shaper space distinction than the cluster algorithm based on interconnected tower structures. As mentioned before, merging clusters however improves the sharpness of the cluster algorithm, and consequently, it has been difficult to determine which algorithm is better. Moreover, it is impossible to do full justice to all algorithm because of a lot of parameters, such as merging radius, cone-shrink ratio, etc, which can be tuned. In fact, there are no striking difference between four jet algorithms as shown in Table 3.1. For this analysis we have choosen JETCLU, because the procedure is applied to group the particles together in order to form the experimental definition of a jet tracks. This procedure employs the fixed cone around the centroid of a jet determined by the jet algorithm. The JETCLU is thus most closely related to the track association procedure. The next subsection describes more details of JETCLU.

3.1.1 JETCLU

The JETCLU starts by making a list of all the towers with an Et greater than some threshold, called Et_{seed}. A second list containing candidates for clustering is made of all towers above a second threshold Et_{cand}. At the present the default values

of Et_{seed} and Et_{cand} are 1 GeV and 0.1 GeV, respectively. Precluster are formed from combining all touching seed towers, which are required to have continuously decreasing tower E_t. If the total E_t of a precluster is larger than 2 GeV, it is used as a starting point for clustering. The clustering is performed using true tower segmentation without ganging [1] towers used in preclustering. A fixed cone in $\eta - \phi$ space of radius R is formed around the centroid determined from the E_t weighted centroid of the precluster. The candidate towers in this cone are merged into the cluster and the centroid is recomputed. Again, all candidates inside the cone around the new centroid are merged in. This process is iterated on until the tower list remains unchanged. The actual cone size used in the analysis is 0.7.

Two cluster overlap could be occur, because the cluster was formed without regard to the possible presence of others. This overlap problem is handled as follows. If one cluster is completely contained in another, the smaller one is dropped. If the towers have some finite overlap, then an overlap fraction is computed as the sum of the E_t of the common towers divided by the E_t of the smaller cluster. If the fraction is above a cutoff (default is 0.5) then the two clusters are combined. If the fraction is less that the cut, the clusters are kept intact, and the energy is divided up between the clusters, based on the proximity of the towers to the centroid. After the energy has been divided up, the centroids are recomputed. This tower re-shuffling process is iterative, and ends when the tower lists remain fixed.

3.2 Jet to parton correction

This section describes the jet energy correction. We start with the definition of the 4-vector of the jet cluster found by the jet algorithm. Each tower of calorimeters in the cluster is treated as a massless particle (tower-particle) with all energy

[1] In the preclustering, the gas calorimeter towers are ganged together in groups of three in ϕ to correspond to the central segmentation.

assumed to be deposited in the tower center. The polar angles of the electromagnetic and hadronic towers which have the common tower index are given separately, because the event vertex is different from the exact center of the calorimeter, while the azimuthal angles are common. The cluster momentum and energy are then calculated as the vector sum and the scalar sum of both electromagnetic and hadronic tower energies, respectively, and the jet has a finite mass as a result.

The measured 4-vector of the jet is generally not equal to that of the parton from which the jet comes. This is the result from both instrumental and physical effects such as low energy non-linearities, η crack energy losses, underlying events and clustering. One can estimate these effects comparing the real data with the Monte Calro and detector simulations[2] with the same jet algorithm. Measuring the η dependence of jet transverse momentum P_t response from the calorimeters provides a "response map" [56], which allows us to correct the jet 4-vector. We are however aware of the difficulties to correct the jet back to the primary parton exactly, because the partons produced far off mass-shell generate showers as mentioned in Chapter 1.3, and consequently the final state includes multi partons. We thus generated events with Isajet Monte Carlo event generator, in which the gluon radiation was turned off. The generated events shows rather clean dijet structures, allowing us to associate each particles with its parent parton in an unambiguous way. In addition, we correct the jet back to the final particles the parton fragmented into instead of the parton itself, thereby minimizing the inherent uncertainty of the Monte Carlo (e.g. energy non-conservation in Isajet).

[2] see section 3.5

3.3 Event selection

The goal of the analysis is the experimental distinction of gluon and quark jets. It is therefore needed to prepare a gluon-rich and a quark-rich sample. We choose the dijet events as the gluon-rich sample, because the dominate dijet final state is gluon-gluon at the CDF energy, while for the quark-rich sample, we take the "γ+jet" events, in which the direct photon associated with jet is produced. Fig. 3.1 shows theoretical prediction of the fraction of the final state gluon in the samples, dijets and γ+jet events. Here the calculation of the dijet cross section is of the lowest order QCD only, but it includes the higher order QCD contributions to the cross section of γ+jet (i.e. gluon-gluon fusion, see fig. 1.2); the used structure functions are EHLQ [6] and Duke-Owens [7] with $\Lambda = 200$ MeV. The production of the quark jet associated with the direct photon, for instance at $E_t = 20$ GeV, is dominant by about one order of magnitude compared to the $gluon + \gamma$ production. When going to higher E_t (i.e. 60 GeV), the gluon fraction in the γ+jet events increases up to about 30%, whereas that in dijet events decreases down to about 70%.

3.3.1 Dijet events

The data were taken from the 1987 runs which were triggered by the calorimeter trigger described in Chapter 2.6.2. The integrated luminosity contained in these runs is approximately 26 nb^{-1}. The data were fully reconstructed with the version 4.4 tracking and clustered using the JETCLU with a cone size R of 1.0. We require the energy centroid (jet axis) of the leading and next to leading jets to be in the central region $|\eta| < 0.8$, and call them "central-central" jets. In order to remove trigger inefficiency bias [57], the sum E_t cuts were then placed on central-central jets at 36, 48, 56, and 60 GeV, depending on the hardware sum E_t thresholds, before jet energy corrections mentioned in the last section was made.

At this stage, the events passed the above preliminary cuts are reclustered by JETCLU with $R = 0.7$ and their energies are corrected by the response map described in section 3.2. To insure that the jet is well contained in the central calorimeter avoiding non-uniform regions such as the 90° crack and boundaries between the central and plug calorimeters, we require at least one of the two leading jets with $0.1 < |\eta| < 0.7$. The two leading jets are further required to be within 25° from back-to-back configuration in ϕ according to the expected dijet structure.

For the track association, we first boost the events to the longitudinal dijet center of mass system using the corrected 4-vectors of the jets. In this Lorentz transformation, the masses of all charged particles are assumed to be equal to the pion mass. In the dijet rest frame, a cone is formed around the jet axis. This cone is defined by a minimum pseudorapidity with respect to the jet axis, $\eta_\perp$, as opposed to the R used for the clustering of calorimeter towers. The tracks within the cone are selected as jet particles, but tracks with poor quality are removed by requiring three-dimensional reconstruction capability and other quality cuts such as impact parameter or delta-z cut [58]. For 1987 data, we also exclude these jets whose axis are in the region, $-24° \leq \phi \leq 35°$ and $188° \leq \phi \leq 247°$ (*Dead Region* $\pm$ 20°) because of the dead cells in the CTC.

3.3.2 γ+jet events

Events were selected from 1989 data which were triggered by "Photon-10" and "Photon-23"[3], and are required to have an isolated electromagnetic (EM) cluster and one jet in the opposite hemisphere ($\pm$ 25° in ϕ) in the central region. All data have been completely preprocessed, which means that the calorimetric and tracking information has been fully reconstructed (including energy scale correction, version 5.1 tracking, clean up, etc.).

[3]They require at least one EM cluster with $E_t > 10$GeV and $E_t > 23$GeV, respectively.

We start with the photon identification. Since a true single photon energy deposition is well localized in a single tower of central calorimeter, we require the lateral shower sharing variable LSHR<0.2 [59]. LSHR is a CEM 3-tower isolation characteristic obtained from a trajectory[4] and fitted lateral profile for EM showers to the observed tower sharing in the CEM calorimeter. In addition, the events are filtered by isolation requirement:

$$I_{0.7} = \frac{E_{tcone} - E_{t\gamma}}{E_{t\gamma}} \leq 0.15\,, \tag{3.1}$$

where the $E_{t\gamma}$ and E_{tcone} are the total transverse energy of EM cluster[5], and that within a cone[6] in $\eta - \phi$ space of radius $R = 0.7$, respectively. The shower profile of the single γ is different from that of more than two γ's coming from the decay of π^0/η particle. The following strip chamber requirement therefore allows, to some extent, one to distinguish γ from π^0's and η particles:

$$\chi^2_a = 0.5 \times (\chi^2_{strip} + \chi^2_{wire}) \leq 4\,, \tag{3.2}$$

Here χ^2_{strip} and χ^2_{wire} are the fit chisquared values derived from central strip chamber shower profiles in wire and strip views, respectively; we use the average value of the two. Both strip and wire clusters are also required with approximately equal energies; i.e.

$$\frac{E_{strip} - E_{wire}}{E_{strip} + E_{wire}} < 0.2\,. \tag{3.3}$$

The fitted cluster centroids are further required to be well within the active region of the chamber: 14 cm $< |z_s| <$ 217 cm and $|x_s| <$ 17.5 cm, where z_s and x_s is the local coordinate system of the chamber (see Chapter 2.2). The hadronic-to-EM ratio (H/E) of the energy in the cluster is required to be less than $0.055 + 0.045 \cdot E/100$;

[4]The trajectory is defined by the event vertex and strip cluster coordinate.

[5]The energy of hadronic components is not included.

[6]The cone is formed around the centroid of the EM cluster.

E is the total (Hadronic+EM) cluster energy. Finally we require no track pointing at the towers in the cluster.

In the next section, we present a number of observables. Let us here describe the coordinate system in which we handle them. In the longitudinal dijet rest frame or photon-jet rest frame, we define the z' axis along the jet direction, and the y' axis along the direction of $\mathbf{p}_{beam} \times \hat{\mathbf{z}}'$, where $\mathbf{p}_{beam}$ is the 3-vector of the proton, and $\hat{\mathbf{z}}'$ is the unit vector along the z' axis. Here the jet direction is determined by the centroid of the calorimeter energy deposit. For each jet, we calculate the transformation matrix, which transforms all particle 3-vectors on the CDF global coordinate system into that on x'-y'-z' local coordinate system of the jet. We further boost the particles into a single jet rest frame, i.e. the center of mass system (CMS) of the jet itself, which is determined by taking internal invariant mass of the jet and its momentum. By this transformation, the x' and y' components of particle momentum are not changed.

3.4 π^0/γ ratio in photon candidates

As shown in fig. 3.1, the gluon fraction for $\gamma + jet$ events is very low, but that for the photon candidates in the real data is expected to be higher because of significant π^0/η contamination. In the case where most of the momentum of the parent parton is carried by a single neutral particle such as π^0 or η, the parton is sometime misidentified as a single photon. The dominant background to single photons are π^0's, and the background from $\eta \to 3\pi^0$ and $\eta \to 2\gamma$ are rather small. We therefore estimate π^0 background using the average strip χ^2_a distribution as follows.

We first generate π^0 with random angles and simulate the strip chamber response by the Monte Calro which incorporates the test beam electron response. The distribution of χ^2_a for the simulated π^0's is then calculated. The distribution

is normalized so that the π^0 data is equal to the high χ^2 ($4 < \chi^2_a < 25$) tail of the distribution for real data selected as direct photons without χ^2_a cut. Here we assume that the backgrounds are correctly modelled by single π^0's. We shall call direct photon data with χ^2_a greater than 5 "π^0 candidate" and denote it with the letters π^0_{cand}, and also denote photon candidate with χ^2_a less than 4 with the letters γ_{cand}.

Fig. 3.2 shows the χ^2_a distributions for direct photon data together with the distributions scaled for a π^0 background contribution for four p_t intervals. As mentioned before, strip chamber χ^2_a cut allows one to distinguish γ from π^0 by means of flag indicating one γ versus two γ showers. However at high E_t, the χ^2_a cut becomes useless, because photons from the decays coalesce with E_t and accordingly hit the same strip and wire in the strip chamber, and is consequently misidentified as a single photon. On the other hand at rather lower E_t, the χ^2_a cut again become useless, because the opening angle between two photons from the decays is so large that they make completely separated strip clusters and each of them is identified as a single photon as a result.

As mentioned before, $\pi^0 + jet$ events are provided by the case where one of the two outgoing partons fragments into very hard π^0. There is no reason to believe the gluon fraction of a handful of special case like this is equal to that for common dijet events. To check this, we generate a large amount of dijet events with Herwig, and make two sets of events; in which a) one of two partons fragments into π^0 with the momentum fraction $z > 0.7$, and b) π^0 with $z > 0.8$ is produced. We notice that the gluon fraction for $\pi^0 + jet$ events is less than that for dijet by about 10%. We also notice that the second case where $z > 0.8$ shows lower gluon fraction than the first case.

From the results shown in fig. 3.1 and fig. 3.3, i.e. the predicted gluon fraction for $\gamma + jet$ events, $F_g(\gamma + jet)$, and $\pi^0 + jet$ events, $F_g(\pi^0 + jet)$, and the γ fraction

(γ/π^0 ratio) in the photon candidates, F_γ, we may derive the gluon fraction in the real γ_{cand}+jet events as follows:

$$F_g(\gamma_{cand} + jet) = F_g(\gamma + jet) * F_\gamma + F_g(\pi^0 + jet) * (1 - F_\gamma) . \qquad (3.4)$$

In fig. 3.4 we show the resulting gluon fraction as a function of jet E_t. The data points are limited in the region below $E_t = 30$ GeV because of the difficulty in π^0 rejection.

3.5 Monte Calro sample

Since the analysis is strongly based on Monte Carlo's, we describe how to make Monte Carlo samples for gluon and quark jets in this section. We first produce quark and gluon jets in QCD $2 \rightarrow 2$ processes at $\sqrt{s}$ =1.8TeV, by using event generators, Herwig and Pythia. According to the two outgoing partons, the generated events are divided into two groups, quark and gluon samples. Here quark sample was taken from processes whose final states composed of two quarks, while gluon sample was from outgoing gluon-gluon processes: q g $\rightarrow$ q g process is not used.

In CDF three different detector simulation programs with different functions are available. The GEANT is useful for extrapolating detector performance to regions not measured in test beam, but is actually not used to simulate full events because of its extreme CPU requirements. A full detector simulation CDFSIM, with detailed modelling of detector geometry, materials, and interactions, is suitable for modelling physics signal, but also requires much CPU time. A fast detector simulation QFL [60] runs about ten times faster than CDFSIM, and is therefore useable for producing a high statistics sample. The calorimeter simulation within QFL incorporates a more realistic[7] version of the CDF geometry modelling the energy sharing between phototubes as in CDFSIM, includes a natural model of the

[7]The original QFL used a spherical model of the detector.

η cracks, tunes the calorimeter response for low energy pions on 1987 test beam data. For the tracking simulation, CDFSIM generates raw data, i.e. track-chamber hits, and then applies true pattern recognition, whereas QFL does not simulate raw data. However QFL does correctly model the momentum resolution with Gaussian fluctuation and simulate the effects of tracking pattern recognition: Moreover we can impose CTC track-finding efficiencies such as double-track resolution onto a QFL output bank. Hence the generated events are processed through QFL for detector simulation.

Next we reconstruct events in the same way as real data: The simulated events are clustered by JETCLU with the same parameters. The events are further divided into four samples, depending on the jet transverse energy E_t; 10−20,20−30,30−40 and 40−50 GeV. In each E_t range, 2000(quark)+2000(gluon) jets are finally produced. We shall call them "reference" jets.

Chapter 4

Analysis

4.1 Moment analysis

As was mentioned in chapter 1.5.2, some observables such as multiplicity, a jet angular width, etc., have been pointed out to show differences between quark and gluon jets. In this analysis, however, we do not try to find ad hoc variables which are more sensitive to the differences between the parton ancestors. Instead, we take a systematic approach of analyzing the momentum distribution (the fragmentation function) of charged particles in a jet by using the method of moment analysis. It is motivated by the fact that a function (the momentum distribution function in a jet in this case) of variables (the momenta of charged particles here) can generally be expressed by their moments as defined by the Mellin transformation. More terms of different orders reproduce the function more precisely. The moments of different orders in general are not mutually independent as probability variables. Considering the computer CPU time in the analysis on the one hand, we take about 30 variables in the present treatment.

The variables which we choose are mainly divided into two classes: one is the m-th power of the momentum, summed over all particles, which we call the "me-

chanical moment";

$$\sum_{i=1}^{n}(p_{li}/M)^m \; and \; \sum_{i=1}^{n}(p_{ti}/M)^m \; . \tag{4.1}$$

where the term $(p_i/M)^m$ represents the m-th power of the normalized momentum of the i-th charged particle, n is the total number of charged particles in a jet, and M is the jet invariant mass. The suffix l and t indicate the momentum components, longitudinal and transverse to the jet axis respectively. The other is the m-th power of the momentum multiplied by the electric charge of the particle and summed over all particles, which we call the "electric moment";

$$\sum_{i=1}^{n}C_i(p_{li}/M)^m \; and \; \sum_{i=1}^{n}C_i(p_{ti}/M)^m \; . \tag{4.2}$$

where C_i is charge of the i-th charged particle.

In this analysis, the moments defined by eqs. (4.1) and (4.2) are calculated in the jet rest frame which is obtained, as mentioned earlier, by the Lorentz transformation along the jet axis. The reason why we try this coordinate system is that the moment variables thus defined are Lorentz invariant and are expected to be less energy (mass in this system) dependent. In this treatment, however, a certain ambiguity is introduced for the definition of moments, because we usually have soft particles in the lab system about which we do not know whether they belong to the jet or to the underlying event. The soft components do not give substantial effects in the determination of the jet CM system, but they acquire large backward momenta by the Lorentz boost to the jet CM frame, giving non-trivial contributions to the values of moments. In order to remedy this flaw, we take sums only over particles whose momenta lie in a forward hemisphere of the jet CM momentum space.

The choice of variables to form a set is somewhat arbitrary. Here we take a variable set with integers, $m = -3, -2, -1, 0, 1, 2, 3, 4$, for powers of moments as shown in table 4.1. The negative power means that we deal with the inverse of the momentum instead of the momentum itself, and the 0-th power corresponds to the multiplicity of charged particles. By the uncertainty relation, the higher positive

moments provide information about the inner part of the jet in the ordinary space, while the higher negative moments about the outer part of the jet. In addition to the moments, we take three more measures; a) the ratio of the electromagnetic (EM) calorimeter response to the total (EM+HAD) calorimeter response (EM/TOTAL), b) the "asymmetry" and c) the "oblateness" of a jet. The asymmetry and the oblateness are measures about the non-uniform momentum distribution around the jet axis. For each jet, we calculate a tensor,

$$T_{x'x'} = \sum_{i=1}^{n} p_{ix'}^2, \tag{4.3}$$

$$T_{x'y'} = T_{y'x'} = \sum_{i=1}^{n} p_{ix'} p_{iy'},$$

$$T_{y'y'} = \sum_{i=1}^{n} p_{iy'}^2,$$

where the axes x' and y' are in the plane perpendicular to the jet axis (z-axis). The asymmetry is defined as

$$A = \frac{T_{y'y'} - T_{x'x'}}{T_{y'y'} + T_{x'x'}}, \tag{4.4}$$

where the x' axis is in the jet production plane and the y' axis is in the direction perpendicular to it. The oblateness O is defined by eigenvalues d_1 and d_2 ($d_1 > d_2$) of the T-tensor of eq. (4.3) as

$$O = \frac{d_1 - d_2}{d_1 + d_2}. \tag{4.5}$$

Finally we take into account the momentum correlation between two particles by defining the following variables:

$$\begin{aligned} C_+ &= \sum_{i,j} \{(\mathbf{p}_i - \mathbf{p}_j)^2\} / \{n_p(n_p - 1)\} \; and \\ C_- &= \sum_{i,j} \{(\mathbf{p}_i - \mathbf{p}_j)^{-2}\} / \{n_p(n_p - 1)\}, \end{aligned} \tag{4.6}$$

where each of the sums runs over all pair of jet particles: n_p is number of possible pairs and $\mathbf{p}$ is the particle 3-vector.

4.1.1 Moment distribution

In this section, we discuss the moment distributions for quark and gluon references. Also presented are the results of comparisons between the observed and the reference Monte Carlo (Pythia and Herwig) dijets.

Fig. 4.1 shows several distributions of the mechanical transverse moments in the logarithmic scale. These moments are calculated from the particle momenta transverse to the jet axis. Both distributions for references and real data are normalized so that the integrations of the distributions over the entire moment range are unity:

$$\int P_q(x)dx = \int P_g(x)dx = \int P_r(x)dx = 1, \tag{4.7}$$

where $P_q(x)$, $P_g(x)$ and $P_r(x)$ are distributions of a moment x for quark/gluon samples and real data, respectively. In the plots of negative power moments (i.e. -3rd, -2nd and -1st), gluon distributions peak at larger values than the quark distributions, whereas for positive power moments, gluon peaks are at smaller value than quark ones. It implies that the gluon jets are "fatter" than the quark jet. We also show the distributions of the "electric" transverse moments in fig. 4.2. These distributions show similar trend that gluon jets have larger values in the ordinary space (i.e. larger negative moments).

In the same way, the mechanical/electric longitudinal moments are calculated from longitudinal components of particle momenta. The resulting distributions for the mechanical and the electric moments are shown in fig. 4.3 and 4.4, respectively. In these figures, the gluon jets have larger values of the positive power moments (i.e. 4th, 3rd, 2nd and 1st), and smaller values of the negative power moments than quark jets. This means that fragments of quark jets are "harder" than that of gluon jets.

From figs. 4.1–4.4, we conclude that gluon jets are broader and contain more soft particles than quark jets: Hadrons from a quark are harder and more collimated than those from a gluon. We notice that the real dijet data overlap with gluon

reference almost completely, although the dijet sample should contain quark jets with the approximately 20% fraction at low E_t (10 GeV) and 30% at high E_t (50 GeV), according to the QCD prediction shown in fig. 3.1. We hence conclude that current fragmentation models underestimate the differences between gluon and quark jets, compared to what really is, i.e., the real gluon jet might be softer and broader than the Monte Carlo predictions. On the other hand, discrepancies between two Monte Calro generators are small, namely, both fragmentation models give similar predictions. This is understandable, because they are based on the same color-flow scheme as described in Chapter 1.4.

In fig. 4.5, we show the oblateness and the asymmetry. These two variables are defined in the dijet rest frame. The discrepancy of asymmetries between gluon and quark jets is less clear in the plot, while the oblateness plot shows that quark jets are more oblate than gluon jets. However, we should note here that the oblateness strongly depends on the charged multiplicity as shown in appendix B. As the multiplicity decreases, the jet has more chances to look oblate. The quark jet has lower charged multiplicity than the gluon jet as shown in fig. 4.6. Thus we cannot simply conclude here that quark jets are oblate than gluon jets. A contiguity motivation for the study of oblateness is that gluon polarization due to its spin may result in the oblate distribution of the final hadrons (see Appendix B). The present analysis is however too far to draw a conclusion about this problem.

Finally in fig. 4.6, we show the electromagnetic (EM) fraction of jets. We see that the gluon jet has a larger EM fraction than the quark jet: Fragments of the gluon jet have more chances to shower in the EM calorimeter. Since the EM fraction increases with number of produced π^0's in a jet and the gluon produces more π^0's than the quark because of its neutral charge, it is reasonable that the gluon jet gets a larger EM fraction. The correlation variables C_+ and C_- are also shown in fig. 4.7, but both gluon and quark data are distributed very likely. It is difficult to

judge the parton ancestor on the basis of C_+ and C_-, hence we decided not to use the correlation variables for the quark/gluon separation now.

4.2 Quark/gluon likelihood

Quark vs. gluon likelihood is calculated as follows. Let us denote the i-th moment by x_i (i = 1,2,...,n), and its distributions for quark and gluon sets by $P_q^{(i)}(x_i)$ and $P_g^{(i)}(x_i)$, respectively. A measure of the degree with which a jet with a moment x_i is more likely from a quark than from a gluon is the log-likelihood $L_i(x_i)$, defined by

$$L_i(x_i) = \ln\left[\frac{P_q^{(i)}(x_i)}{P_g^{(i)}(x_i)}\right] , \tag{4.8}$$

where the integrations of the distribution functions over x_i's are normalized to unity (see eq. (4.7)). The next question is how to integrate the information on the likelihood L_i's obtained from individual moments to get a "global" likelihood. If the moments x_i's are mutually independent probability variables, the global likelihood is a simple sum of L_i's. The distributions of moments are actually not independent. For simplicity of the treatment, we shall here take an equal-weighted sum, but also introduce one scale parameter to represent the effect of correlations among variables. Thus in the present analysis, the global likelihood is defined by

$$L' = \lambda \sum_{i=1}^{n} L_i = \lambda L , \tag{4.9}$$

where λ is a scale parameter. We will denote the difference of the means of L (L') for quark and gluon reference jets by Δ (Δ'), and the combined deviation for the two references by σ (σ'). As shown in Appendix A, if the global likelihood distributions are symmetric Gaussian functions, L' is the proper likelihood with the scale factor:

$$\lambda = \frac{\Delta}{\sigma^2} . \tag{4.10}$$

The figure of merit or the separation power of the global likelihood can be defined as

$$S = \frac{\Delta'}{\sigma'}\,, \tag{4.11}$$

which is equal to σ' for the proper likelihood.

Let us next consider the errors of the likelihood. The errors of individual likelihood, σ_{Li}'s, are mutually correlated, but we assume that the effect is again represented by the scale factor λ, and that the uncertainty of the global likelihood, $\sigma_{L'}$, is given by

$$\sigma_{L'} = \lambda\sqrt{\sum \sigma_{Li}^2}\,. \tag{4.12}$$

The likelihood L_i is evaluated from the distribution functions $P_q(x_i)$ and $P_g(x_i)$ by eq. (4.8), hence its error is given by

$$\sigma_{Li} = \sqrt{\left(\frac{\sigma_q^{(i)}}{P_q^{(i)}}\right)^2 + \left(\frac{\sigma_g^{(i)}}{P_g^{(i)}}\right)^2 + \left(\frac{1}{P_q^{(i)}}\cdot\frac{\partial P_q^{(i)}}{\partial x_i} - \frac{1}{P_g^{(i)}}\cdot\frac{\partial P_g^{(i)}}{\partial x_i}\right)^2 \sigma_{xi}^2}\,. \tag{4.13}$$

There are several sources of uncertainties which contribute to σ_{Li}, in particular when we deal with real data provided by experiments. The uncertainties are of two kinds: One is that of the distribution functions themselves, $\sigma_q^{(i)}$ and $\sigma_g^{(i)}$, due to our imperfect knowledge of the fragmentation. The other is the error in the experimental determination of x_i, σ_{xi}, which is a combination of systematic effects due to clustering, and detector originated uncertainties such as low energy calorimeter responses, calibration systematic errors, finite detector resolution and simulation uncertainties. We however do not assign here the errors from these σ_{xi} to σ_{Li}, just for simplicity. Note that the σ_{xi}^2 term in eq. (4.13) has a coefficient which is small when the $P_q^{(i)}$ and $P_g^{(i)}$ are nearly equal as in the present case. Thus, we ignore the third term on the right hand side of eq. (4.13), and take the statistical errors for $\sigma_g^{(i)}$ and $\sigma_q^{(i)}$, which are due to the finite number of events in a given x_i-bin in the reference data sets.

In the actual analysis described in this paper, the histogram of each moment was divided into 50 bins, and the total binwidth was chosen wide enough. The statistical errors, $\sigma_q^{(i)}$ and $\sigma_g^{(i)}$, are assigned to each bin, assuming a Gaussian fluctuation. It is to be noted that this kind of statistical error can be reduced as much as one likes by accumulating the reference jet data.

Finally, we take eq. (4.12) as the error of L' for a jet, and make a smoothing of the L' distribution, supposing that L' is distributed with a Gaussian with uncertainty $\sigma_{L'}$.

The next subject is the discriminating powers of individual moments. To quantify them, we use the figure of merit for the i-th moment defined by

$$s_i = \frac{\Delta_i}{\sigma_i}\,, \tag{4.14}$$

where Δ_i and σ_i are equivalents of Δ and σ for the i-th moment. Figs. 4.8a–h show the figures of merit given for 30 moments of jets in some E_t interval (10–20, 20–30, 30–40, 40–50 GeV). In these figures the letters, MT, ET, ML and EL followed by positive/negative numbers (the power of moment) mean Mechanical transverse moment, Electrical transverse moment, Mechanical longitudinal moment and Electrical longitudinal moment, respectively. The other four letters, EMFR, MULT, OBLT and ASYM refer to the electro magnetic fraction of a jet, charged multiplicity within a jet, oblateness of jet and asymmetry of jet fragments, respectively. Assignments of variable numbers to moments are listed in Table 4.1. We note that some variables, for instance, multiplicity and a moment ML−1, have rather large figures of merit, while the asymmetry or MT−1 shows a quite small figure of merit. As the jet energy increases, the difference between *useful* moments with relatively strong separation powers and *useless* moments with weak ones becomes clearer. This is due to the fact that as the energy increases, more and more hadrons are produced, thus the statistical fluctuation in the momentum distribution become substantially smaller. In fig. 4.8a (Herwig, $10 < E_t < 20$ GeV), the negative transverse moments,

MT−1, −2 and −3 show larger figures of merit than positive moments MT+1, +2, and +3, while at a higher energy range, the negative moments show smaller figures of merit than the positive ones. It means that the energy dependences of individual moments are different, and in addition, at the low energy statistical fluctuations is large as mentioned before. Also, the results from two Monte Carlo generators show a rough agreement, although at $E_t > 30$ GeV, Pythia shows clearer differences between *useful* and *useless* moments rather than Herwig. In fig. 4.8e, for example, figures of merit for some *useful* moments are close to 1, whereas that for some *useless* moments are almost zero.

4.3 Results

The resulting global likelihood shows different distributions $Q(L')$ for quarks and $G(L')$ for gluons as presented in fig. 4.9. Thus when given a data set to analyze, which we will call an "analysis" sample, we can determine a quark vs. gluon likelihood for each jet in the sample. The data are presented in four different E_t ranges. We note that the width of the distribution of gluon is narrower than that of quark, and quark shows more tail in the positive side. In addition this tail becomes larger with jet energy, and accordingly the separation between two histograms becomes better. The separation power of the highest E_t (40−50 GeV) samples generated with Herwig and Pythia are 0.86 and 0.91, respectively. These values are about 1.4 times larger than those of the lowest ones (10−20 GeV). This behavior can be accountable in terms of the fact that the separation power of each moment becomes larger with energy because of smaller statistical fluctuation, and the resulting global likelihoods are distributed with clearer separation between the two sets. We also see that the separation power of Pythia is slightly bigger than that of Herwig, but this may be less important, because it does not mean that Pythia is superior to Herwig. We can not speak of speriority of a model without comparing each moment with

that of the real data.

One can use the global likelihood as a criterion to select quark jets. For example, by cutting jets below a certain level of the likelihood L'_c, we can enhance the quark-to-gluon ratio and obtain a signal-richer sample accordingly. The signal-to-background ratio is then given by

$$r = \frac{N_q \int_{L'_c}^{\infty} Q(L')dL'}{N_g \int_{L'_c}^{\infty} G(L')dL'}, \tag{4.15}$$

where N_q and N_g are numbers of jets in analysis sample respectively. This technique becomes less useful in case that the original sample contains much larger amount of gluon jets.

Fig. 4.10 shows global likelihood distributions for dijet events and the γ_{cand}+jet events. Like the previous figure, the data are shown in four jet E_t interval. Recalling the results in chapter 3.3.2 and 3.4, we see that the dijet events show a very good agreement with gluon-rich hypothesis. The γ_{cand}+jet sample still contains π^0+jet events by approximately 40% level (see previous chapter). We then expect that γ_{cand}+jet data are between quark and gluon references. In fact γ_{cand}+jet data show a good agreement with this hypothesis. In particular two peaks of γ_{cand}+jet in fig. 4.10c represent this situation well. Needless to say, the peak with higher likelihood are from quark jets, and the lower peak are from gluon jets in the sample. In fig. 4.10d, the distributions for γ_{cand}+jet data is not smooth, and this is due to the poor statistics[1].

We can also determine the fraction of the gluon (or quark) jets in a given analysis sample without any cut. The predictions from two references are fit to the analysis sample in a form:

$$D_i = X_g G_i + (1 - X_g) Q_i \tag{4.16}$$

[1] number of γ_{cand}+jet events is 78.

by finding the coefficient X_g which minimizes the chi-squared defined by

$$\chi^2 = \sum_{i=1}^{50} \left[\frac{D_i - (X_g G_i + (1 - X_g) Q_i)}{\sigma_i} \right]^2 . \quad (4.17)$$

In eqs. (4.16) and (4.17), G_i, Q_i, and D_i are (normalized) numbers of jets in the i-th bin of the likelihood histograms for gluon, quark, and analysis samples respectively; σ_i is an error on D_i: $\sqrt{D_i}$. In fig. 4.11, we plot χ^2 as a function of the gluon fraction X_g for two kinds of simulated samples: dijet produced from all QCD $2 \rightarrow 2$ processes and jet associated with direct gamma production. The true values of gluon fraction as directly given by Monte Calro generators in the dijet and jet+γ events are 80% and 20% respectively. We note that in fig. 4.11 a good agreement is found between the estimated and true value of X_g. The result represents the self consistency of the method, and an agreement between two Monte Calro generators suggests the stability of this method.

Using this fitting technique, we determine the gluon fraction in the real data. But before doing so, let us describe the errors on the resulting gluon fraction. As usual, the errors are independent of the χ^2 at minimum, χ^2_{min}, and given by the set of $X_g^{(-)}$ and $X_g^{(+)}$ such that

$$\chi^2(X_g^{(-)}) = \chi^2(X_g^{(+)}) = \chi^2_{min} + 1 . \quad (4.18)$$

To be sure that this error estimation is appropriate, we have performed the following check reported in figs. 4.12 and 4.13. We produced 200 different samples which contains 2000 events. The quark/gluon of each sample is in the ratio 7:3. The gluon fraction and its error given by eq. (4.18) are calculated on an sample-by-sample basis. In these figures, "*R.M.S*" refers to the deviation of the gluon fraction distribution from its mean, and "$\chi^2 error$" refers to the mean value of gluon fraction errors given by eq. (4.18). The error bars of *R.M.S* and $\chi^2 error$ are the standard deviation of the *R.M.S.* in the gluon fraction distribution, and that of the gluon fraction error distribution. The error given by eq. (4.18) shows a approximately

agreement with one-standard-deviation limit on the determinations of X_g. We also notice that, is natural, the error becomes smaller as separation power σ' increases. Futhermore, as the number of events, N, increases, the error becomes smaller; thus the error is approximately proportional to $1/\sqrt{N}$ as shown in fig. 4.13.

In fig. 4.14, we show the fraction of the final state gluon in the dijet events, γ_{cand}+jet events, and π^0_{cand}+jet events sample in which strip χ^2_a is greater than 5, as a function of jet transverse energy E_t. We have given at the end of chapter 3, in figs. 3.1 and 3.3, the expected gluon fraction for these three types of events. The γ_{cand}+jet data shows good agreement with the expected fraction in fig. 3.4, but unfortunately we have no expected point at higher E_t. For dijet data, the agreement is good for high E_t (>30 GeV), but has not overlap at low E_T, in which the real data show higher gluon fractions. For π^0_{cand}+jet data, which is considered as the special case of QCD $2 \rightarrow 2$ processes, the gluon fraction agrees with the prediction of Herwig.

In fig. 4.14b, the γ_{cand}+jet data overlap with the π^0_{cand}+jet data at high E_t, whereas in fig. 4.14a it is still different from the dijet event. We can not tell which is correct, because we have no chance to know the γ/π^0 ratio in high E_t range with CDF detector, and can not estimate the gluon fraction as a result. However, in both figures, the dijet data is significantly different from γ_{cand}+jet events.

According to the good agreement between the results and the expected, the prediction of two Monte Carlo models, i.e. string fragmentation and cluster fragmentation models, are rather good. At low E_t, both models tend to overestimate gluon fraction. This may be related either to the treatment of real data (for example, the jet energy calibration or detector simulation, both which are sources of the systematic uncertainty, as mentioned in Section 4.2) or to the problem with Monte Carlo generators.

Chapter 5

Conclusions

The fragmentation properties of jets in $\bar{p}p$ collisions at $\sqrt{s} = 1.8$ TeV have been studied by the CDF experiment at Fermilab. We have shown that there are characteristic differences between quark and gluon jets, and the differences are consistent with current QCD-based ideas about the jet fragmentation.

The fundamental notion of colored-partons, i.e. quarks and gluons, is revolutionary because of the apparent confinement of these objects. This notion emerged out of the hadron spectroscopy and was later established by the successes of the description of the strong interaction in terms of the perturbative QCD. The successes of the quark-parton model stimulated interest in the possible discriminaion of the quark/gluon jets, and various works were carried out in some e^+e^- annihilation experiments and the CERN $\bar{p}p$ collider experiments. Our approach differs in several ways from these studies.

The QCD can not directly address the question of interpreting actual experimental data of fragmentation because of its non-perturbative nature. Thus, we resort to the phenominological hadronization models. A number of developed models including both QCD-based and non-QCD ones, have had some success in describing many features of jet production, such as cross-sections, angular distributions. The key feature for QCD-inspired fragmentation model is the approximation of planer

color flow, which naturally generates jet-like configurations and predicts the differences between quark and gluon jets. However in the non-QCD fragmentation models, e.g. the independent fragmentation model, the quark and gluon jet properties are assumed to be the same because of the absence of the specific model of gluons. Hence in this analysis, we use two Monte Calro programs, Herwig and Pythia, which are based on colored fragmentation and describe coherent pictures of the $\bar{p}p$ interaction by including hard scattering matrix elements, structure functions, initial and final parton showers, and Cluster and String fragmentation models based on QCD.

The generated events are processed through a detector simulation which reproduces the CDF detector realistically, and then clustered by a jet window-type finding algorithm called JETCLU. The proposed method is based on these simulated quark and gluon reference jets. Various variables, such as mechanical/electric moments, multiplicity, and EM fraction, are calculated for the reference jets. Their resulting distributions suggest that gluon jets are softer and broader than quark jets, reflecting the nature of the double color charge of the gluon. The reference jets are compared with real dijet events of the CDF experiment. The real data show strong preference for gluon-like behaviour. This is consistent with the QCD prediction: the gluon jet is dominant at the CDF energy. According to the figure of merit defined in eq. (4.14), some variables, e.g. multiplicity and a moment ML$-$1, are rather efficient for quark/gluon separation, while the asymmetry or MT$-$1 is less efficient.

We have proposed statistical approach to improve the discrimination power, i.e., each jet is characterized in global likelihood which is a simple sum of all log-likelihood functions derived from 30 different variables. This results in a bigger figure of merit than that of a single most effective variable.

The global likelihood for real dijet events are again distributed much like gluons,

and that for γ_{cand}+jet events, in which the jet is associated with a photon candidate γ_{cand} with χ^2 for its lateral shower profile in the strip chamber less than 4, are distributed like the mixture of gluons and quarks. The quark sample has more tail in the positive side of the global likelihood. Removing the gluon-like range of the global likelihood, one can enhance quark-to-gluon ratio, thus suppressing the QCD gluon jet events. This procedure is suggested to be useful in search for new particles which predominantly decay into quarks.

Finally, the gluon fraction in a given sample is determined by fitting its global likelihood distribution to the superposition of two distributions for quark and gluon samples. The dijet data shows approximately 80% gluon fraction, and the γ_{cand}+jet data shows about 40% gluon fraction in the jet transverse energy (E_t) range of 10–30 GeV. These results agree within the error with the gluon fraction determined from theoretical prediction and the expected π^0/γ ratio in the photon candidates, except that some disagreement for dijet event is observed at low energy. This discrepancies might be caused by inadequacy of the simulation for low energy jets. In addition, π^0+jet data agree quite well with the Monte Carlo simulation, in which very hard π^0's (with momentum fraction $z > 0.7, 0.8$) are assumed to be generated. Moreover, both dijet and π^0+jet data reproduce the expected E_t dependence of the gluon fraction, i.e. the fraction 0 gradually decreases with E_t.

Tables

Subprocess	Squared matrix element
$q_i q_j \to q_i q_j$	$\langle\frac{2}{9}\rangle 2\frac{\hat{s}^2+\hat{u}^2}{\hat{t}^2} + \delta_{ij}[\langle\frac{2}{9}\rangle 2\frac{\hat{t}^2+\hat{s}^2}{\hat{u}^2} + \langle-\frac{2}{27}\rangle\frac{4\hat{s}^2}{\hat{u}\hat{t}}]$
$q_i \bar{q}_j \to q_i \bar{q}_j$	$\langle\frac{2}{9}\rangle 2\frac{\hat{t}^2+\hat{u}^2}{\hat{s}^2} + \delta_{ij}[\langle\frac{2}{9}\rangle 2\frac{\hat{u}^2+\hat{s}^2}{\hat{t}^2} + \langle-\frac{2}{27}\rangle\frac{4\hat{u}^2}{\hat{s}\hat{t}}]$
$gg \to q\bar{q}$	$\langle\frac{1}{12}\rangle 2\frac{\hat{u}^2+\hat{t}^2}{\hat{u}\hat{t}} - \langle\frac{3}{16}\rangle 4(1-\frac{\hat{u}\hat{t}}{\hat{s}^2}) + \langle\frac{3}{32}\rangle 4$
$q\bar{q} \to gg$	$\langle\frac{16}{27}\rangle 2\frac{\hat{u}^2+\hat{t}^2}{\hat{u}\hat{t}} - \langle\frac{4}{3}\rangle 4(1-\frac{\hat{u}\hat{t}}{\hat{s}^2}) + \langle\frac{2}{3}\rangle 4$
$gq \to gq$	$-\langle\frac{2}{9}\rangle 2\frac{\hat{u}^2+\hat{s}^2}{\hat{u}\hat{s}} + (\langle 2\rangle - 1)\frac{\hat{s}^2+\hat{u}^2}{\hat{t}^2}$
$gg \to gg$	$(\langle 2\rangle - 1)\frac{9}{2}(3 - \frac{\hat{u}\hat{t}}{\hat{s}^2} - \frac{\hat{t}\hat{s}}{\hat{u}^2} - \frac{\hat{s}\hat{u}}{\hat{t}^2})$

Table 1.1: Squared matrix elements for $2 \to 2$ parton-parton scattering in lowest order. The color factors are in brackets "$\langle..\rangle$". The variables $\hat{s}$, $\hat{t}$, $\hat{u}$ correspond to the Mandelstam invariants for the parton-parton subsystem.

Tracking	Inner layer	Outer layer
VTPC	0–3.5	0–2.6
CTC	0–2	0–1
CDT	0–1	0–1
FTC	2.4–4	2.4–4
Calorimeter	**EM**	**Hadron**
Central	0–1.1	0–0.9
Endwall		0.7–1.3
Endplug	1.1–2.4	1.3–2.4
Forward	2.2–4.2	2.3–4.2

Table 2.1: The regions in pseudo-rapidity $|\eta|$ covered by the tracking chambers and calorimeters

Items	Parameters
Vacuum vessel	
Diameter; outer/inner	3353 mm/2858 mm
Length	5067 mm
Material	A5083 aluminum
Wall thickness; outer/inner	20 mm/7 mm
Central field	1.5 T
Material thickness	0.85 radiation length
Total weight	11 t
Cold mass	5.6 t
Coil	
Current	5000 A
Inductance	2.4 H
Stored energy	30×10^6 J
Number of turns	1164
Winding scheme	Single layer helix
Supporting structure	Shrink-fit assembly with outer support cylinder; no inner bobbin
Conductor	
NbTi/Cu/Al ratio	1/1/21
Dimensions	3.89×20.0 mm^2
NbTi filaments	Nb–46.5 Ti, 50 μm diameter × 1700
Standard short sample current	10.4 kA at 1.5 T and 4.2 K
Purity of aluminum stabilizer	~ 99.999%
Outer support cylinder	
Material	A5083 aluminum
Thickness	16 mm
Liquid helium cryogenics	Forced flow two-phase
Liquid nitrogen cryogenics	Forced flow

Table 2.2: Parameters of the CDF solenoid

Modules	
12/arch + 2 spare	50
Length	98 in.
Width	(17.9 in. at 68 + in. from beamline)
Depth (including base plate)	13.6 in.
Weight	2 tons
Towers	
10/module	478
Length	0.11 $\Delta\eta$ ($\frac{1}{2}$ of width)
Thickness (see table 2)	18 X_0, 1 L_{abs} (+ coil etc.)
Layers	20–30 lead
	21–31 scintillator
	1 strip chamber
Lead	$\frac{1}{8}$ in. aluminum clad
Scintillator	5 mm SCSN-38 polystyrene
Wavelength shifter	3 mm Y7 UVA acrylic
Photomultiplier tubes (956 channels)	Hamamatsu R580 ($1\frac{1}{2}$ in.)
Chambers (see table 4)	
Depth	5.9 X_0 (including coil)
Wire channels (64/module)	3072
Strip channels (128/module)	6130
Angular coverage	
θ	about 39° –141°
ϕ	complete
Pseudorapidity	about ±1.1
Performance (high = 30 + GeV)	
pe/GeV	100 + /tube
Energy resolution σ/E [GeV]	$13.5\%/\sqrt{E}$
Position resolution (high)	±2 mm
Strip/wire PH correlation	8–10%
Wire PH resolution (high)	±25%
Hadron rejection (at 50 GeV) without strip chamber information	$(2\text{–}3)\times 10^{-3}$

Table 2.3: Characteristics of the central electromagnetic calorimeter

Perpendicular distance to beam line	184 cm
Wire channels (64)	
Extrusion	3 piece aluminum
Cell	0.250 in. deep by 0.239 in.
Wall	0.047 in. (16.4%)
Wire	0.002 in. Au-plated W
Readout	RABBIT
Split	121.2 cm from 90° edge
Ganging	pairs except edges (1.453 cm)
Blocking capacitor	200 pF
Strip channels (128)	
Section 1	6.2–121.2 cm from 90° edge
Strips	69 × 1.67 cm
Section 2	121.2–239.6 cm from 90° edge
Strips	59 × 2.01 cm
Total thickness	0.75 in.
	0.069 radiation lengths
	0.022 adsorption lengths
High voltage	1420 V
Feedin	separate by logical channel
Cable	stripped RG-174
Protection	1 MΩ on board
Gas	95%/5% Ar/CO_2
Flow	parallel

Table 2.4: Characteristics of the central strip chamber

Modules	
Number of modules	48
Length	2.5
Width (in ϕ direction)	1.33 m
Weight per module	12000 kg
Towers	
Total number (8/module)	384
Length ($\Delta\phi = 15^0$)	0.56–0.91 m
Width ($\Delta\eta = 0.11$)	0.28–0.45 m
Total depth	
(hadron calorimeter alone)	$4.7\Lambda_{abs}$
Layers	
Number	32
Steel thickness	2.5 cm
Scintillator thickness	1.0 cm
Scintillator type	PMMA doped with 8% naphtalene 1% butyl-PBD and 0.01% POPOP
Wavelength shifters	UVA PMMA doped with 30 mg/l layer dye #481
Number of phototubes	768

Table 2.5: Parameters of the central hadron calorimeter

Modules	
Number of modules	48
Approximate dimensions	$0.8 \times 1.0 \times 1.1$ m^3
Weight per module	7000 kg
Towers	
Total number (6/module)	288
Length ($\Delta\phi = 15^0$)	0.35–0.78
Width ($\Delta\eta = 0.11$)	0.25–0.40
Total depth	
(hadron calorimeter alone)	$4.5\ \Lambda_{abs}$
Layers	
Number	15
Steel thickness	5 cm
Scintillator thickness	1.0 cm
Scintillator type	PMMA doped with 8% naphtalene 1% butyl-PBD and 0.01% POPOP
Wavelength shifters	UVA PMMA doped with 30 mg/l laser dye #481
Number of phototubes	576

Table 2.6: Parameters of the endwall hadron calorimeter

$\theta = 11°$	30°	Chamber no.	
1.24	$1.41X_0$	1	Pad long. segment–I
		2	
		...	
3.33	$3.78X_0$	5	
3.86	$4.37X_0$	6 θ-strip no. 1	Pad long. segment–II
		7 ϕ-strip no. 1	
		8 θ-strip no. 2	
		9 ϕ-strip no. 2	
		10 θ-strip no. 3	
		11 ϕ-strip no. 3	
		12 θ-strip no. 4	
		13 ϕ-strip no. 4	
		14 θ-strip no. 5	
8.57	$9.71X_0$	15 ϕ-strip no. 5	
		16	
		17	
		...	
15.89	$18.01X_0$	29	
16.41	$18.60X_0$	30	Pad long. segment–III
		31	
		...	
18.50	$20.97X_0$	34	

Table 2.7: Longitudinal layer configuration of the PEM

Energy resolution (pad)	$28\%/\sqrt{E}$
Angular resolution	
Second pad segment	$\Delta\theta$: 0.04° –0.2°
	$\Delta\phi$: 0.2° –0.3°
θ-strips	$\Delta\theta$: 0.04°
ϕ-strips	$\Delta\phi$: 0.1°
Linearity at 200 GeV	
1.8 kV	−16%
1.7 kV	−7% (−4% leakage inclusive)
Gain uniformity	
(anode wire)	rms $\lesssim$ 2.5%
Gain monitoring	rms $\lesssim$ 0.5%
Pion rejection	
(electron efficiency 60–80%)	500–1000 (100 GeV)

Table 2.8: Performance of the PEM

Dimensions	
Number of modules	8
Module length	35.3 cm
Modules spacing	35.94 cm
Maximum active radius	21 cm
Minimum active radius	7 cm
Drift length	15.25 cm
End caps	
Sense wires	24/octant 6.336 mm spacing 15 μm gold-plated tungsten
Field wires	24/octant 63 μm copper/beryllium
Cathode pads	24 pads/octant, in 3 rows 4.12 cm in r by $\approx$ 1.4 cm in $r-\phi$
Resistive ink	10 MΩ/square
Field cage	
Material	Kapton/Rohacell foam laminate epoxy/graphite-foam support frame
Electrodes	3.175 mm overlapping strips on 2.38 mm centers
Central grid	ss screen 50 μm wires on 1000 μm centers
Cathode grid	ss screen 50 μm wires on 500 μm centers
Magnetic field	
B_{axial}	1.5 T
B_{radial}(max)	$<1\%$ B_{axial}
Drift field	
E_{drift}	256 V/cm
Gas	
Argon-ethane	50/50 at 1 atm
Drift velocity	42 μm/ns
Voltages	
Cathode	-2.5 kV
Field shaping	-1.6 kV
Central grid	-6.4 kV
Sense wire	ground
Electronics	
Number of wire channels	3072
Number of pad channels	768
Number of dE/dx channels	768

Table 2.9: VTPC specifications

Number of layers	84
Number of superlayers	9
Stereo angle	0° +3°0° −3°0° +3°0° −3°0°
Number of super cells/layer	30, 42, 48, 60, 72, 84, 96, 108, 120
Number of sense wires/cell	12, 6, 12, 6, 12, 6, 12, 6, 12
Sense wire spacing	10 mm in plane of wires
Tilt angle (center of plane)	45°
Radius at intermost sense wire	309 mm
Radius at outermost sense wire	1320 mm
Wire length	3214.0 mm
Sense wire diameter/tension	40 μm gold plated tungsten/135 g
Potential wire diameter/tension	140 μm stainless steel 304/661 g
Field wire diameter/tension	178 μm stainless steel 304/429 g
Guard wire diameter/tension	254 μm stainless steel 304/875 g 305 μm stainless steel 304/1259 g
Shaper wire diameter/tension	305 μm stainless steel 304/1259 g
Total number of wires	36, 504
Total wire tension	25 ton
Endplate	2 in. aluminum 6061-T6(51)
Outer can	0.250 in. aluminum
Inner support cylinder	0.080 in. carbon fiber reinforced plastic
Gas	argon-ethane-alcohol (49.6% : 49.6% : 0.8%)
Drift field (E_0)	-1350 V/cm
Drift field uniformity	$dE_0/E_0 - 1.5\%$ (rms)

Table 2.10: Mechanical parameters of the CTC

Gain	3×10^4 (250 ns gate)
Resolution	<200 μm per wire
Efficiency	>0.98 per point
Double track resolution	<5 mm or 100 ns
Maximum drift distance	40 mm
Maximum hits per wire	>7
Stereo angle	$\pm3°$
Z resolution	<0.200 mm/sin 3°) = 4 mm
Momentum resolution	$dP_t/P_t < 0.001$ P_t (in GeV/c at 90°)

Table 2.11: Performance of the CTC

Outer radius	72.5 cm
Inner radius	12.5 cm
Wire length of sensitive volume	60 cm
Minimum drift distance	5.4 mm
Maximum drift distance	28.3 mm
Sense wire	50 μm gold plated tungsten and 50 μm Stablohm (for current division)
Field wire	150 μm stainless steel 304
Cathode strips	25 μm thick, 6 mm wide on 125 μm G10
Total number of wires	6768
Total number of sense wires	3024
Wire tension	40 g
Cathode plane tension	2.5 kg (each)
Chamber volume	0.5 m^3 (total volume 2 m^3)

Table 2.12: Mechanical specifications of the FTC

MEASURE	CLUST2	CLUST3	CLUST4	JETCLU
CPU/event (VAX 8650 sec)	0.075	0.093	0.141	0.063
Fraction (2 clus. $E_t > 15.$)	55%	60%	61%	66%
Embedded	3%	0%	0%	0%
Large	1%	0%	0%	0%
Mean η width	0.73	0.82	0.78	0.95
Mean ϕ width	1.21	1.17	1.25	1.26
$\Delta Et\ (GeV)$	0.96	0.72	0.90	0.43
Merging distance	0.62	0.64	0.71	0.79
Merging sharpness	0.19	0.14	0.22	0.15
Merge dist ($E_t > 25\,GeV$)	0.77	0.67	0.65	0.81
Merge sharp($E_t > 25\,GeV$)	0.17	0.07	0.33	0.12
Pt resolution (GeV)	13.4%	13.0%	11.3%	11.4%

Table 3.1: Perfomance of the CDF jet clustering algorithms

Variable #	Moment name	Moment definition
1	MT−3	$\sum(p_{ti}/M)^{-3}$
2	MT−2	$\sum(p_{ti}/M)^{-2}$
3	MT−1	$\sum(p_{ti}/M)^{-1}$
4	MT+1	$\sum(p_{ti}/M)^{1}$
5	MT+2	$\sum(p_{ti}/M)^{2}$
6	MT+3	$\sum(p_{ti}/M)^{3}$
7	ET−3	$\sum c_i \cdot (p_{ti}/M)^{-3}$
8	ET−2	$\sum c_i \cdot (p_{ti}/M)^{-2}$
9	ET−1	$\sum c_i \cdot (p_{ti}/M)^{-1}$
10	ET+1	$\sum c_i \cdot (p_{ti}/M)^{1}$
11	ET+2	$\sum c_i \cdot (p_{ti}/M)^{2}$
12	MT+3	$\sum c_i \cdot (p_{ti}/M)^{3}$
13	EMFR	Et_{EM}/Et_{total}
14	MULT	multiplicity
15	OBLA	oblateness
16	ASYM	asymmetry
17	ML−3	$\sum(p_{li}/M)^{-3}$
18	ML−2	$\sum(p_{li}/M)^{-2}$
19	ML−1	$\sum(p_{li}/M)^{-1}$
20	ML+1	$\sum(p_{li}/M)^{1}$
21	ML+2	$\sum(p_{li}/M)^{2}$
22	ML+3	$\sum(p_{li}/M)^{3}$
23	ML+4	$\sum(p_{li}/M)^{4}$
24	EL−3	$\sum c_i \cdot (p_{li}/M)^{-3}$
25	EL−2	$\sum c_i \cdot (p_{li}/M)^{-2}$
26	EL−1	$\sum c_i \cdot (p_{li}/M)^{-1}$
27	EL+1	$\sum c_i \cdot (p_{li}/M)^{1}$
28	EL+2	$\sum c_i \cdot (p_{li}/M)^{2}$
29	EL+3	$\sum c_i \cdot (p_{li}/M)^{3}$
30	EL+4	$\sum c_i \cdot (p_{li}/M)^{4}$

Table 4.1: List of variables. P_{li} is the i-th charged particle momentum along the jet axis; P_{ti} is the i-th charged particle momentum transverse to the jet axis; c_i is the charge of the i-th particle; M is the jet invariant mass; asymmetry and oblateness of the jet are defined in terms of the charged particle momentum flow in a jet (see eqs. 4.3 and 4.4); Et_{EM}/Et_{total} is the EM energy fraction of jet.

Figures

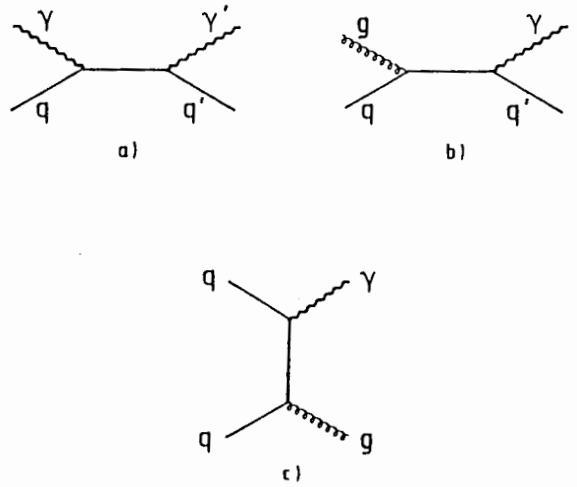

Figure 1.1: Some Feynman diagrams for direct photon productions in hard hadron interactions.

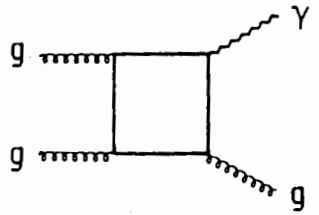

Figure 1.2: Production of the direct photon via gluon-gluon fusion.

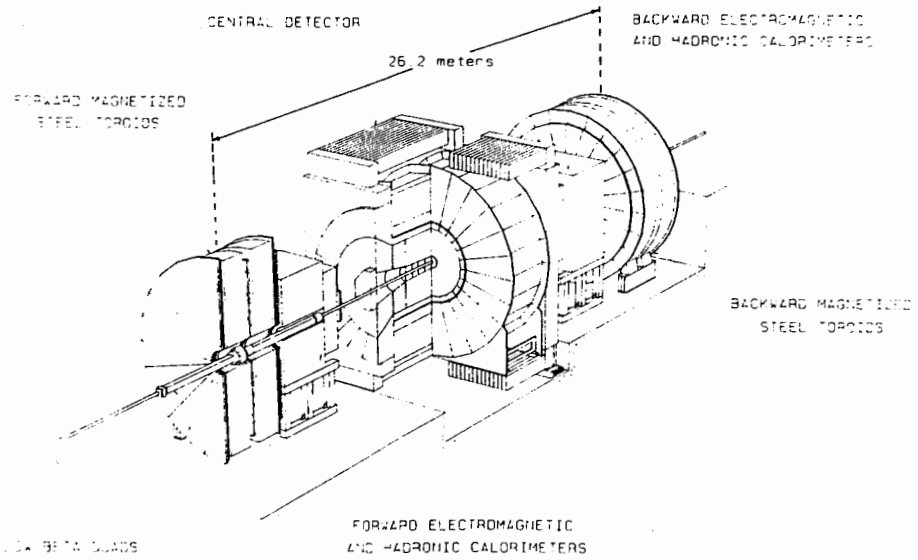

Figure 2.1: A perspective view of the CDF detector showing the central detector and two identical forward/backward detectors.

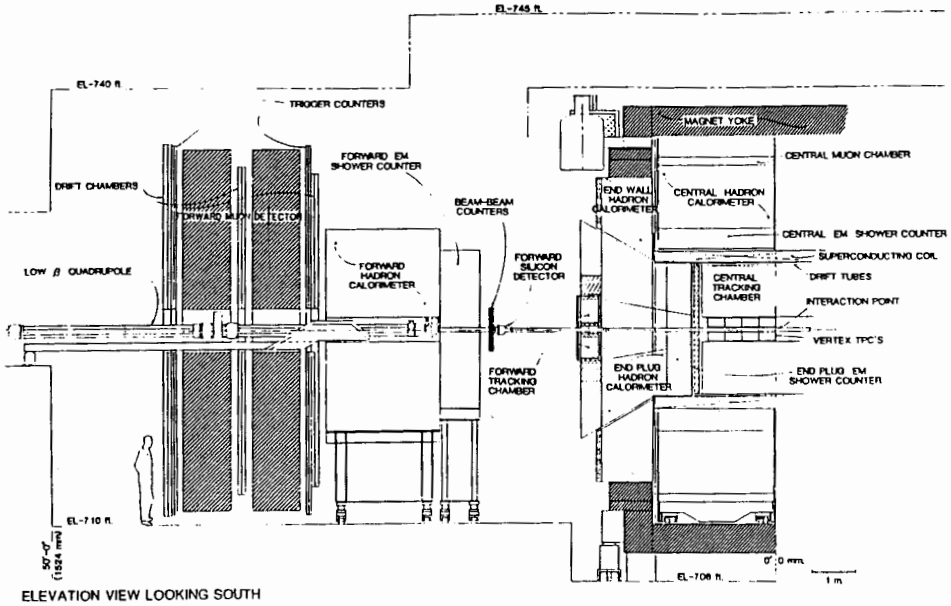

Figure 2.2: Cross section through a vertical plane of one half the CDF detector.

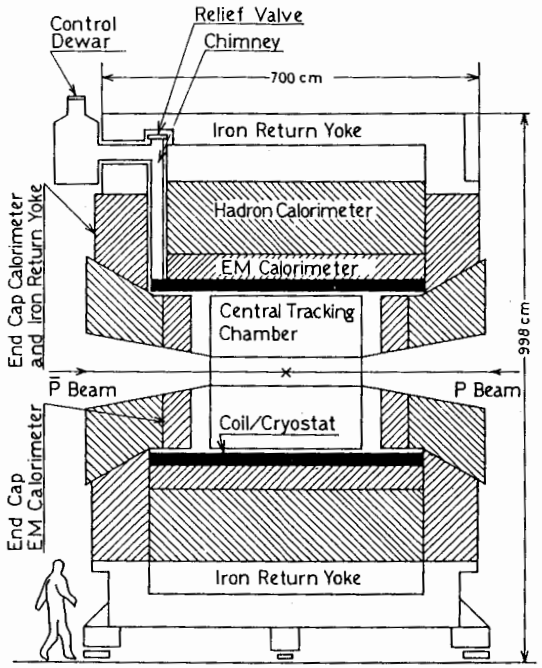

Figure 2.3: Schematic side view of the solenoid system together with the other central detector components.

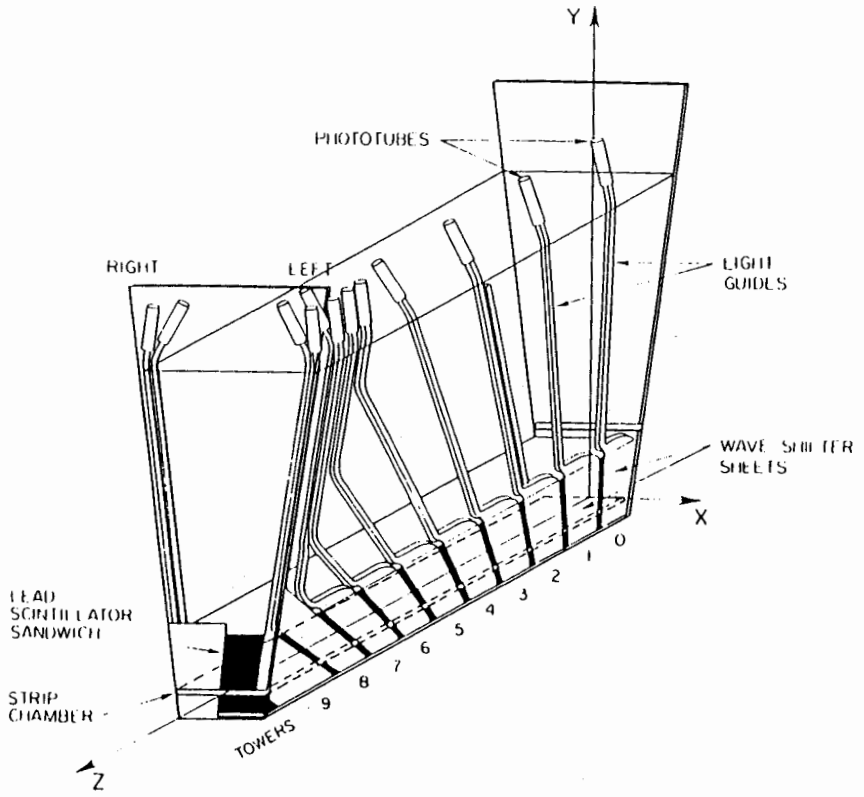

Figure 2.4: Schematic of a wedge module of the CDF central calorimeter showing the local coordinate system as measured by the strip chamber.

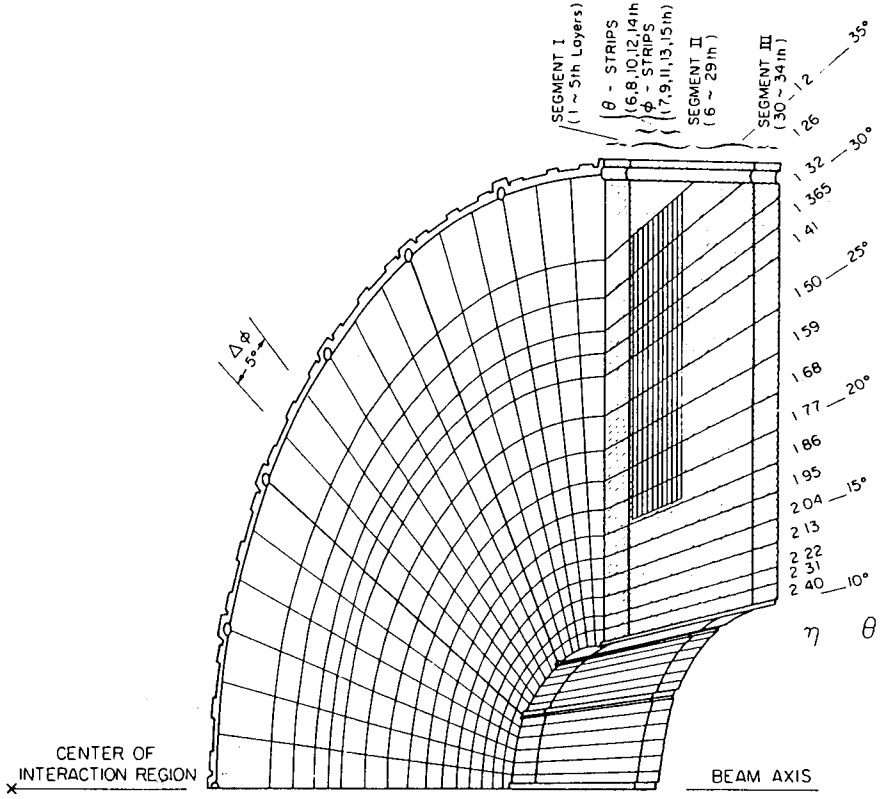

Figure 2.5: Isometric view of a PEM quadrant showing the projective pad tower structure and the longitudinal layers.

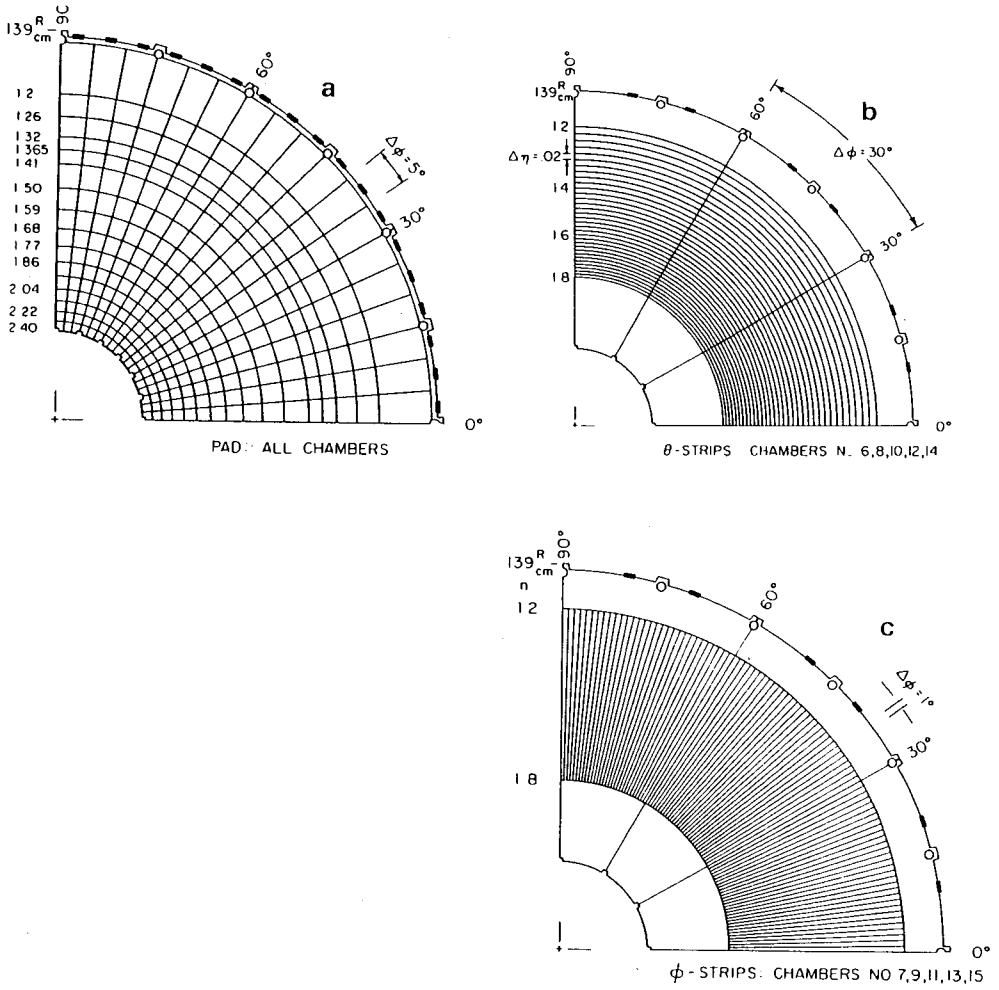

Figure 2.6: Patterns of the outside pickup electrodes of the PEM: a) pads, b) θ strip, and c) ϕ strip.

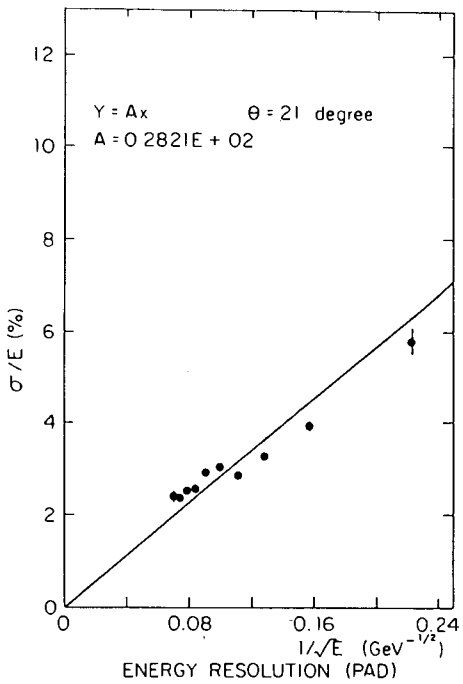

Figure 2.7: Energy resolution measured by the pads of the PEM at 1.8 kV.

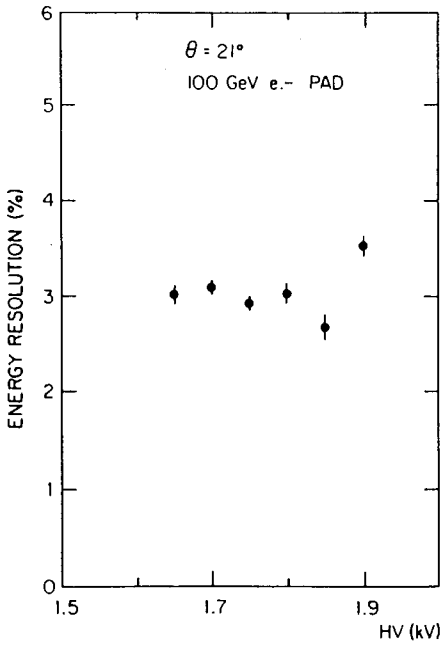

Figure 2.8: Dependence of the energy resolution of PEM on the operation voltages.

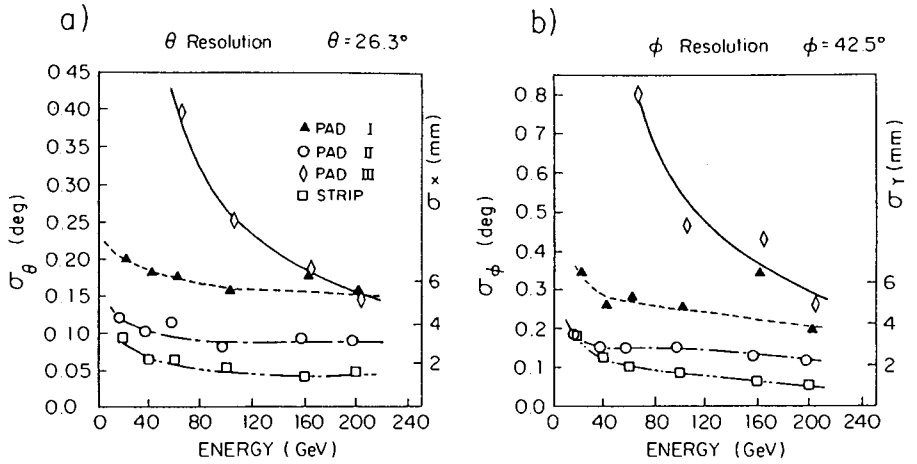

Figure 2.9: Incident energy dependence of the PEM on the position resolution: a) θ direction, and b) ϕ direction.

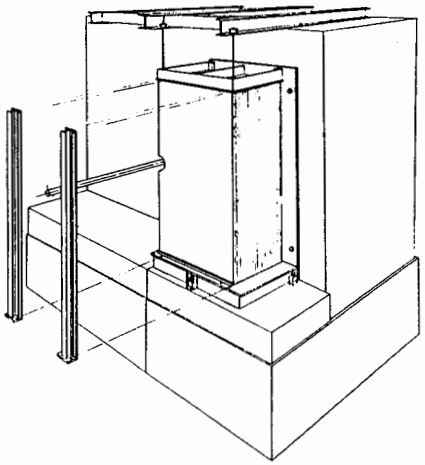

Figure 2.10: One half of one end of the FEM shown mounted on the front face of the FHA steel.

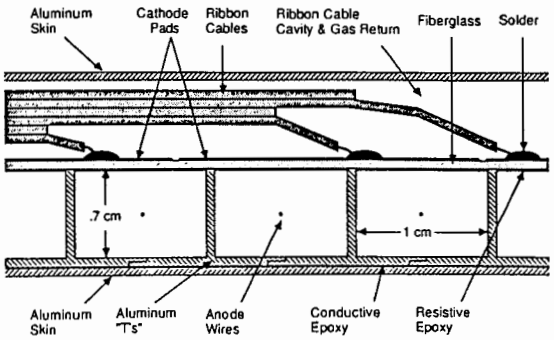

Figure 2.11: Cross section of a typical FEM chamber with appropriate dimensions indicated.

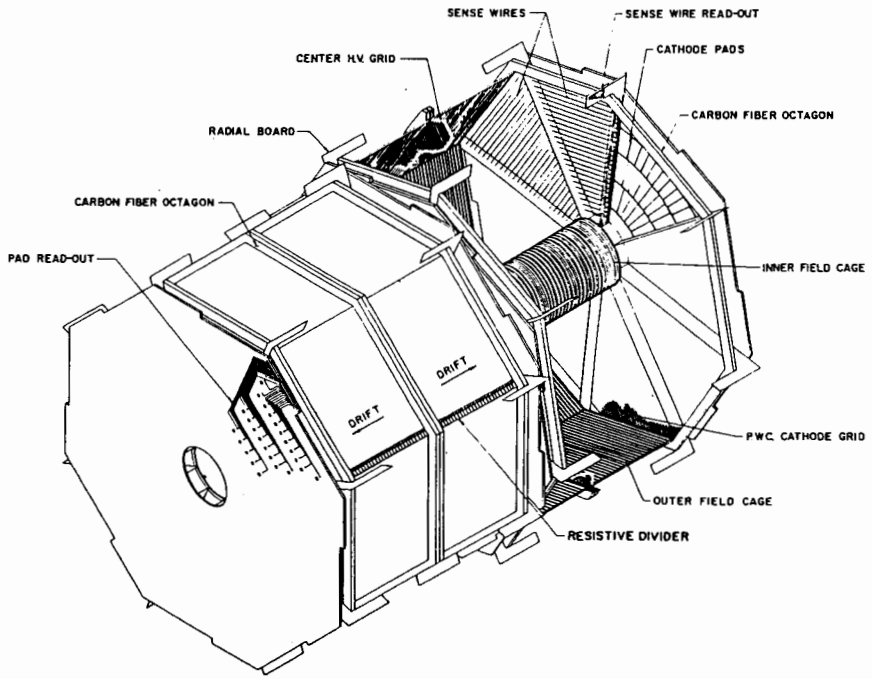

Figure 2.12: An isometric view of two VTPC modules. They are rotated in ϕ by 11.3° with respect to each other.

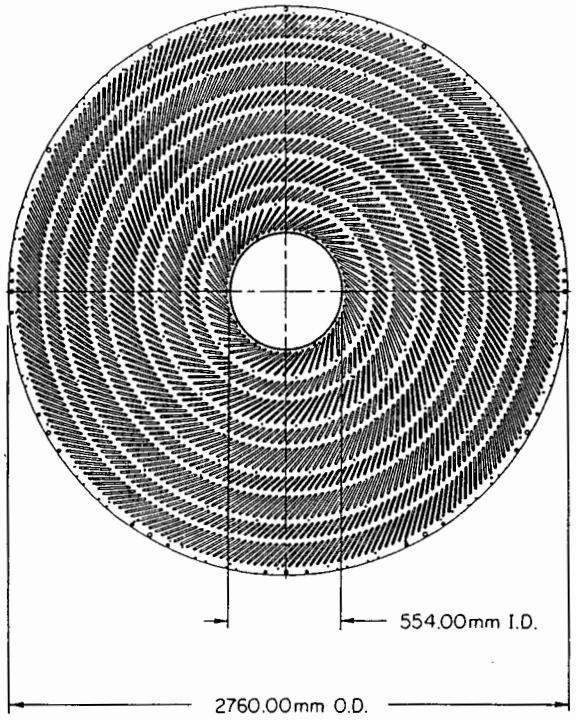

Figure 2.13: End view of the CTC showing the location of the slots in the aluminum endplates.

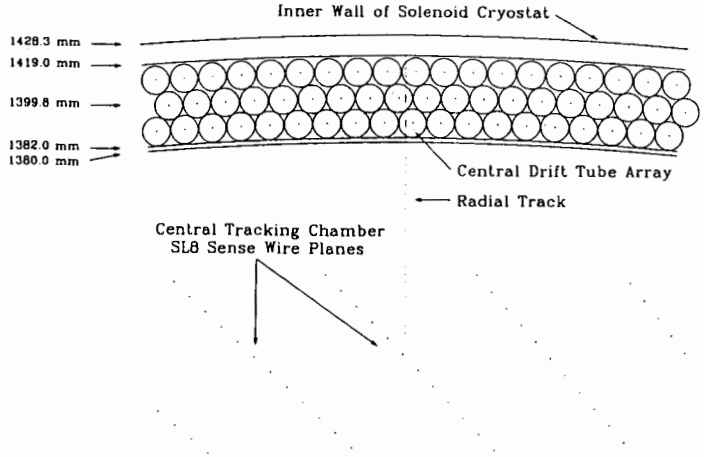

Figure 2.14: Tube array geometry of the CDT.

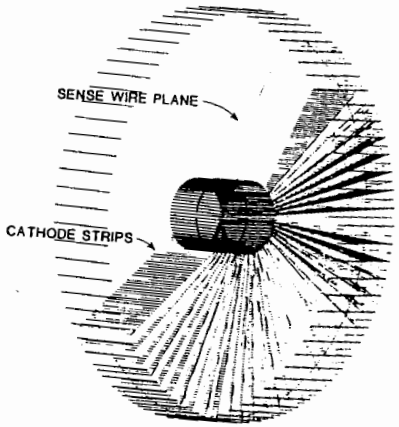

Figure 2.15: An isometric view of the FTC configuration.

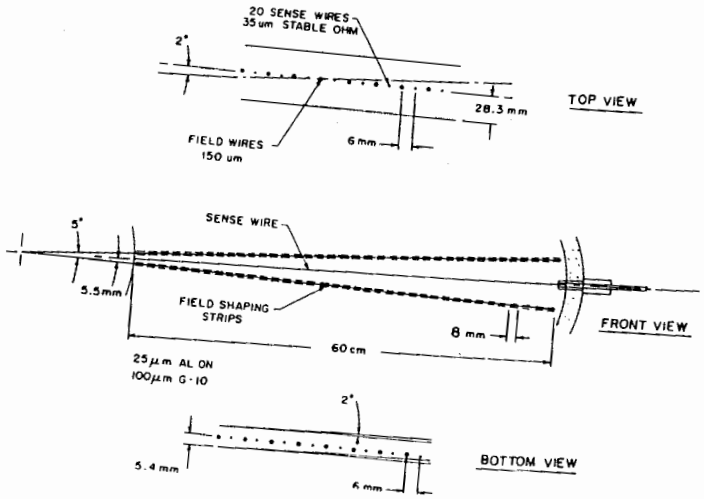

Figure 2.16: A beam view of a radial cell of the FTC.

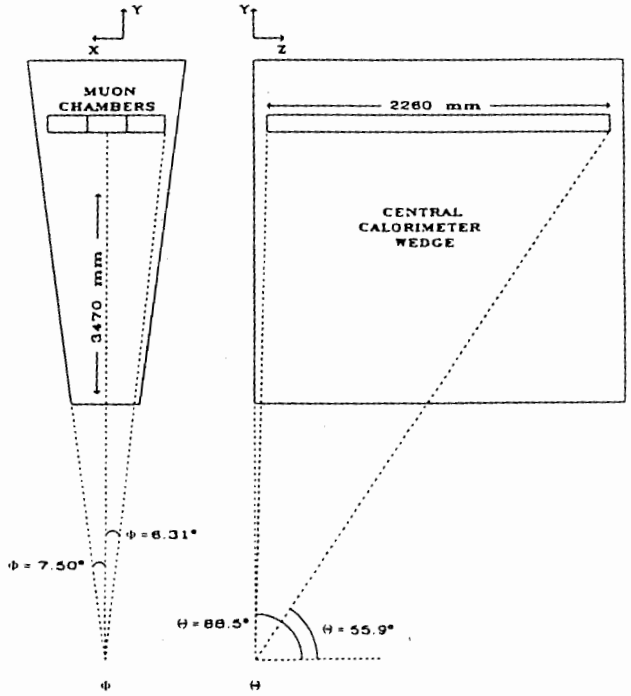

Figure 2.17: Location of the CMU with in the central calorimeter.

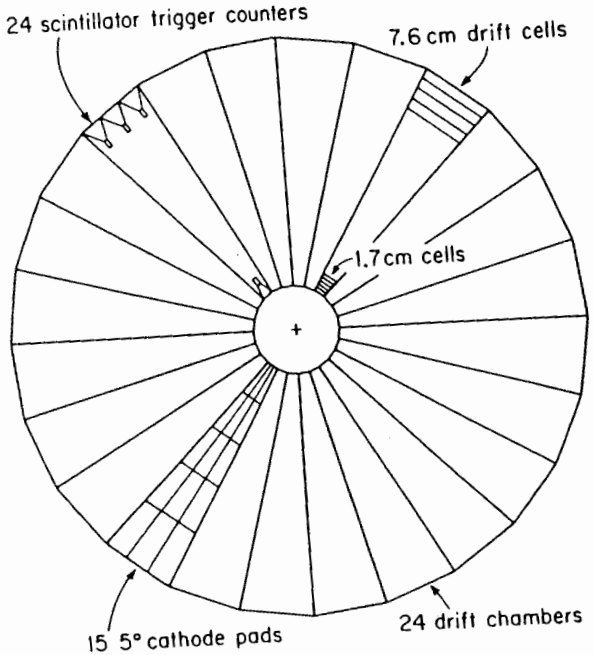

Figure 2.18: Elements of the FMU detector plane.

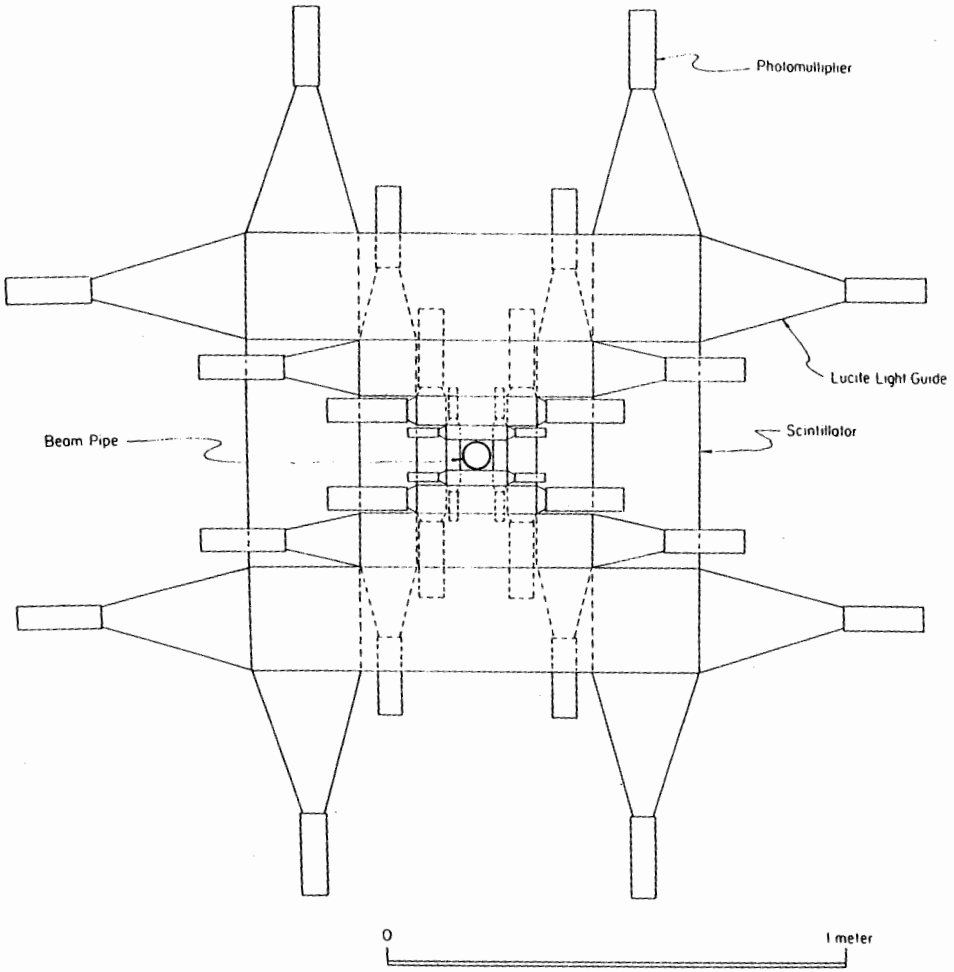

Figure 2.19: A beam's-eye view of one of the BBC planes.

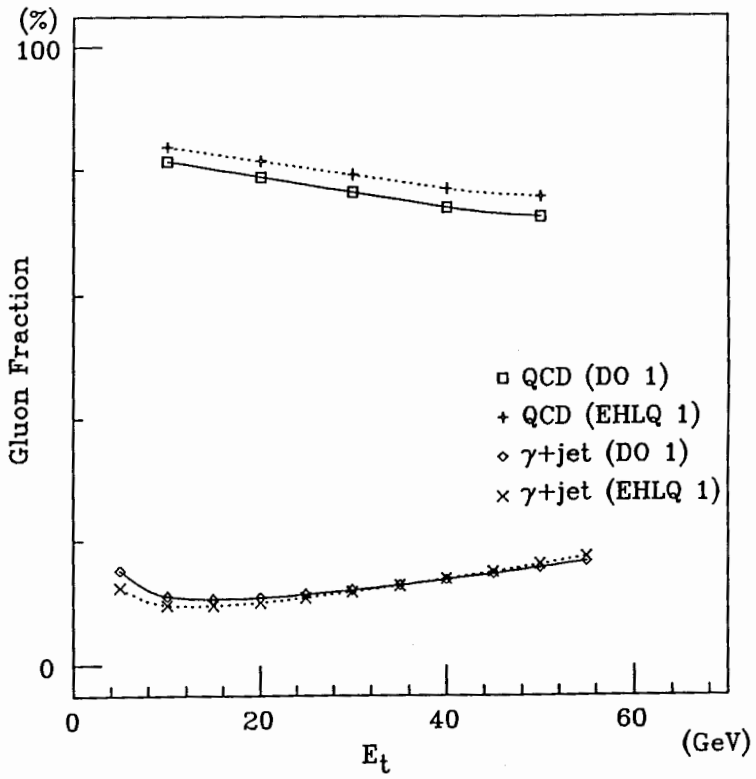

Figure 3.1: The fraction of the final state gluon in the sample (QCD dijet and γ+jet), as a function of jet transverse energy E_t. The data are theoretical prediction. The calculation is of the lowest order QCD only for dijet cross section, but it includes the higher order QCD contributions to the cross section of γ+jet. The used structure functions are EHLQ and Duke-Owens with Λ = 200 MeV.

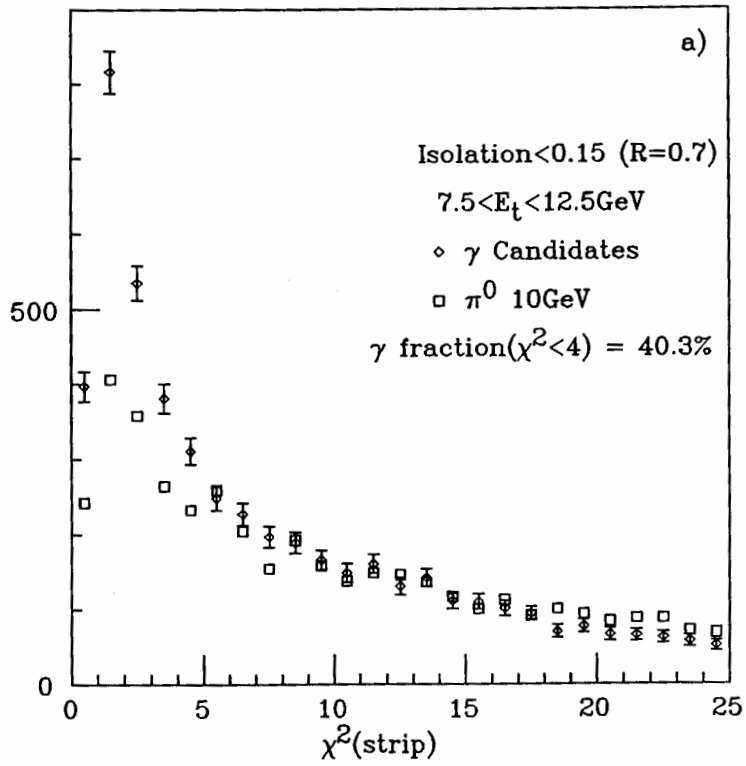

Figure 3.2: Distributions of average χ^2 for central strip chamber profiles(wire/strip) for isolated photon candidates. The simulated π^0 background is plotted with a scale chosen so that the π^0 data is equal to the high χ^2 ($4 < \chi^2 < 25$) tail of the distribution for photon candidates. The data are shown for different E_t ranges: a) 7.5 – 12.5 GeV, b) 12.5 – 17.5 GeV, c) 17.5 – 22.5 GeV, and d) 22.5 – 27.5 GeV.

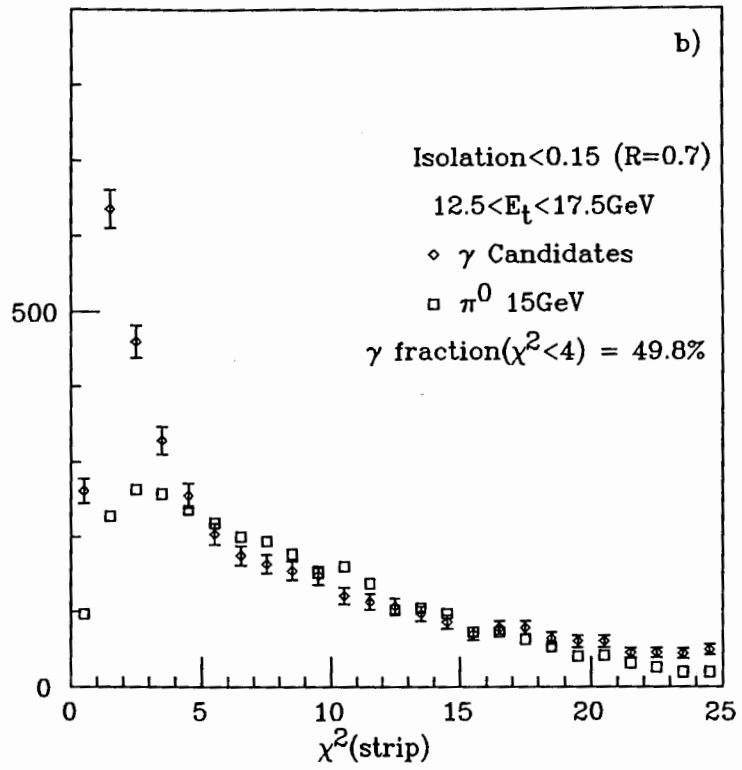

Figure 3.2 b

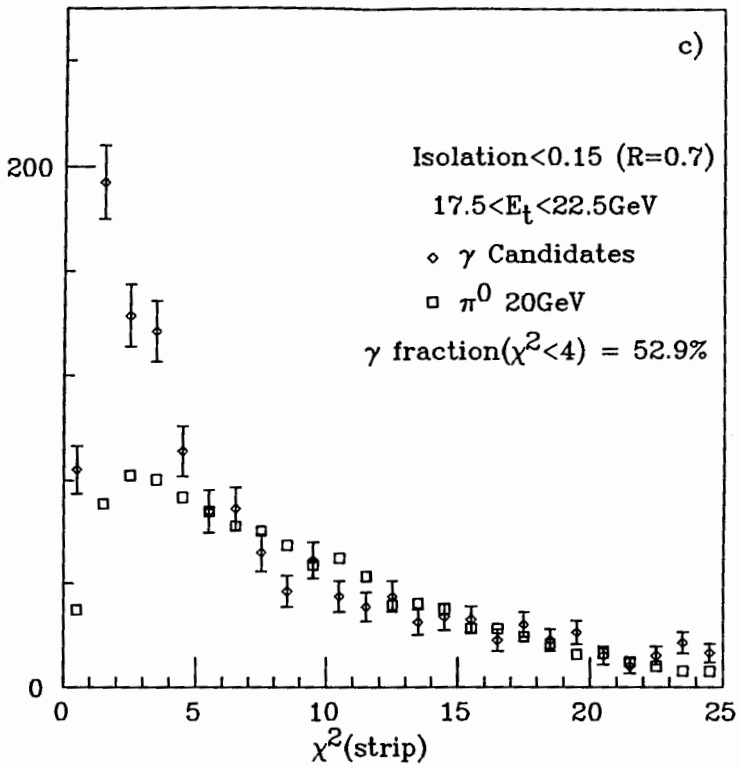

Figure 3.2 c

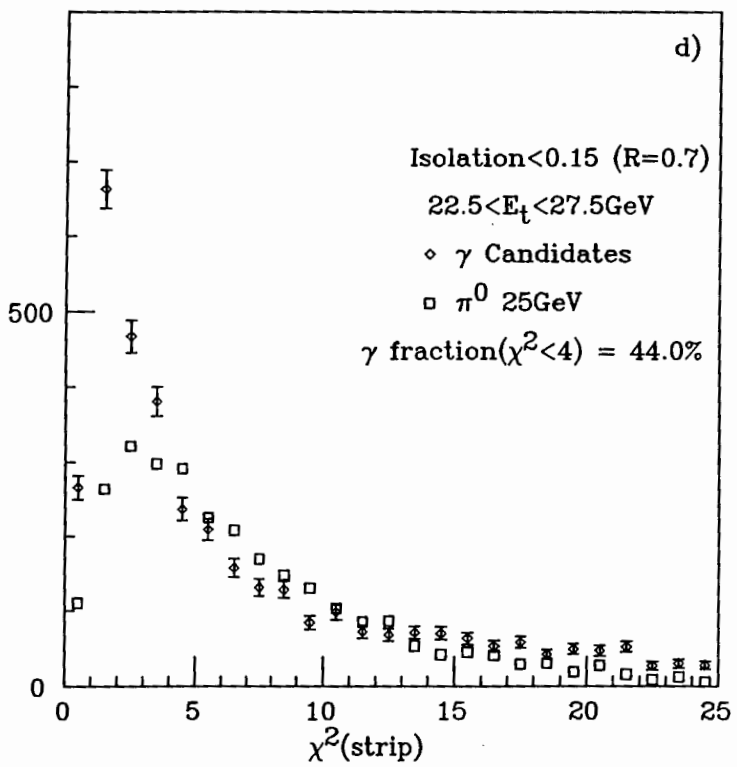

Figure 3.2 d

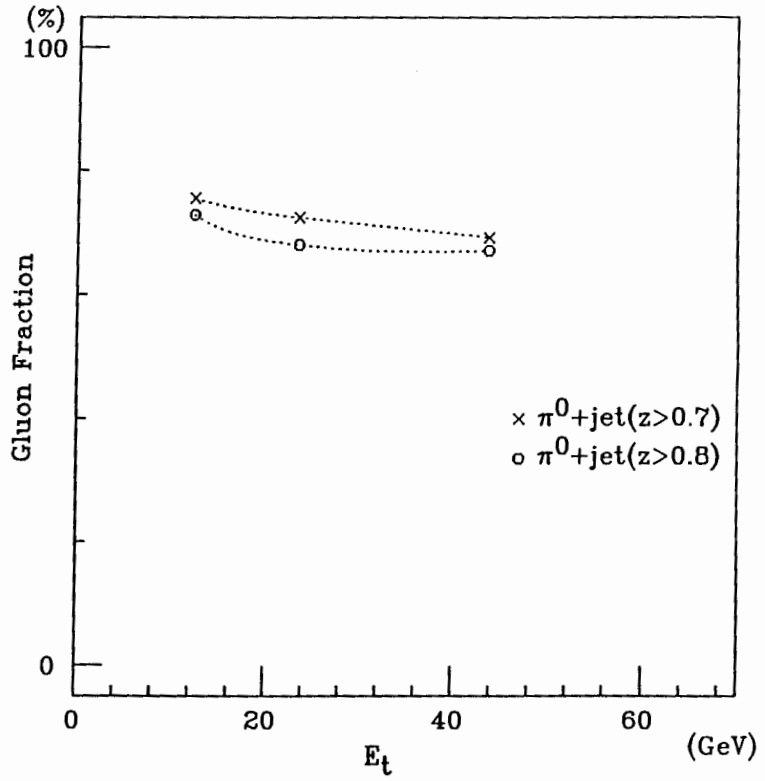

Figure 3.3: The fraction of the final state gluon in the sample where one of two final partons fragments into π^0 with the momentum fraction $z > 0.7$ (crosses), and into π^0 with $z > 0.8$ (open circles). The data are Monte Calro model prediction with Herwig generator.

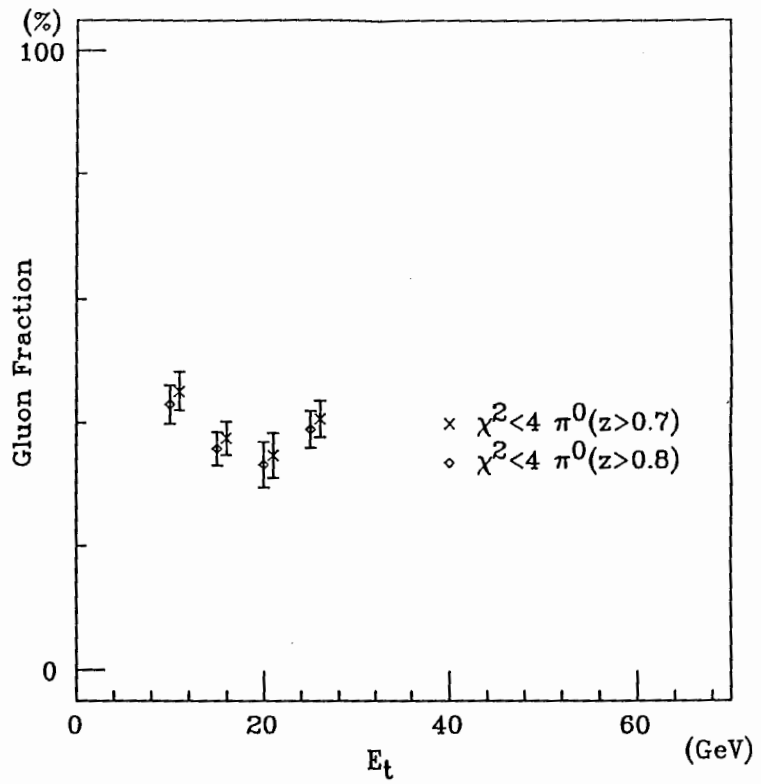

Figure 3.4: The expected gluon fraction for the photon candidates as a function of the jet E_t. The points shows the result of the calculation given in eq. 3.4 and their statistical errors.

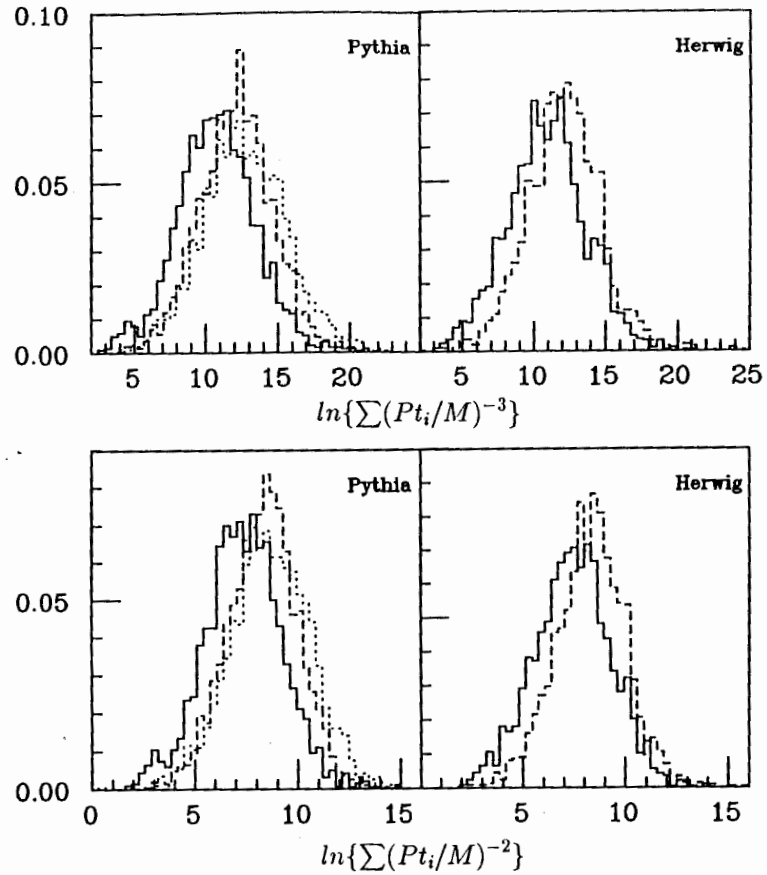

Figure 4.1: Distributions of mechanical transverse moments. In this and subsequent figures, solid and dot-dashed histograms correspond to quark and gluon reference jets with $30 < E_t < 40$ GeV respectively. Dotted histograms are from 1987 dijet events

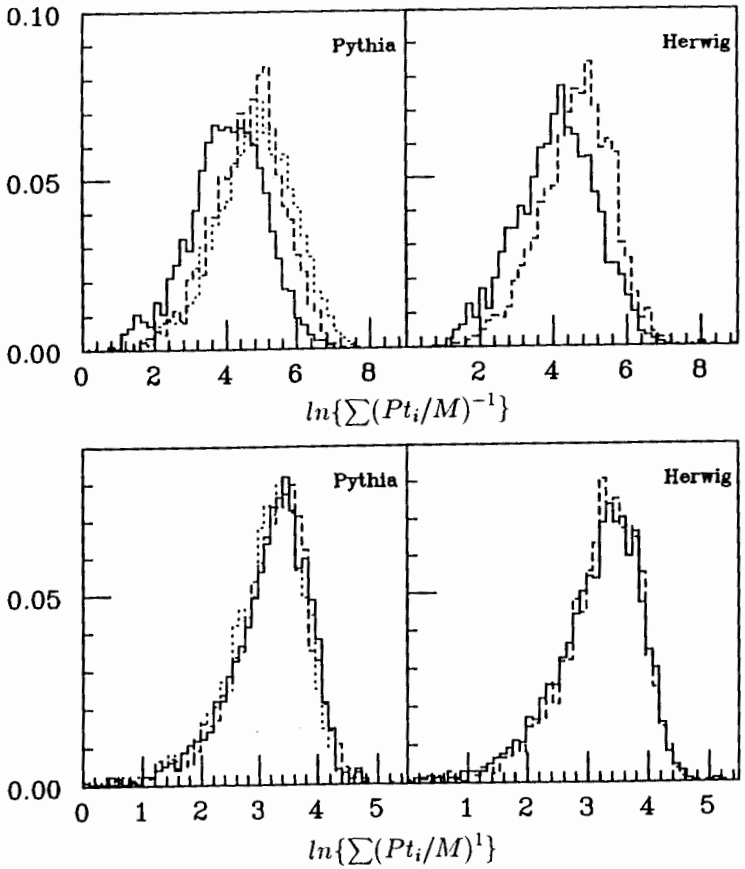

Figure 4.1 ii

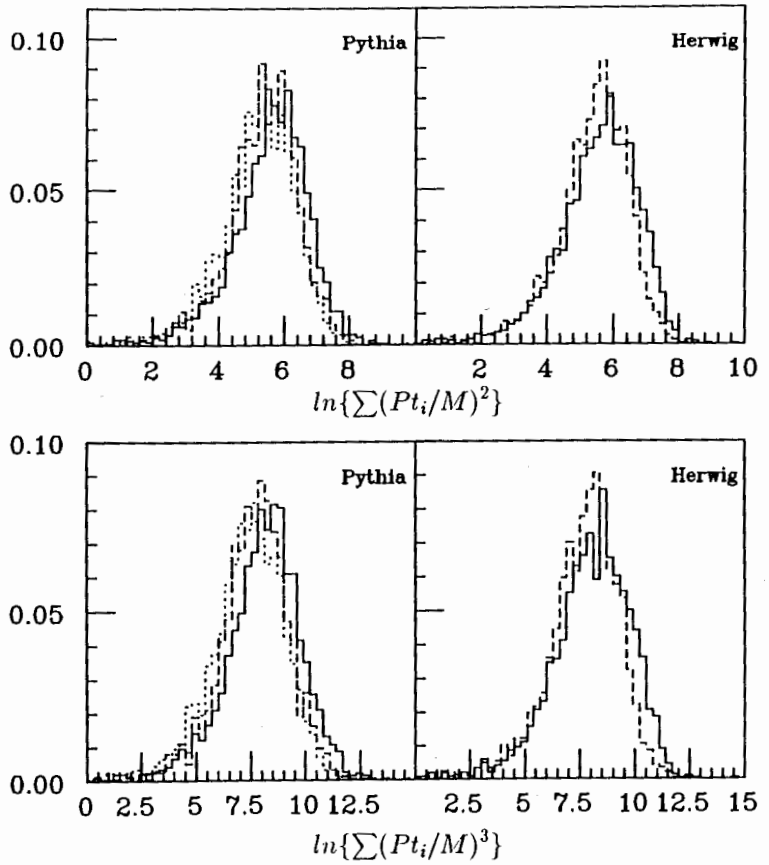

Figure 4.1 iii

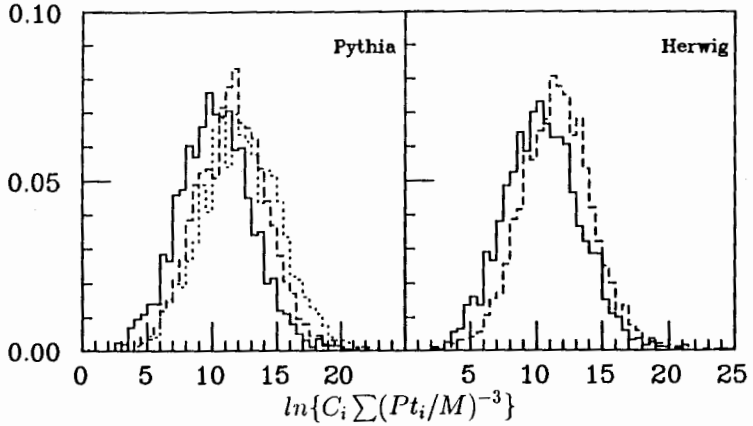

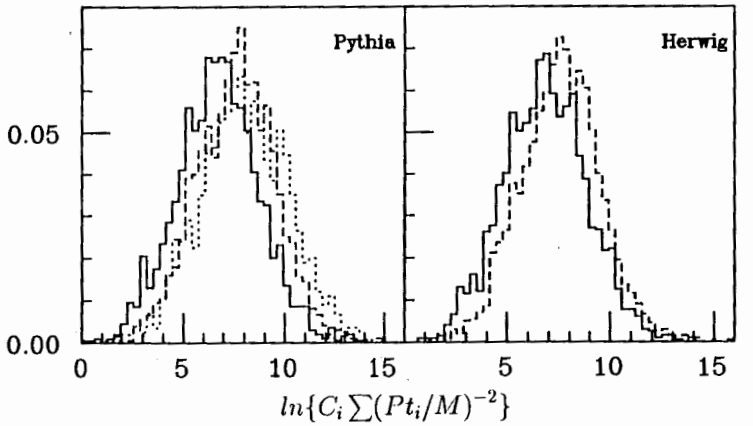

Figure 4.2: Distributions of electric transverse moments.

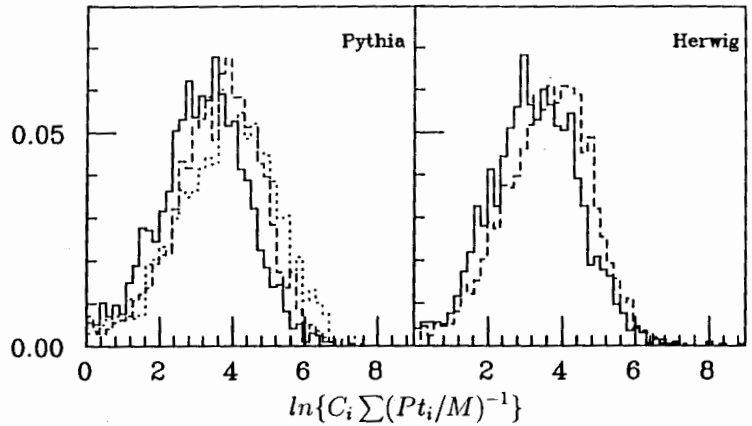

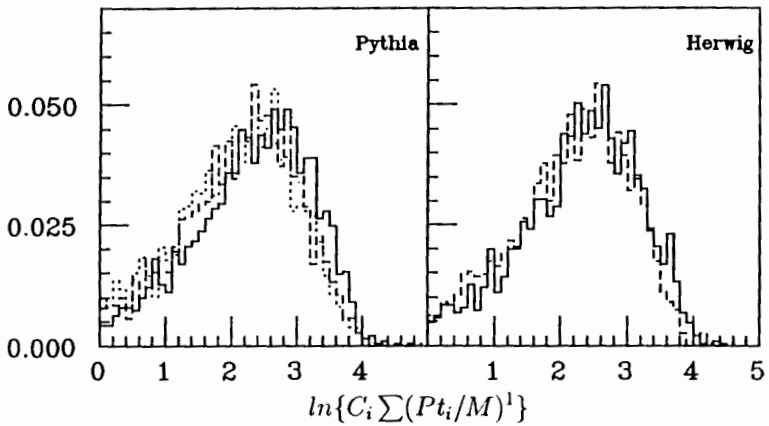

Figure 4.2 ii

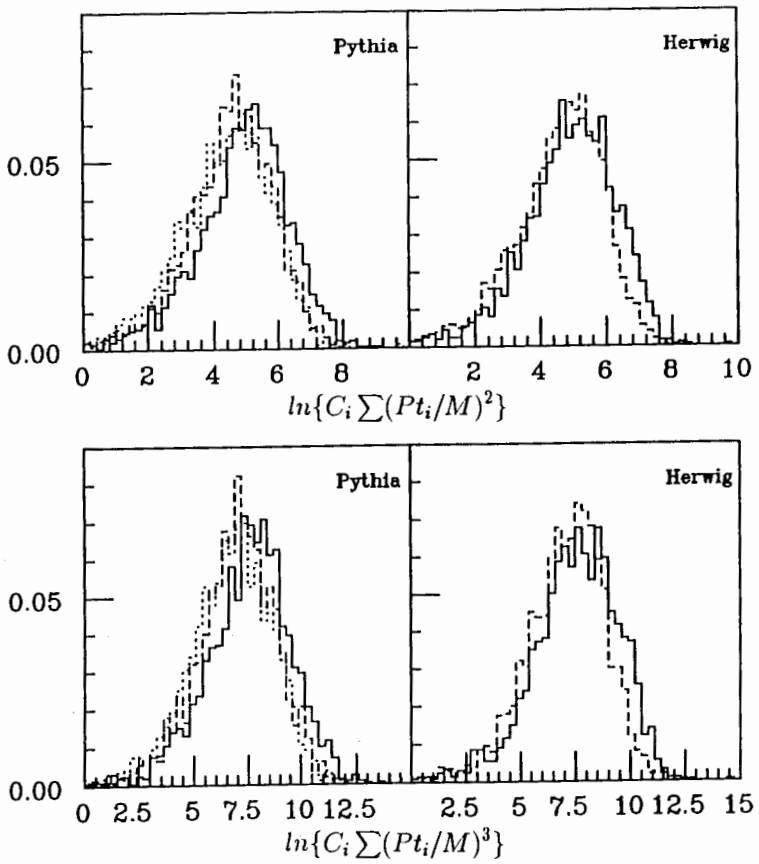

Figure 4.2 iii

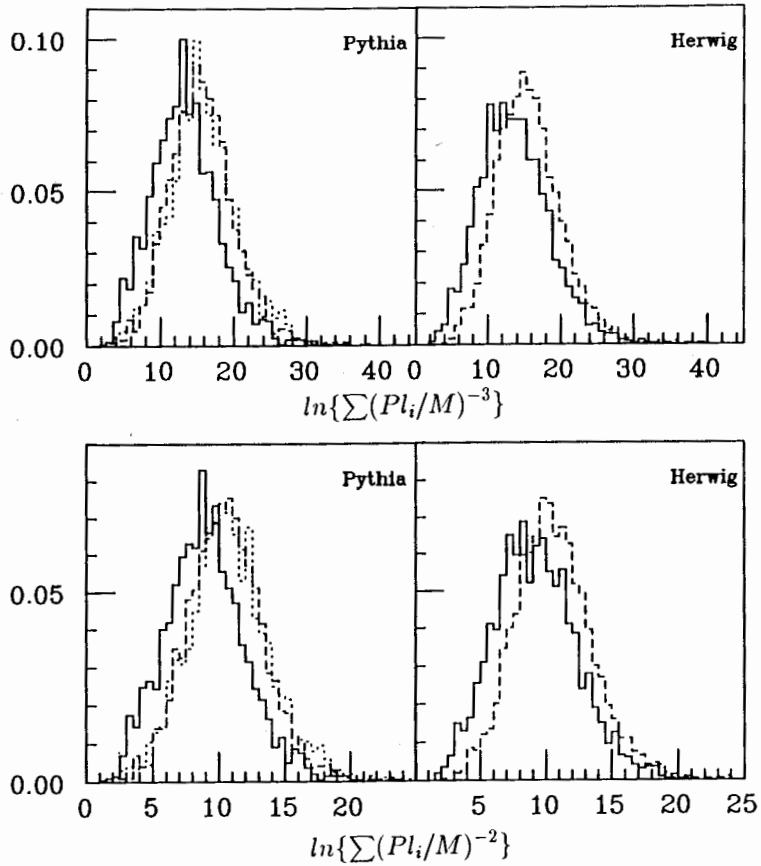

Figure 4.3: Distributions of mechanical longitudinal moments.

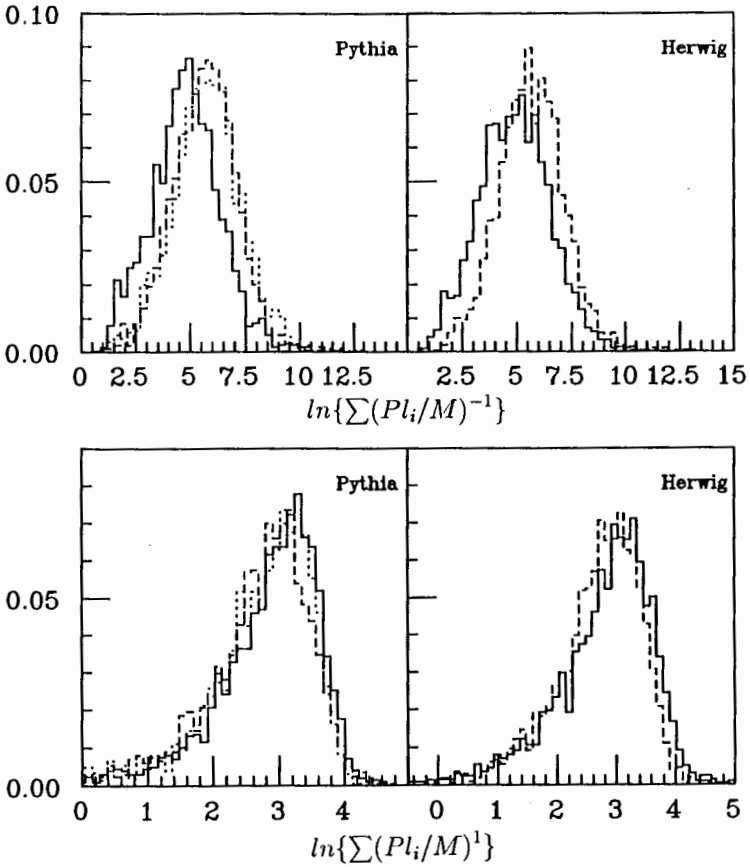

Figure 4.3 ii

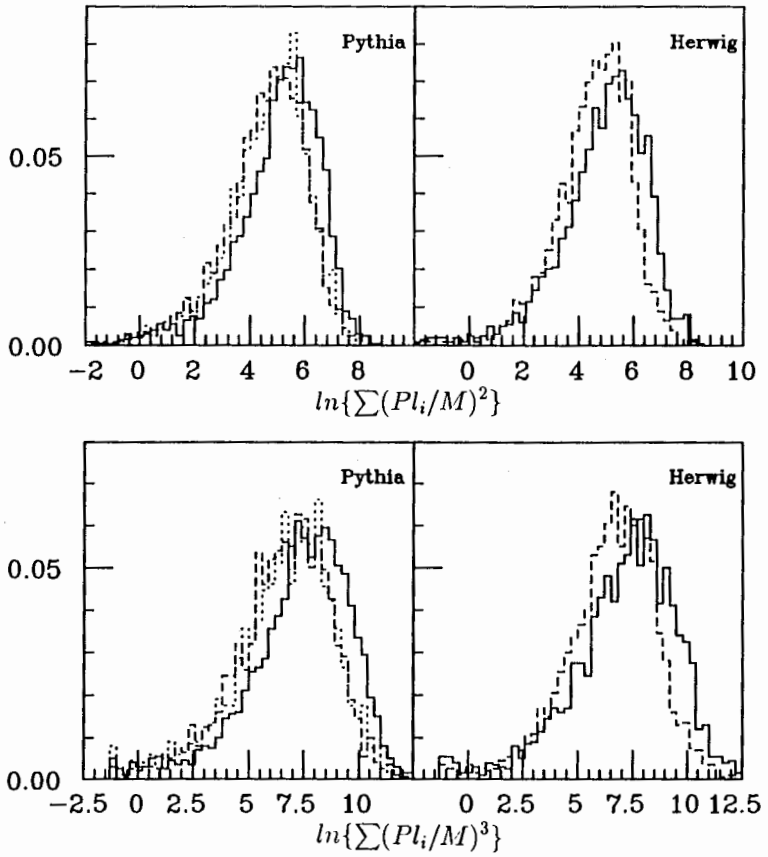

Figure 4.3 iii

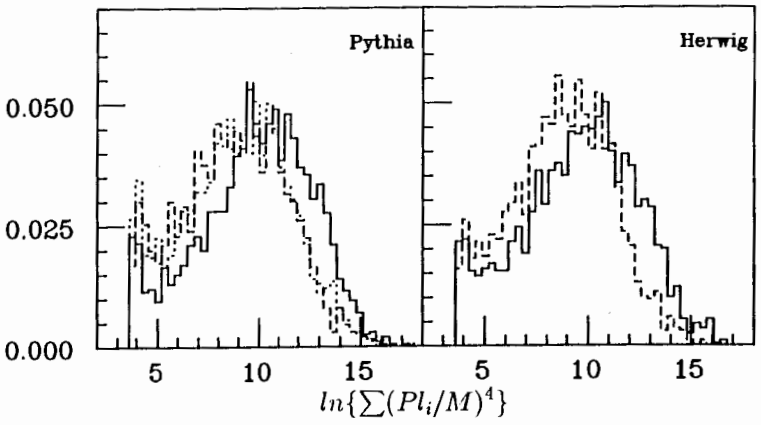

Figure 4.3 vi

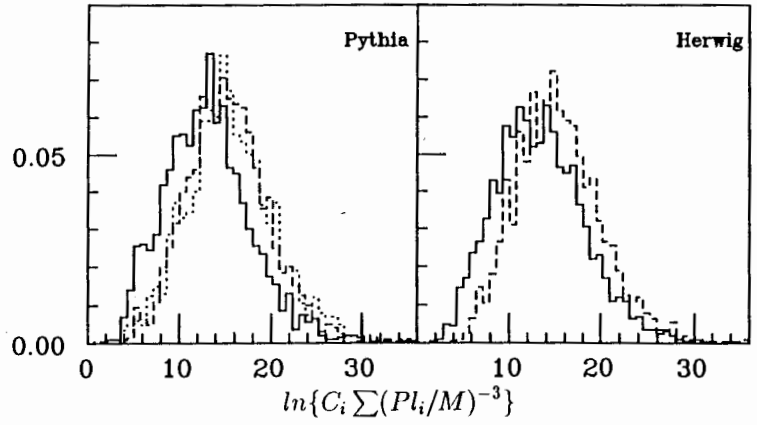

Figure 4.4: Distributions of electric longitudinal moments.

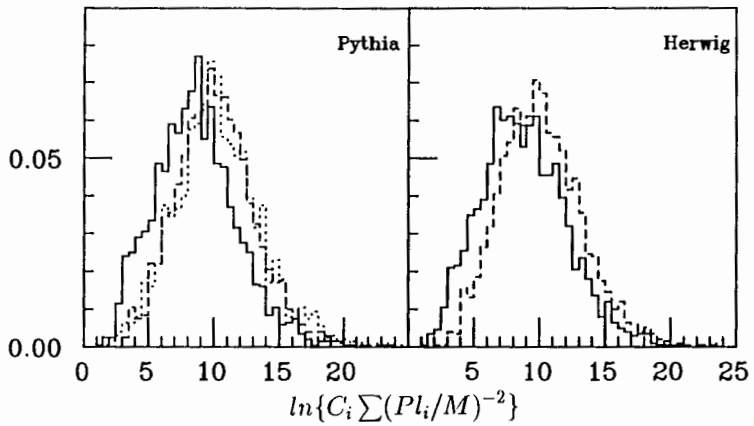

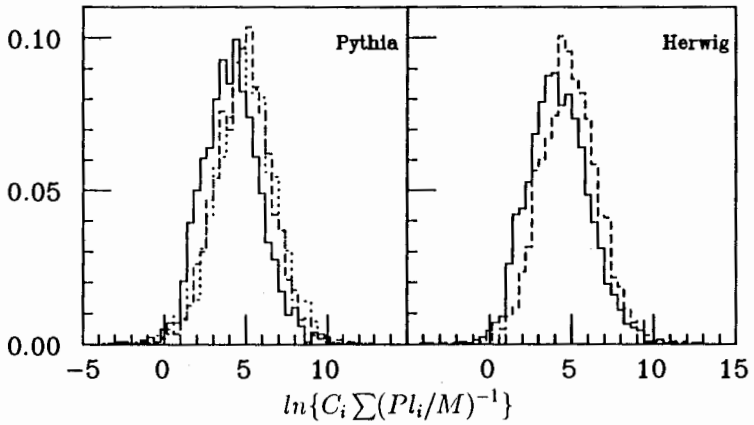

Figure 4.4 ii

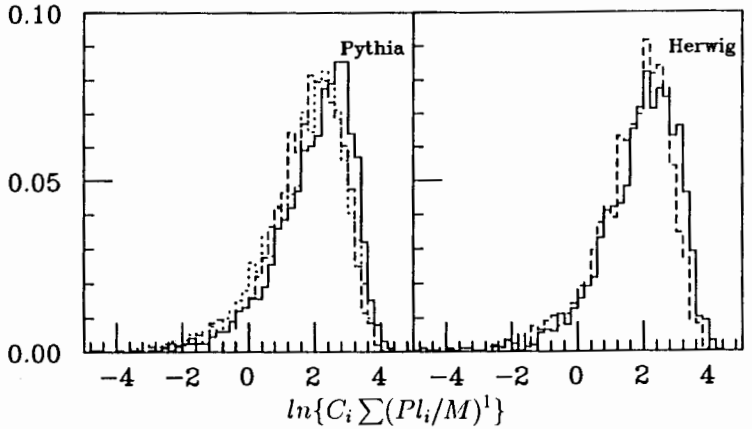

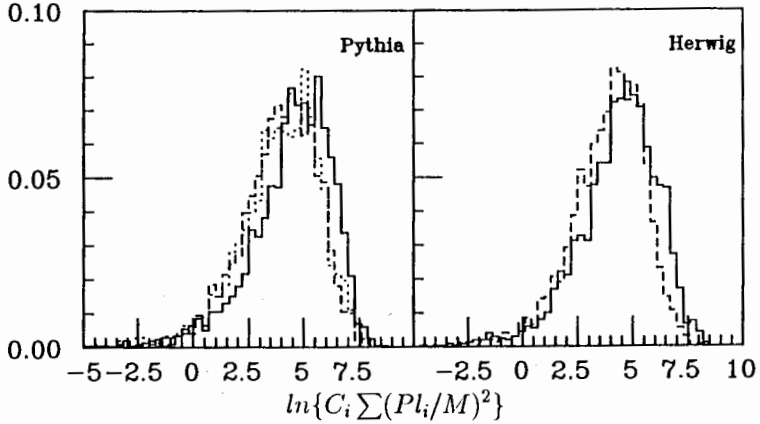

Figure 4.4 iii

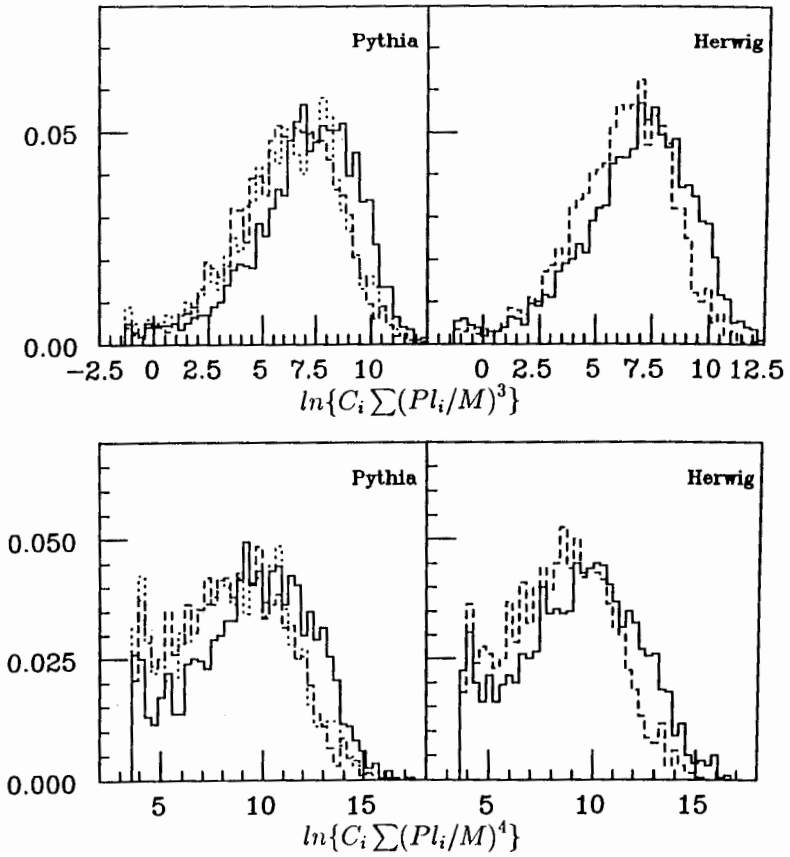

Figure 4.4 vi

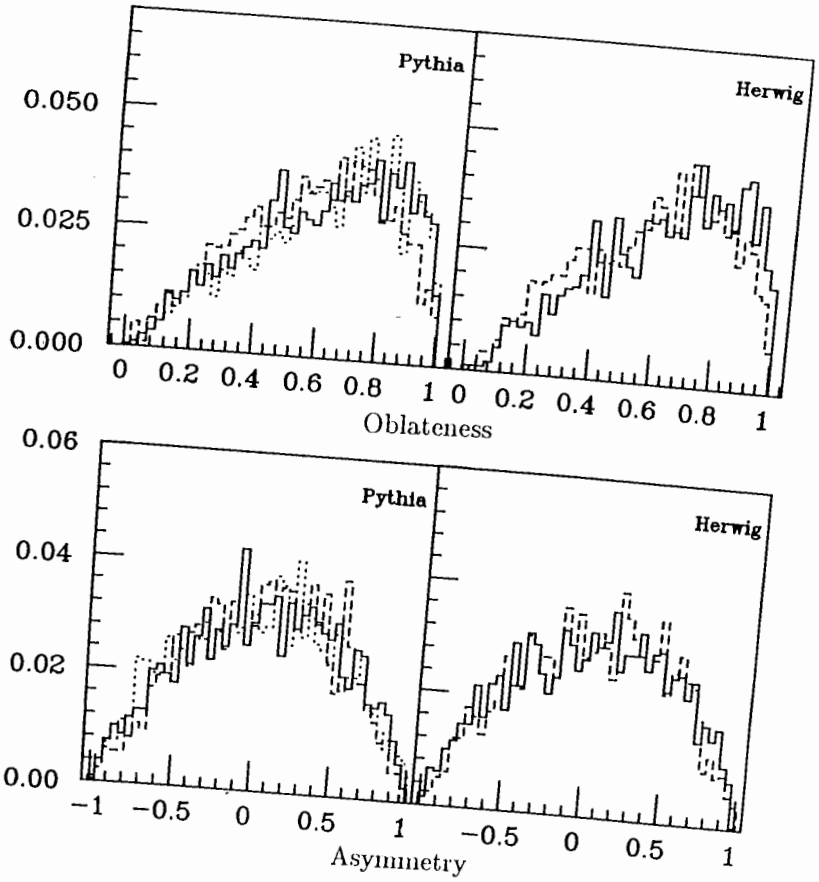

Figure 4.5: Distributions of jet-fragments-asymmetry and oblateness of the jet.

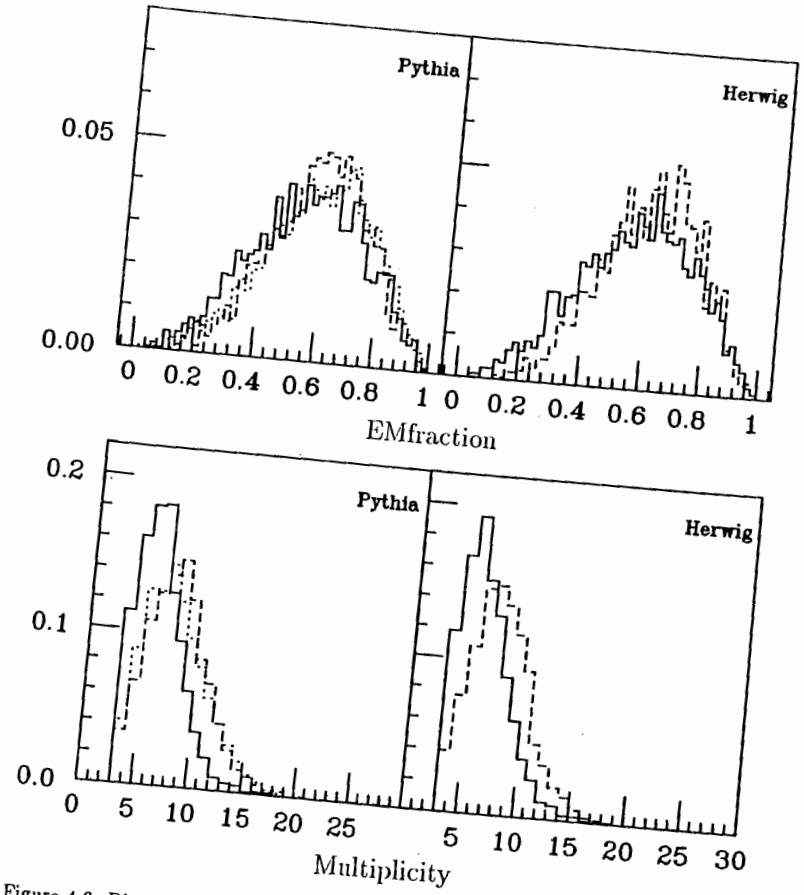

Figure 4.6: Distributions of jet charged multiplicity and EM energy fraction of the jet.

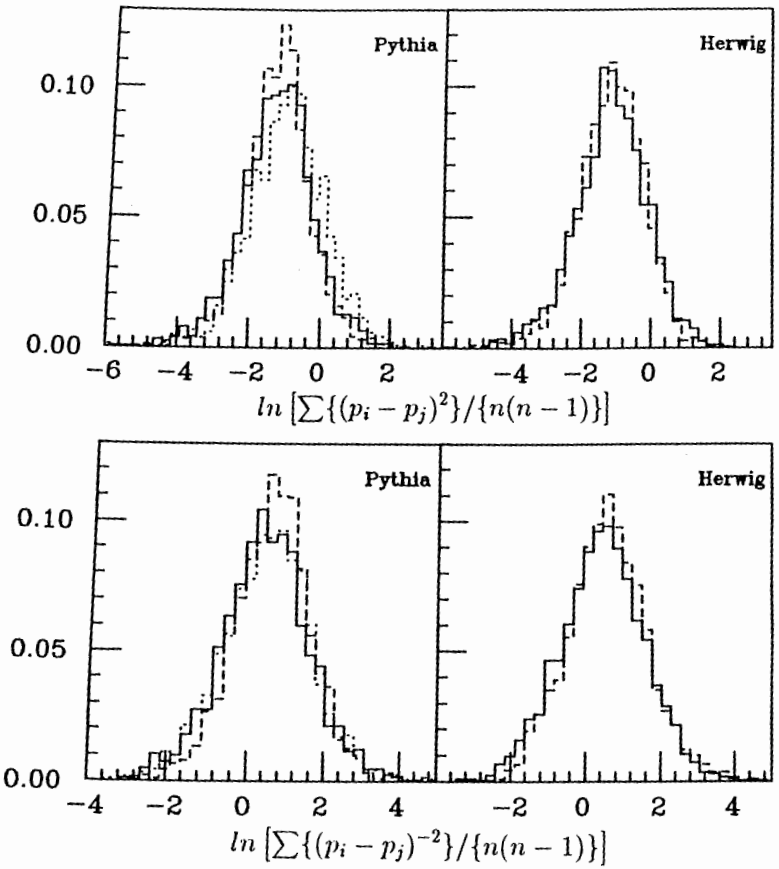

Figure 4.7: Distributions of the correlation variables given in eq. 4.5.

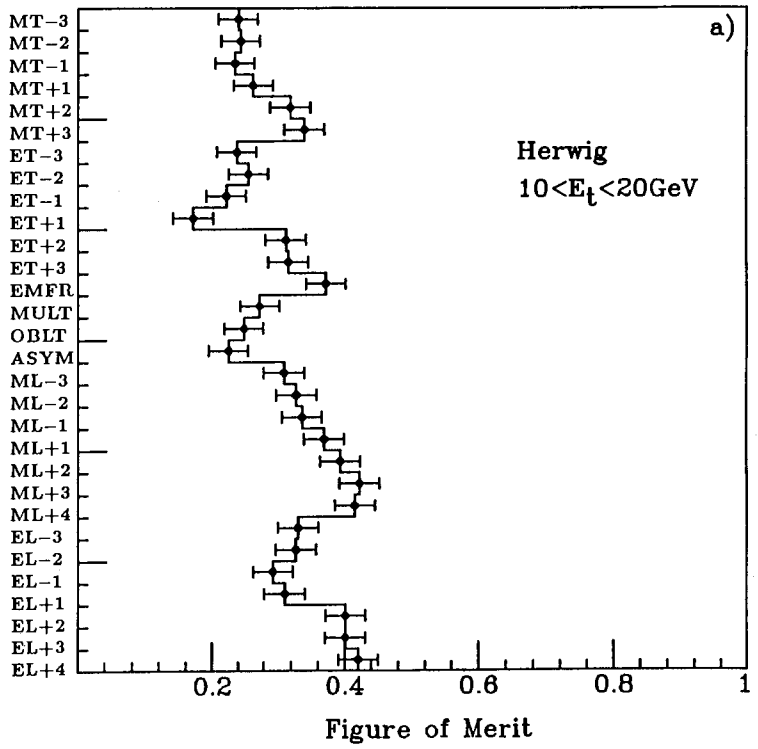

Figure 4.8: Figures of merit of 30 variables for two Monte Calro's: Herwig and Pythia. The letters, MT, ET, ML and EL followed by positive/negative numbers (the power of moment) mean "Mechanical Transverse moment", "Electric Transverse moment", "Mechanical Longitudinal moment" and "Electric Longitudinal moment", respectively (see Table 4.1). The other four letters, EMFR, MULT, OBLT and ASYM refer to the electro magnetic fraction of a jet, charged multiplicity within a jet, oblateness of jet and asymmetry of jet fragments, respectively. The data points were shown for the sample of simulated jets in some transverse energy E_t range, with their statistical errors

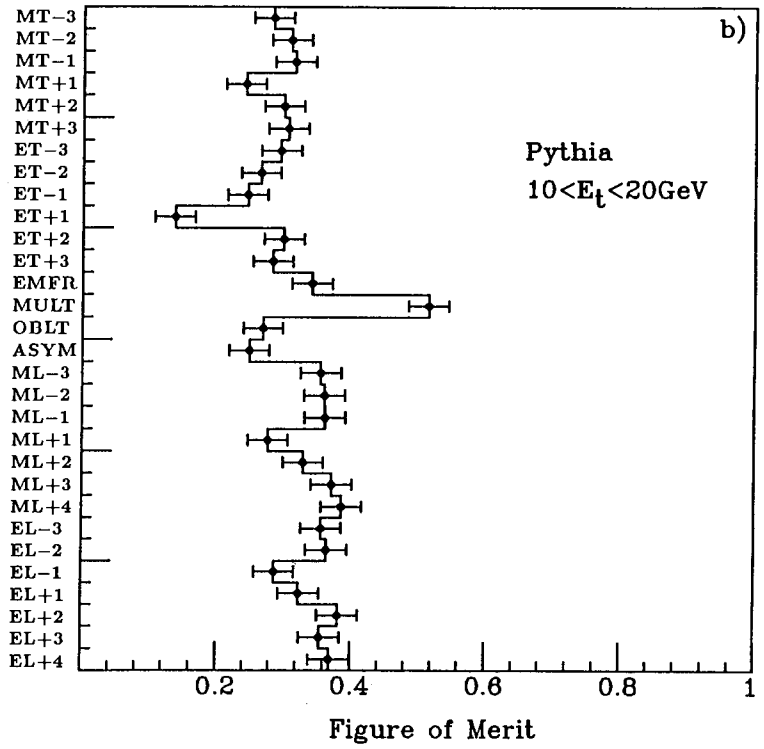

Figure 4.8 b

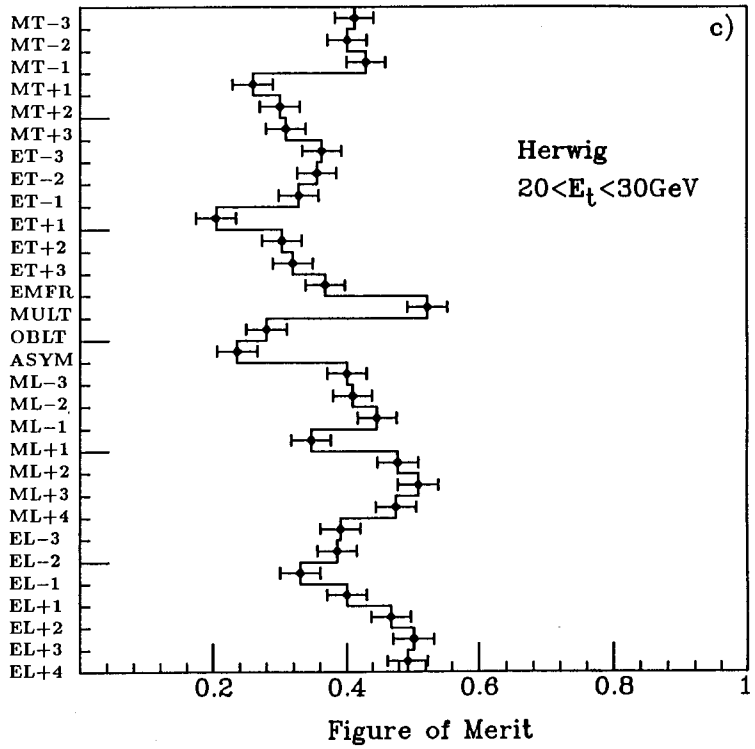

Figure 4.8 c

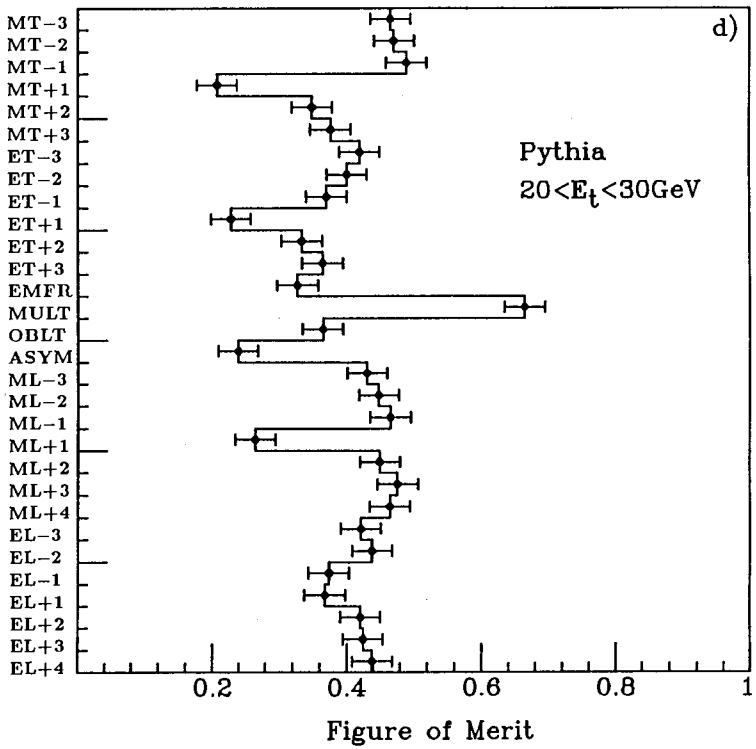

Figure 4.8 d

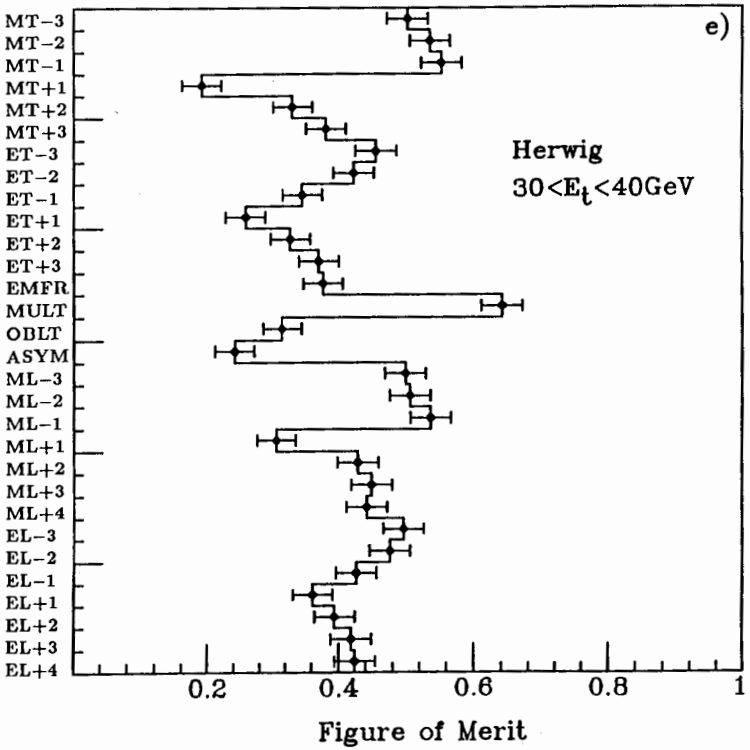

Figure 4.8 e

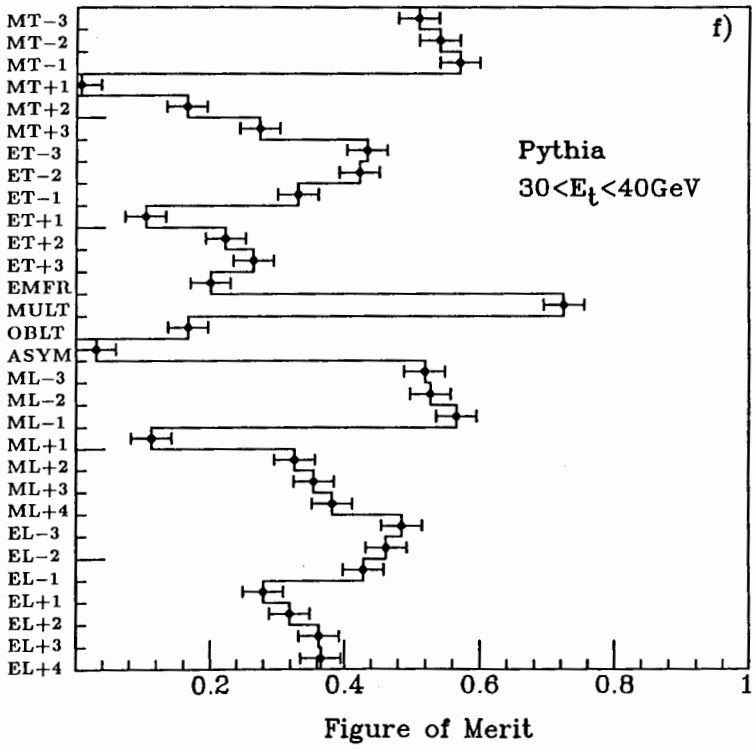

Figure 4.8 f

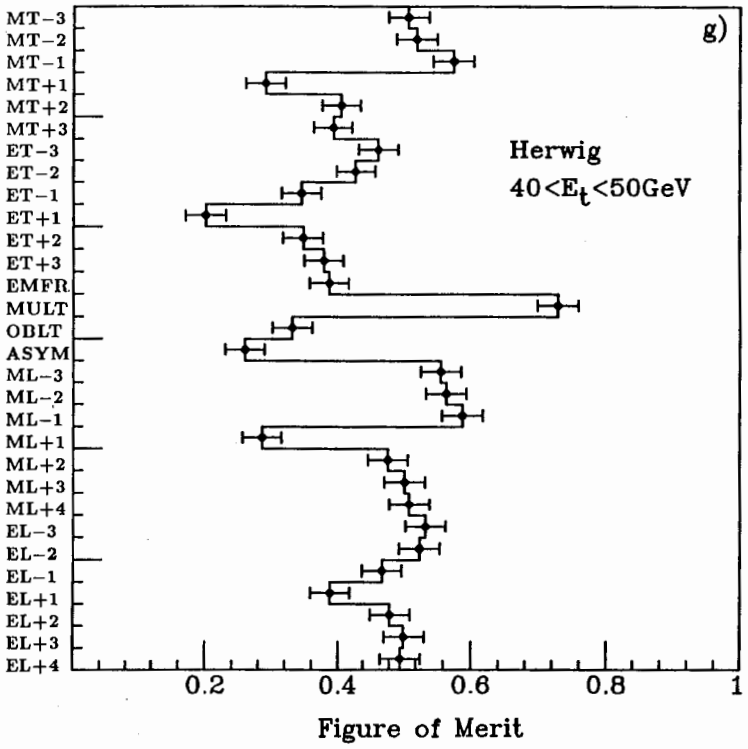

Figure 4.8 g

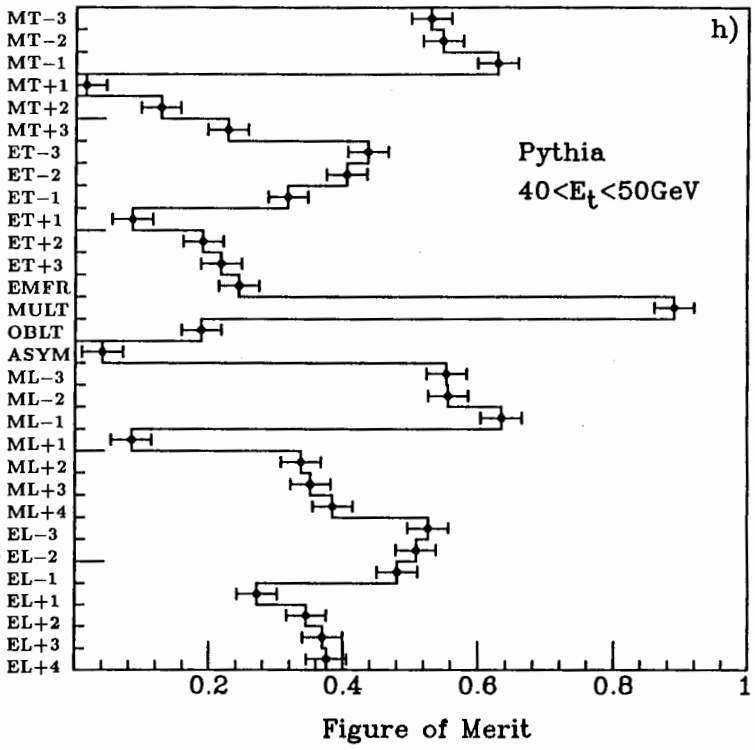

Figure 4.8 h

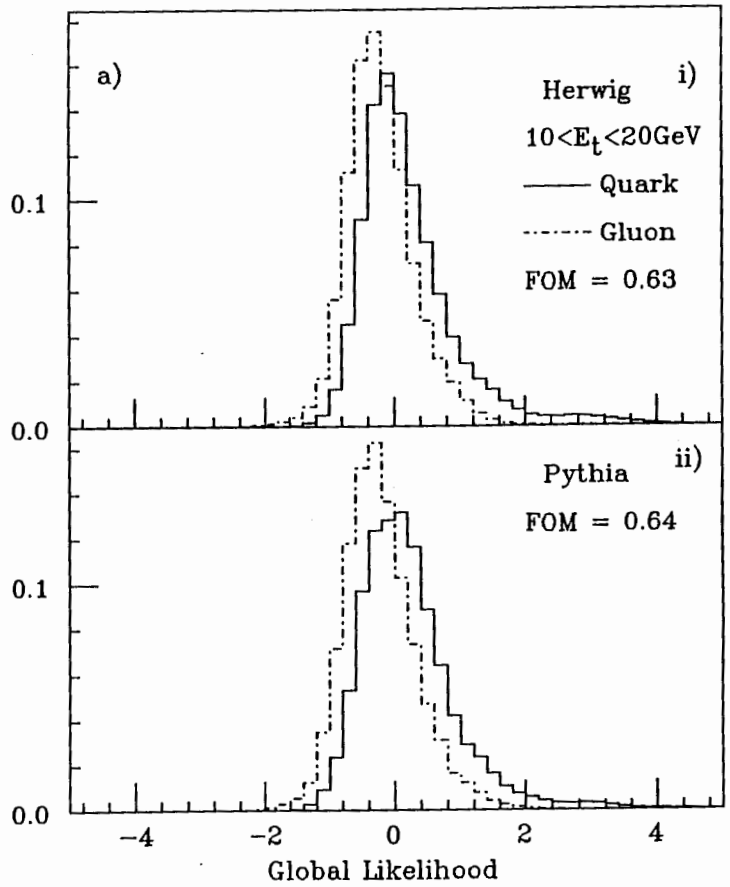

Figure 4.9: Distribution of "global likelihood" defined by eqs. 4.7 and 4.8 for the samples generated with i) Herwig and ii) Pythia in $\bar{p}p$ collisions at $\sqrt{s}$=1.8 TeV. The both generated quark and gluon jets were processed through the detector simulation, and then reconstructed with a cone algorithm. The E_t range of the jets is a) 10–20, b) 20–30, c) 30–40 or d) 40–50 GeV.

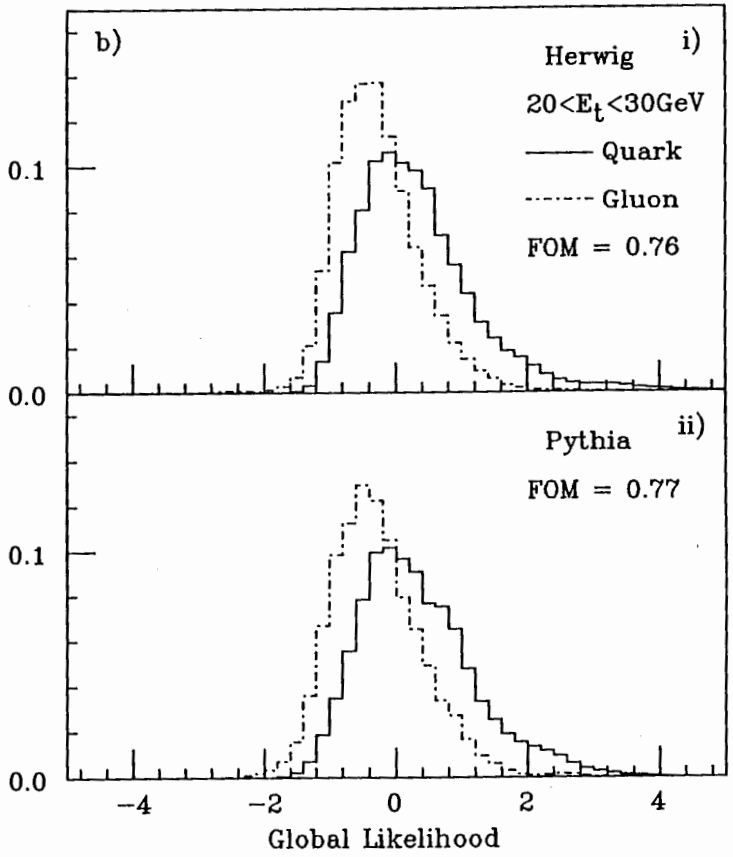

Figure 4.9 b

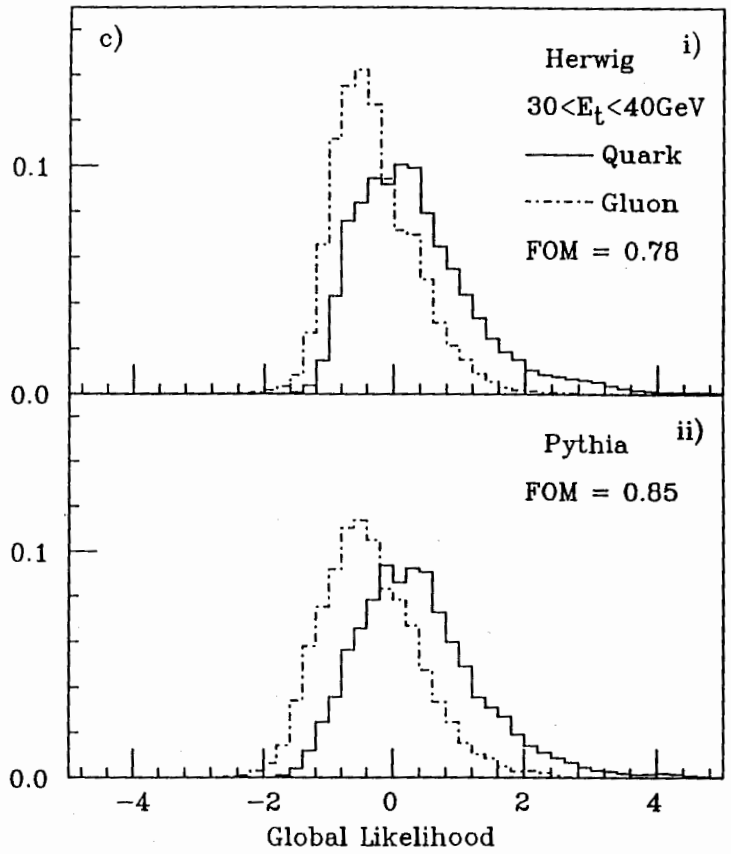

Figure 4.9 c

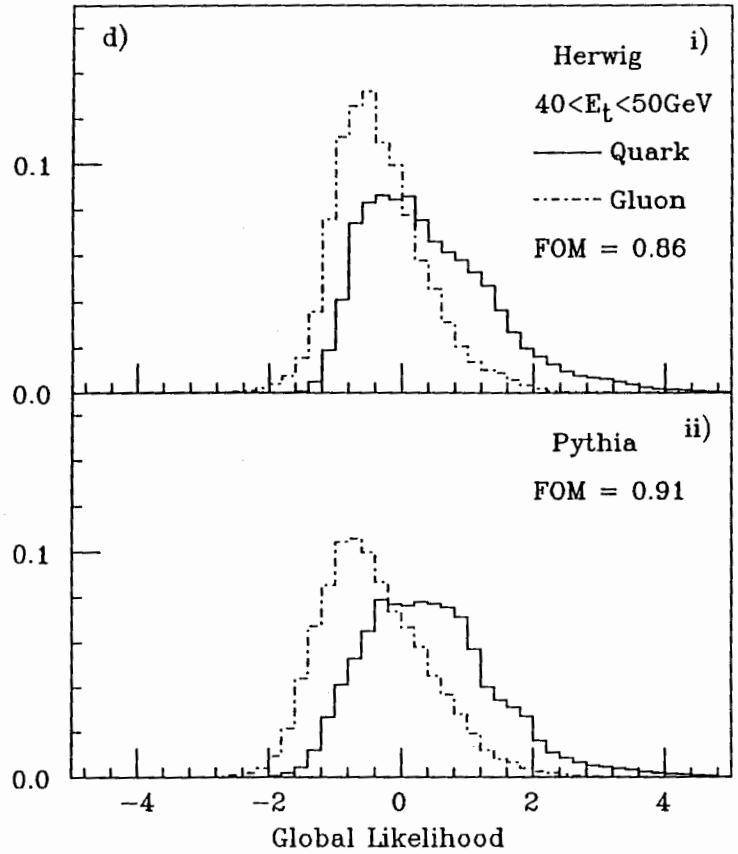

Figure 4.9 d

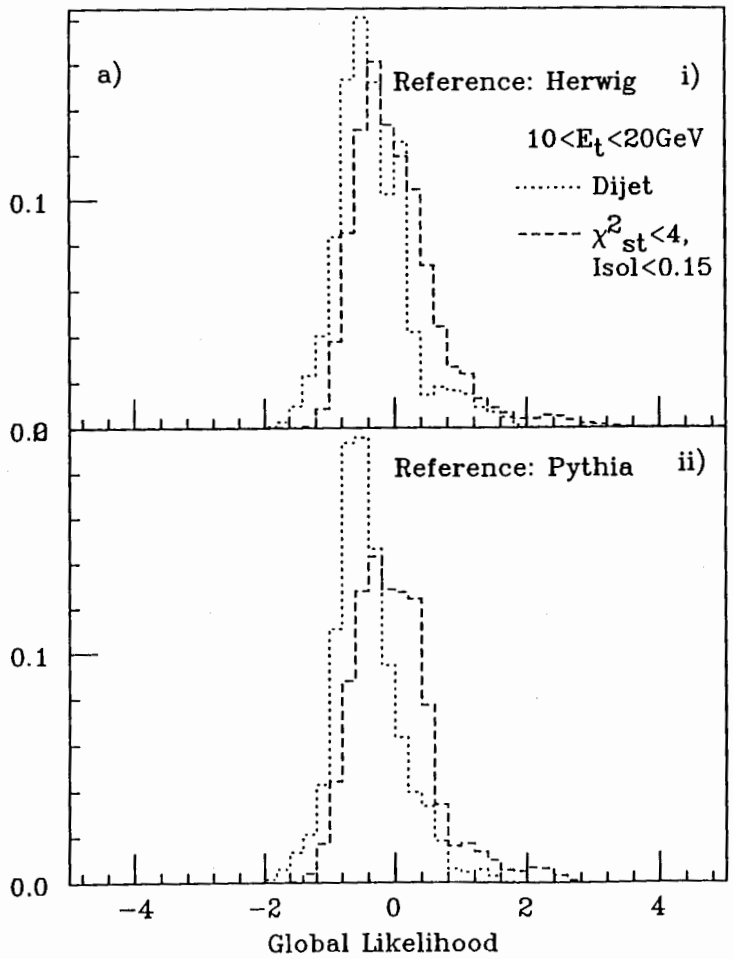

Figure 4.10: Distribution of global likelihood. Data from 1987 dijet events (dotted histogram) and 1988–89 γ_S+jet events in which strip chamber chi-squared value $\chi^2_a < 5$ (dashed), are shown in some energy interval. The calculation of likelihood had been performed using QCD Monte Carlo data as reference quark and gluon jets, which were generated with i) Herwig and ii) Pythia.

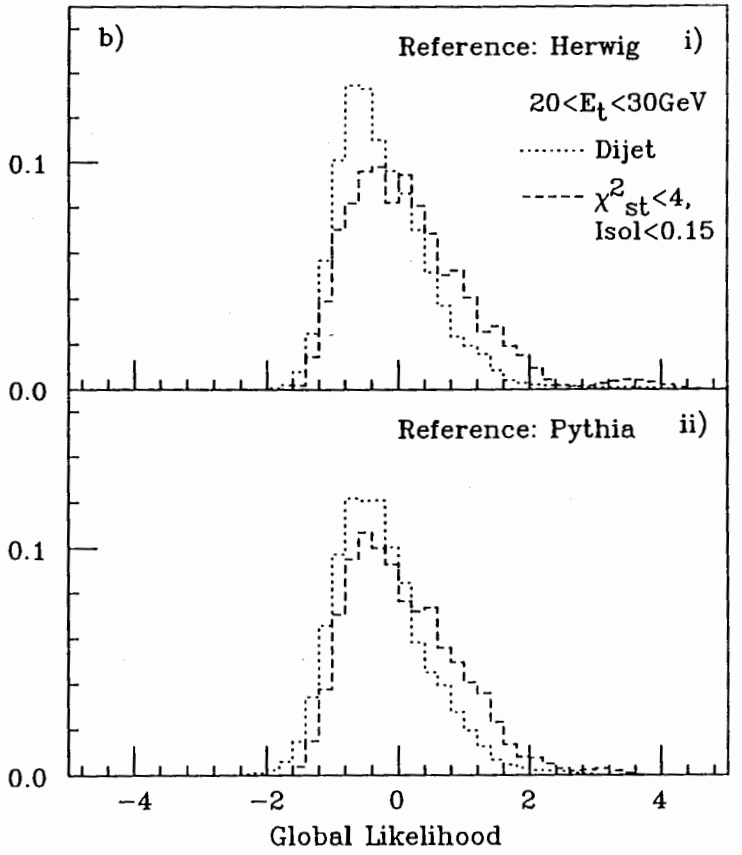

Figure 4.10 b

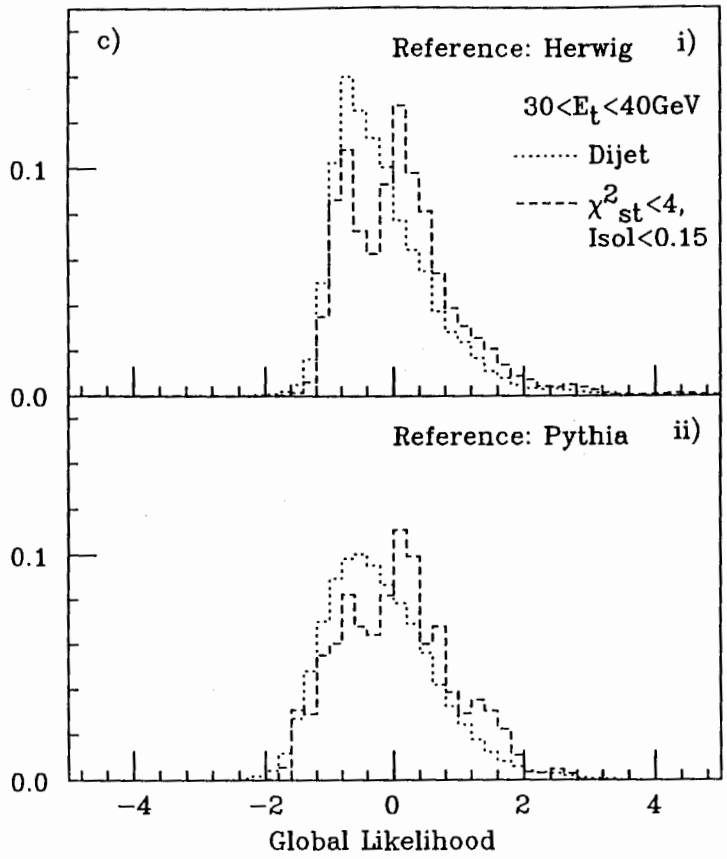

Figure 4.10 c

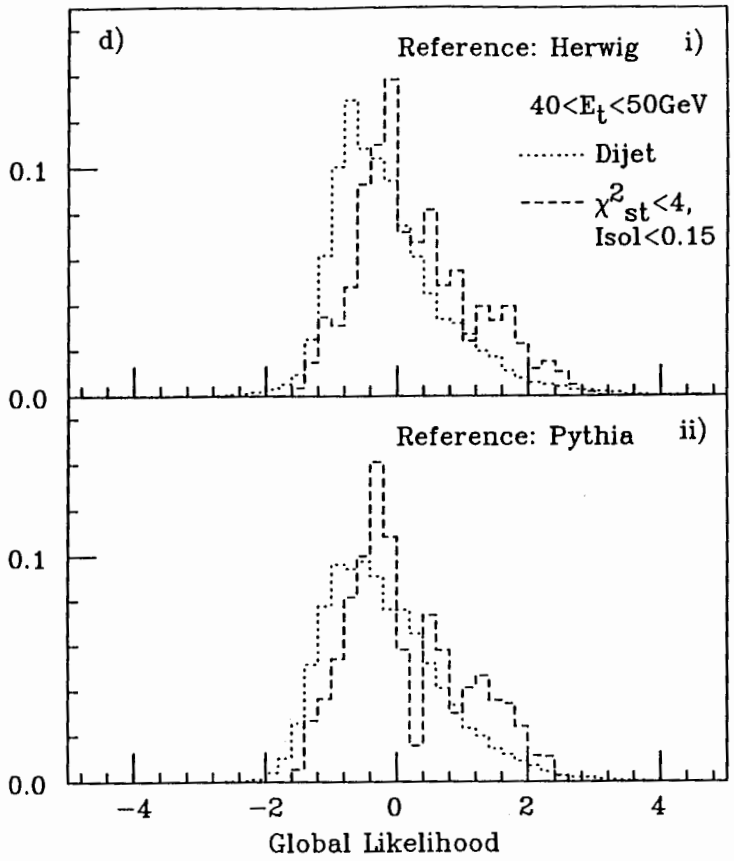

Figure 4.10 d

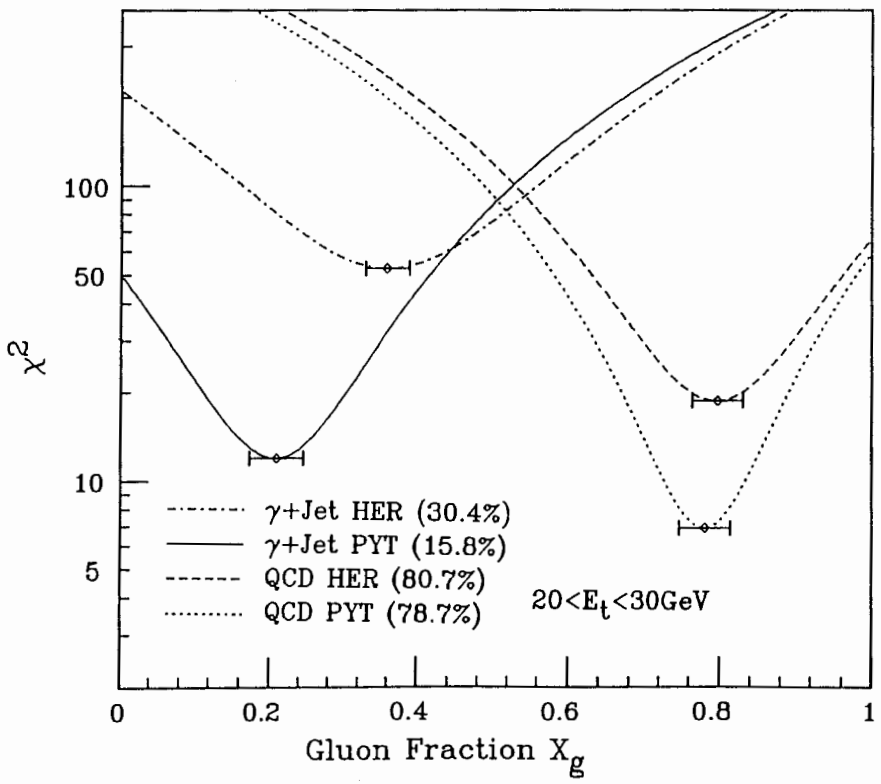

Figure 4.11: Chi-squared value, $\chi^2 = \sum_{i=1}^{50}(\frac{(D_i-(X_gG_i+(1-X_g)Q_i))}{\sigma_i})^2$, as a function of X_g, where G_i, Q_i, and D_i are numbers of jets in the i-th bin of likelihood histograms for gluons, quarks, and data sample respectively; σ_i is an error on D_i: $\sqrt{D_i}$. The samples are from the simulation of all QCD $2 \rightarrow 2$ processes and direct γ+jet events. Exact gluon fractions of these samples are in parentheses. The calculation of likelihood had been performed using QCD Monte Carlo data as reference quark and gluon jets, which were generated with Herwig and Pythia, and simulated with a detector simulation QFL. The sample generated with Herwig(Pythia) was analyzed using Herwig(Pythia) reference jets, whose random number set is different from that for the sample.

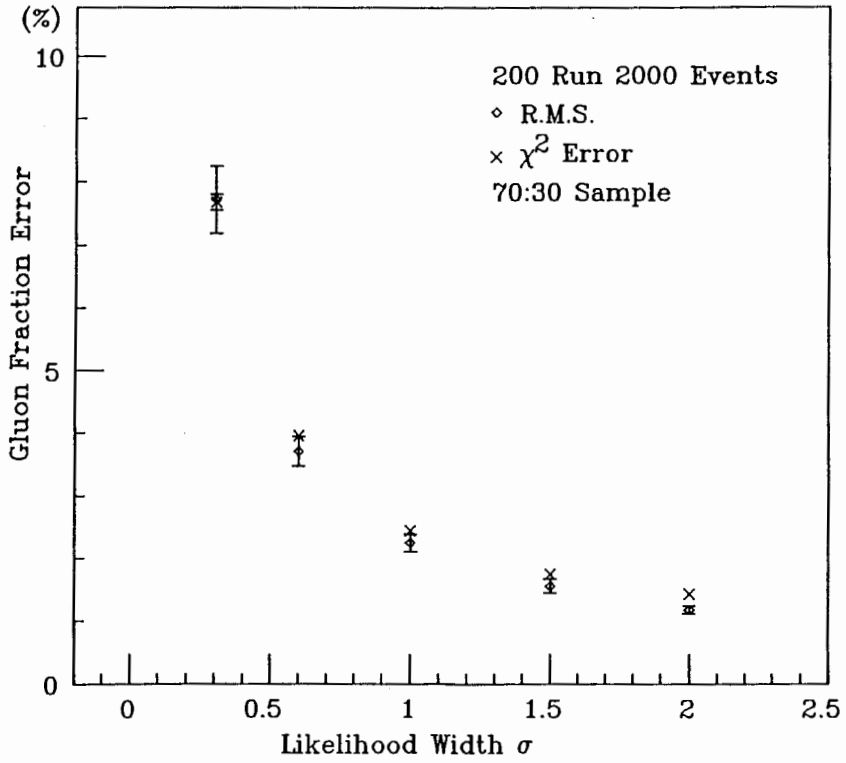

Figure 4.12: Dependence of gluon fraction error on the width of global likelihood distribution. The 200 different samples, each of which contains 2000 events, were produced. The quark/gluon of each sample is in the ratio 7:3. The gluon fraction and its error given by eq. 4.13 are calculated on an sample-by-sample basis. In this and subsequent figures, "*R.M.S*" refers to the deviation of the gluon fraction distribution from its mean, and "χ^2*error*" refers to the mean value of gluon fraction errors. The error bars of *R.M.S* and χ^2*error* are the standard deviation of the *R.M.S.* in the gluon fraction distribution, and that of the gluon fraction error distribution.

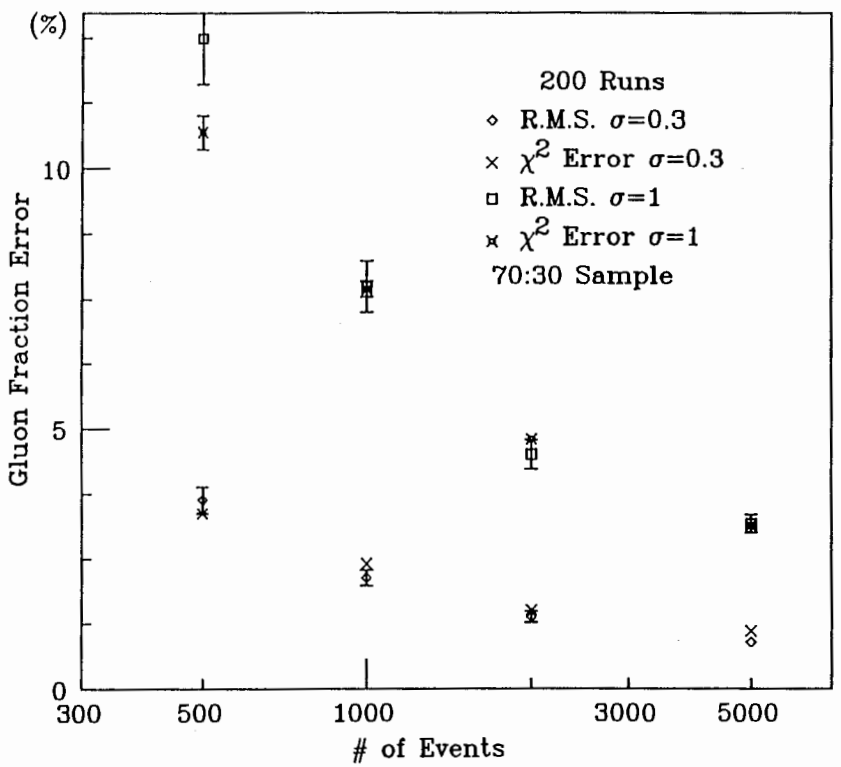

Figure 4.13: Dependence of gluon fraction error on the number of events in the sample. The 200 different samples, each of which contains 500, 1000, 2000, or 5000 events, were generated. The quark/gluon of each sample is in the ratio 7:3 and its likelihood width is 0.3 or 1. The gluon fraction and its error are calculated on an sample-by-sample basis. The error bars of *R.M.S* and χ^2*error* are the standard deviation of the *R.M.S.* in the gluon fraction distribution, and that of the gluon fraction error distribution.

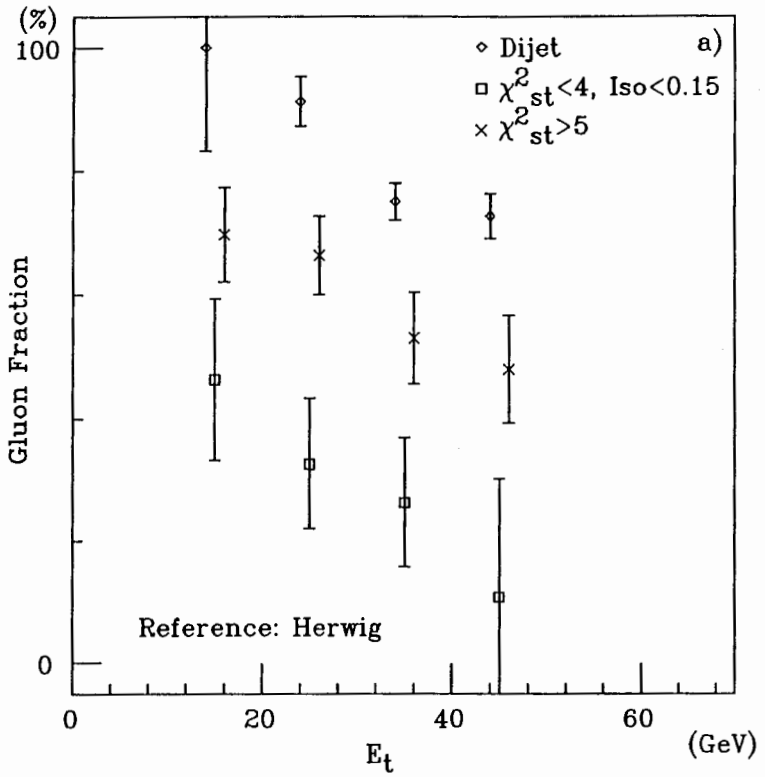

Figure 4.14: The fraction of the final state gluon in the dijet events from 1987 run, γ_S+jet events from 1988–89 runs, and π^0+jet events sample in which strip chamber chi-squared value $\chi^2_a > 5$, as a function of jet transverse energy E_t. The calculation of the fraction has been carried out using QCD Monte Carlo data as reference quark and gluon jets, which were generated with Herwig and Pythia, and simulated with a detector simulation QFL.

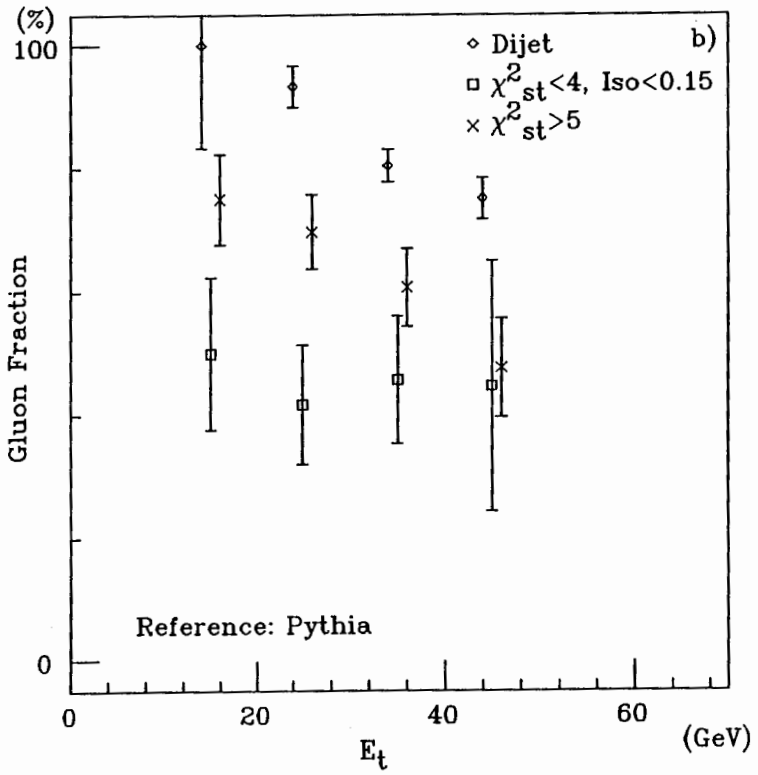
(%)
100
0
Gluon Fraction
◇ Dijet
b)
□ χ^2_{st}<4, Iso<0.15
× χ^2_{st}>5
Reference: Pythia
0
20
40
60
(GeV)
E_t

Figure 4.14 b

Appendix A

Gaussian likelihood distributions

The procedure to find a global likelihood from multi-dimensional likelihood functions is not unique. In this appendix, we point out a general relation which the properly defined likelihood should satisfy, and discuss a simple case where the likelihood distributions for two reference samples are Gaussian functions.

If a parameter L' is a properly defined likelihood, a relation for L',

$$L' = \ln\left[\frac{Q(L')}{G(L')}\right] , \tag{A.1}$$

or, equivalently, a relation for the quark fraction f_q,

$$f_q = \frac{Q(L')}{Q(L') + G(L')} = \frac{1}{1+\exp^{-L'}} \tag{A.2}$$

should hold. In eqs. (A.1) and (A.2), $Q(L')$ and $G(L')$ are likelihood distributions for the quark and gluon samples.

If one assumes that L is a certain parameter representing a measure of likelihood, and that $Q(L)$ and $G(L)$ are Gaussian functions with means μ_q and μ_g and variances σ_q and σ_g, respectively, then it is easy to show that the condition (A.1) requires

$$\mu_q = -\mu_g(=\mu),\ \sigma_q = \sigma_g(=\sigma), \tag{A.3}$$

and

$$\Delta/\sigma^2 = 1 , \tag{A.4}$$

where $\Delta = \mu_q - \mu_g = 2\mu$.

Suppose one found a parameter L whose distributions are Gaussian functions which satisfy eqs. (A.3). Then the condition (A.4) can be satisfied by a scale transformation,

$$L \to \lambda L = L',\ \mu \to \lambda\mu = \mu',\ \sigma \to \lambda\sigma = \sigma',\ \Delta \to \lambda\Delta = \Delta' \tag{A.5}$$

with $\lambda = \Delta/\sigma^2$. The separation power for such samples is given by a simple parameter σ' as

$$S = \frac{\Delta'}{\sigma'} = \frac{\Delta}{\sigma} = \sigma' . \tag{A.6}$$

Appendix B

Gluon polarization

This appendix describes the study of gluon polarization [61–64]. According to the QCD, the $\bar{p}p$ hard collisions at the CDF energy are dominated by the gluon-gluon scattering, i.e. the $g + g \rightarrow g + g$ process. In this process, the gluons are generally expected to be polarized in the scattering plane.

In case of the gluon hadronization, it is conceivable that the plane defined by the momenta of two particles in the first stage of decay, i.e. q and $\bar{q}$, or 2 g's, has a similar correlation with the polarization plane of the original gluon. We will denote by ω the angle between the $q - \bar{q}$ or $g - g$ plane in the initial hadronization and the polarization plane of the original gluon. From the symmetry consideration of the gluon polarization, the distribution of ω with respect to the gluon polarization vector is given by

$$\frac{dN}{d\omega} = f_0(1 + \alpha \cos 2\omega) , \tag{B.1}$$

where f_0 is a normalization constant. With momentum fraction z and ω, the parton splitting functions are

$$\begin{aligned} P_{gg}(z,\omega)/2 &= N_c[(1-z)/z + z/(1-z) + 2z(1-z)cos^2\omega] \ \textit{and} \\ P_{qg}(z,\omega)N_f &= (N_f/2)[1 - 4z(1-z)cos^2\omega] , \end{aligned} \tag{B.2}$$

where N_f and N_c are numbers of flavors and colors respectively. The coefficient α

in eq. B.1 may be written in the form

$$\alpha = \frac{-4(N_f - N_c)\langle z(z-1)\rangle}{N_f - 4N_c + 4N_c\langle 1/z\rangle + 2(N_c - N_f)\langle z(1-z)\rangle} . \tag{B.3}$$

It has been pointed out that α is quite small [62].

We made a first attempt to estimate the effects of polarization due to parton spins, taking no account of hadronization. It is not so clear, whether the parton shower configuration which reflects gluon polarization is kept in the final distribution of hadrons, after many stages of decay and gluon showers. We however assume that the gluon polarization is, to a certain extent, transferred to some hadrons and this transfer is especially strong when those hadrons have large momentum fractions.

Let us consider the asymmetry

$$A = \frac{d\sigma_{\parallel} - d\sigma_{\perp}}{d\sigma_{\parallel} + d\sigma_{\perp}} , \tag{B.4}$$

where $d\sigma_{\parallel}$ and $d\sigma_{\perp}$ are the cross sections for the process with the linear polarization parallel and perpendicular to the production plane, respectively. According to the lowest-order QCD calculation, the asymmetry A is zero as shown in fig. B.1. The asymmetry would be expected to be observable as an oblate transverse momentum distribution of the particles associated with jets. The decay products of gluons will form oblate jets with angular correlations which reflect the linear polarization of the parent. The asymmetry of jet fragments is defined as

$$A_f = \frac{P_{\parallel} - P_{\perp}}{P_{\parallel} + P_{\perp}} , \tag{B.5}$$

with $P_{\parallel}$ and $P_{\perp}$ the sum of the particle momenta in and perpendicular to the production plane, respectively.

For the tracked jet sample, 1987 dijet data were used (see chapter 3). For a given event we first get the longitudinal dijet center of mass system using the corrected 4-vector of clusters. In the Lorentz transformation to the c.m. system, the masses of all charged particles are assumed to be equal to the pion mass. In the dijet rest

frame, tracks within the jet cone were selected as associated with the jet. For each jet in the longitudinal dijet rest frame, we define the z' axis along the jet direction, and the y' axis along the direction of $\mathbf{p}_{beam} \times \hat{z}'$, where $\mathbf{p}_{beam}$ is the momentum of the proton, and $\hat{\mathbf{z}}'$ is the unit vector along the z' axis. Two possible axes of jet were considered. The first one was determined by the centroid of the calorimeter energy deposit. The second one was calculated by the vector sum of the 3-vectors of charged particles associated with the jet. For each jet, we calculate a tensor defined by,

$$T_{x'x'} = \sum_{i=1}^{n} p_{ix'}^2, \tag{B.6}$$

$$T_{x'y'} = T_{y'x'} = \sum_{i=1}^{n} p_{ix'} p_{iy'},$$

$$T_{y'y'} = \sum_{i=1}^{n} p_{iy'}^2,$$

where n stands for the number of tracks in a jet. We then transform the T-matrix to the principal axes coordinate system $S_0(\xi, \eta, z')$, where the T-matrix, T_0, is diagonal;

$$T_0 = \begin{pmatrix} d_1 & 0 \\ 0 & d_2 \end{pmatrix} \tag{B.7}$$

We choose ξ and η axes so that $d_1 > d_2$. We define the oblateness O of the transverse momentum distribution in the S_0 system by

$$O = \frac{d_1 - d_2}{d_1 + d_2}. \tag{B.8}$$

This quantity O is similar to the oblateness A_f defined in eq. B.5 as an observable quantity that shows the gluon polarization. We think the oblateness O is more suitable than A_f for this study, in view of the necessity to take into account the z' components of particle momenta as well as x' and y' components mathematically. We calculate oblateness for several cones and two choices of jet axis. In all these cases, quite obvious asymmetries are observed as shown in fig. B.2. Fig. B.3 shows that a mean of oblateness rises slowly as one reduces the radius of a jet cone, which

may in part be caused by a drop in the charged multiplicity within a cone. The mean oblateness decreases gradually with increasing the multiplicity as shown in fig. B.4. In case of quite low multiplicity, n$\leq$1, the oblateness is no longer defined. Therefore, we require more than two tracks in a jet cone for this analysis.

We have imposed a 0.3 GeV cut on P_{long}, which is momentum of a track along the jet axis, as well as a 0.35 GeV cut on P_t, transverse momentum relative to the beam axis, to insure the removal of soft track effects. At first we anticipated that the particles with small P_{long} had a bad influence on the measurement, because such particles often land outside a jet cone, even though the direction of them at the vertex point lie inside a cone. But as we will see later on, the direction of principal axis is almost independent of the cut on P_{long}. Fig. B.5 shows a gradual increase in the mean oblateness with increasing the cut value on P_{long}. Fig. B.6 shows behavior of the oblateness as a function of cluster E_t. Somehow there is a bump around 70 GeV, but we can say that the oblateness has a fairly weak dependence on E_t in the range of 30 GeV up to 110 GeV.

The distributions of rotation angle ω are shown in fig. B.7 for different size of the jet cones. The ω mentioned here is an angle between the production plane and the principal axis given from matrix T_0, and is not the same quantity that we considered in eqs. B.1 and B.3. The distribution is fitted with a function of the form:

$$N(\omega) = \frac{N_0}{\pi}[1 + \alpha \cos(2\omega)] \ . \tag{B.9}$$

According to QCD prediction, at the tree level, the ω distribution is flat, however the resulting α is undoubtedly not zero. It implies that jets are oblate with principal axes likely to be parallel rather than orthogonal to the production plane. Also, we see that α decreases as a cone size narrows down. In fig. B.8, we plot the α as a function of the cut value of P_{long}. The α is almost independent of the P_{long} cut, because the determination of principal axis is not influenced by soft tracks as

mentioned before.

It is interesting to compare the results presented in fig. B.7 with those obtained by a Monte Carlo study. But before describing that, let's touch briefly on the production of Monte Carlo sample. The events are produced with version 3.0 of Herwig. It has adopted the cluster model for hadron formation in jets; the inclusion of azimuthal correlations within jets due to gluon polarization; and azimuthal correlations within and between jets due to interference.

To define the jet, we draw a cone around the direction of parent partons in their rest frame, and then associate generated final particles inside this cone with a jet. Figs. B.9 and B.10 show the distributions of E_t of generated jets and multiplicity in the jet cone, in which pseudorapidity w.r.t the jet axis $\eta_\perp > 1.4$. The particle 4-vectors are calculated in two ways, first by using exact particle masses, and second by assuming all particles to have the pion mass. The second way corresponds to the fact we can not identify each particle in a jet at the experiment. As we mentioned before, we analyzed real data with pion mass assumed. We also used charged particles only for each case, because CTC can not observe neutral particles. The quantity α turns out insensitive to the mass of charged particles in a jet in fig. B.11. The αs appear to be the same within their standard deviations.

Further studies to be made will include the the momentum resolution of tracks and jet energy smearing as they might affect the measurement. The smearing not only depends on the detector geometry and performance, but also is caused by limitations of jet reconstruction using clustering algorithms. To estimate these effects, the generated events are pushed through the fast simulation program QFL version 2 [60] which reproduces the CDF detectors rather realistically, and full detector simulation CDFSIM (see chapter 3). The simulated events are clustered and analyzed in the same way as real data. Fig B.12 shows the oblateness O distribution for the real data and simulation data. The distribution of real data

peaks at larger O than the result with simulated events, but this trend is mainly due to the difference of the multiplicity which are shown in fig. B.10. The ω distribution is compared for QFL and CDFSIM in fig. B.13 c. The α predicted by QFL is roughly twice bigger than that of real data, on the other hand, CDFSIM prediction appears to be negative value.

We see that obviously the smearing effects due to the detector and algorithm affects the determination of ω. Also we note that our analysis is sensitive to details of the detector simulation. The question raised here is what in the simulation actually causes a change in the ω distribution and discrepancies between CDFSIM and QFL.

We calculate a Lorentz matrix to boost a event to its longitudinal CMS frame by using the corrected cluster energy. If the matrix is not correct and then the event is boosted to the "wrong" CMS frame, the x' components of track momenta will be overestimated. It may make a peak at zero in the ω distribution. Let this uncertainty of transformation to CMS frame be $\Delta\beta$. To evaluate $\Delta\beta$, we first define three inertial reference systems, K_{cms}, K_{gen} and K_{sim}. The K_{cms} is the longitudinal rest frame of two parent partons, which can be considered as a correct CMS frame. K_{gen} is the Laboratory frame, and K_{sim} is the longitudinal rest frame boosted by 4-vectors of jets simulated with QFL or CDFSIM. Let us suppose K_{cms} and K_{sim} systems move relative to the K_{gen} with velocity V_1 and V_2, respectively. The uncertainty of CMS frame, $\Delta\beta$, can be obtained easily by a Lorentz transformation formula. Since K_{gen} system moves with velocity $-V_1$ relative to the K_{cms},

$$\Delta\beta = \frac{\beta_1 - \beta_2}{1 - \beta_1\beta_2}, \tag{B.10}$$

where $\beta_1 = V_1/c$, $\beta_2 = V_2/c$ and c is the velocity of light. Fig B.14 shows the distributions of $\Delta\beta$ for QFL and CDFSIM. The width of $\Delta\beta$ distribution of CDFSIM is narrower than that of QFL.

Another possible cause of a peak or a dip in the ω distribution is a misdetermi-

nation of jet axis. The jet axis difference between simulation and generation data is shown in figs. B.15 and B.16. CDFSIM has better η and ϕ accuracy of jet axis than QFL. However, the thing is the difference of the accuracy between η and ϕ, or rather which accuracy is better than the other. For instance if the accuracy of η is worse than that of ϕ, y' components of particle momenta will be enhanced, and consequently there will be a dip at $\omega = 0$ like a ω distribution of CDFSIM. As a simple measure, consider the ratio of σ of the $\Delta\eta$ distribution to that of $\Delta\phi$. This ratio $\sigma_{\Delta\eta}/\sigma_{\Delta\phi}$ is 0.017 in CDFSIM, and 0.02 in QFL. We believe that the incongruity between QFL and CDFSIM is related to the ratio $\sigma_{\Delta\eta}/\sigma_{\Delta\phi}$ rather than $\Delta\beta$.

To understand this, we analyzed the generation data with simulation informations, i.e. jet axes and a Lorentz matrix calculated from 4-vectors simulated jets. Fig. B.17 shows the resulting ω distribution, i) in the case where we use a Lorentz matrix only, ii) in the case where we used jet axes only, iii) in the case where we used both Lorentz matrix and jet axes. we have known that a jet axis is not independent of a change of Lorentz matrix. The ϕ direction of jet momentum, however, is not changed even if we change a Lorentz matrix, because we now consider the longitudinal CMS frame, where the events are boosted along a beam direction (z axis) only. As shown in fig. B.17, the shape of ω distribution depends crucially on the accuracy of jet axis rather than that of Lorentz boost. It is interesting that we can reproduce the QFL and CDFSIM results in fig. B.13 almost completely in the analysis of generation data with jet axes obtained by a simulation.

We are also able to see the effect of track reconstruction inefficiencies by the reverse method. This time, we analyze the simulation data with the information from a generation. we use 4-vectors of parent partons to get jet axis and a Lorentz matrix. In fig. B.18, we show the ω distributions in three cases like fig. B.17. As we expected, changing jet axes reproduces the generation result shown in fig B.18

quite well. By comparing fig. B.17i with fig. B.18ii, or fig. B.17ii with fig. B.18i, we see that α is not affected by inefficiency of track reconstruction so much. QFL includes particle momentum resolution smearing and but does not model reconstruction efficiency, because it skips production of raw data. We conclude that the discrepancies between QFL and CDFSIM is caused by the position resolution of jets rather than a Lorentz boost error or the other effect, such as track reconstruction efficiency. It is important to remember the QCD prediction, at the tree level the polarization doesn't appear. Therefore even if the result with real data is confirmed not to be caused by the instrumental effects, it does not necessarily mean that the only polarization is mirrored in this observable. Finally, we show in Fig. B.19 the dependence of α on E_t for the real data and simulations. In the case of real data, α is decreasing with E_t and then is consistent to be zero above 70GeV within a error.

In conclusion, obviously, we observed the cos2ω behavior in the rotation angle ω distribution for 1987 central dijet events. This could imply that a memory of polarization of a jet initiator−parton, is retained, even after many branching. If confirmed, this would be clear evidence of the gluon-gluon scattering, because quark jets are not expected to be polarized. we have made a simulation study with Herwig event generator, and two simulations, QFL and CDFSIM. The obtained simulation results indicate that our analysis is very sensitive to the instrumental effects, especially jet position resolution with calorimeters. In figs. B.17 and B.18, we have demonstrated how the experimental effects may provide the change of ω distribution. If one understands these effects, it is still a feasible story to detect the gluon polarization in our fashion.

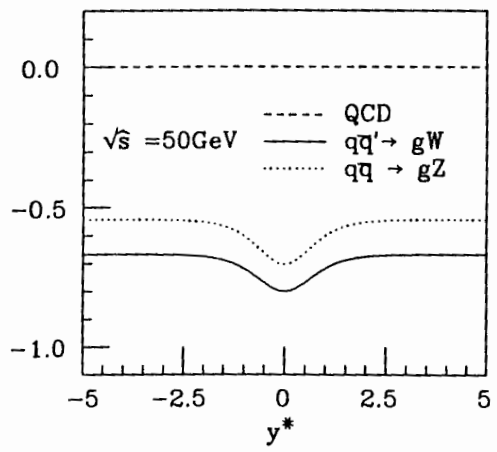

Figure B.1: Predicted asymmetry $\frac{d\sigma_{\parallel}-d\sigma_{\perp}}{d\sigma_{\parallel}+d\sigma_{\perp}}$ as a function of rapidity y^*. In this figure, "QCD" refers to all QCD $2 \rightarrow 2$ hard parton subprocesses which include gluon in the final state.

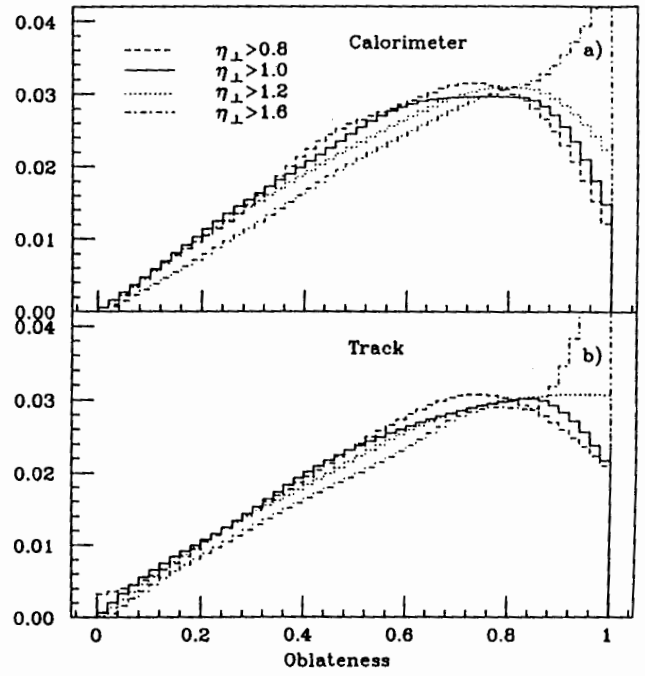

Figure B.2: Normalized and smoothed distribution of oblateness $\frac{d_1-d_2}{d_1+d_2}$, where d_1 and d_2 are given by eq. B.8. Data are shown for four different size of cones defined by a pseudorapidity with respect to a jet axis. a) Jet axis is determined by the calorimeter energy centroid ; b) vector sum of the momenta of charged particles associated with a jet.

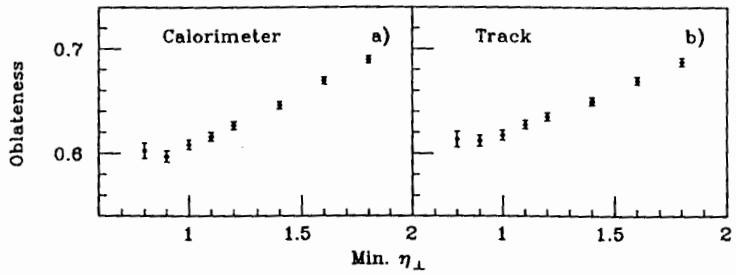

Figure B.3: Dependence of oblateness $\frac{d_1-d_2}{d_1+d_2}$ on the cone size defined by a pseudorapidity with respect to the jet axis. The points show mean values of oblateness and their statistical errors.

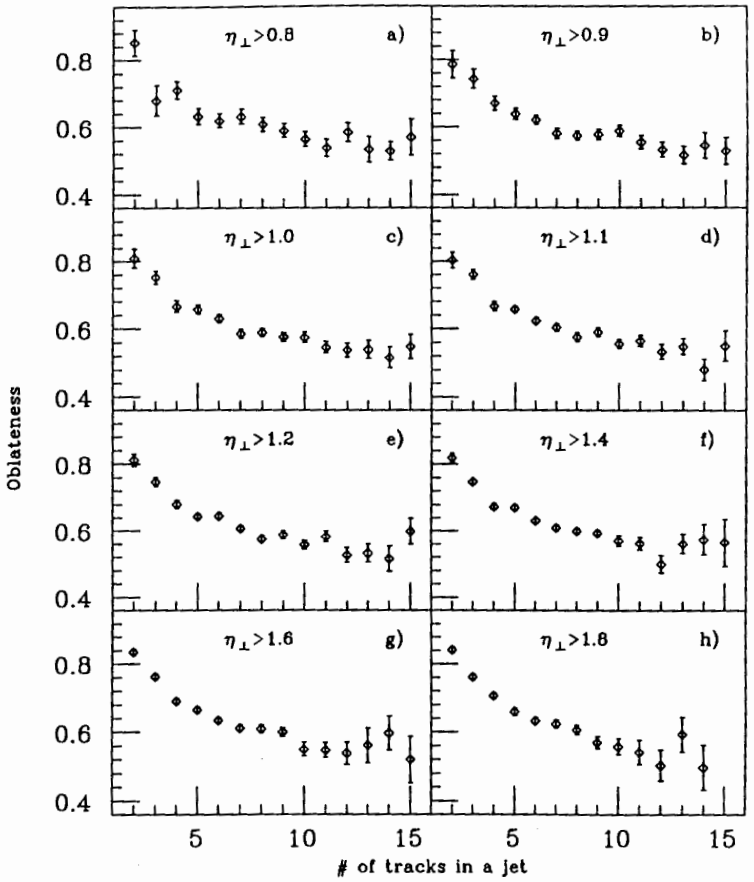

Figure B.4: Dependence of the oblateness $\frac{d_1-d_2}{d_1+d_2}$ on the mean charged particle multiplicity in a jet cone. The points show mean values of oblateness and their statistical errors. The jet cone is defined by a pseudorapidity with respect to the jet axis to associate tracks with a jet. The jet axis is determined by a energy centroid of calorimeter.

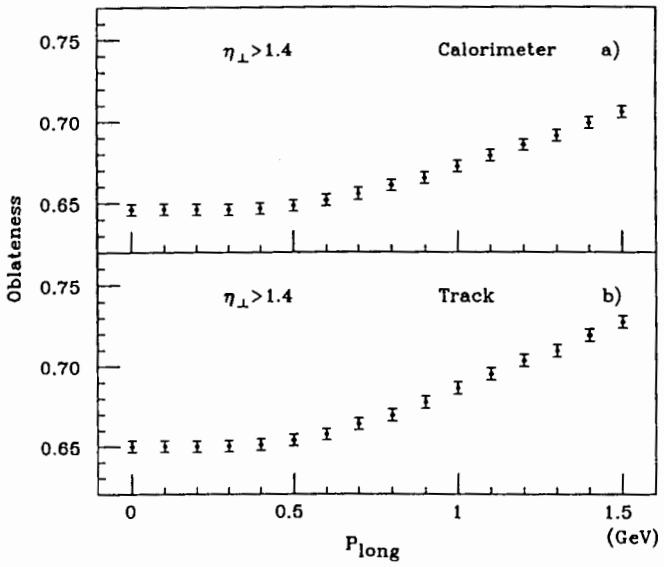

Figure B.5: Dependence of oblateness $\frac{d_1-d_2}{d_1+d_2}$ on the cut on P_{long}, which is momentum of a track along the jet axis. The points show mean values of oblateness and their statistical errors. In this and subsequent figures, "Calorimeter" and "Track" denote that the jet axis is determined by the energy centroid of calorimeter, and the vector sum of the momenta of charged particles associated with a jet, respectively.

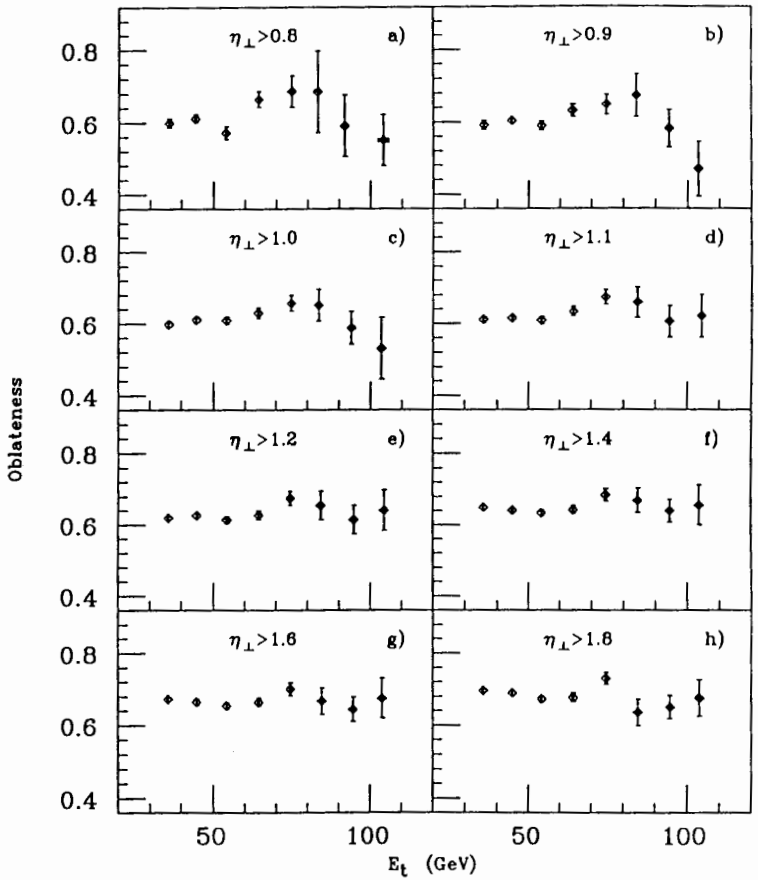

Figure B.6: Dependence of the oblateness $\frac{d_1-d_2}{d_1+d_2}$ on the corrected transverse energy of the jet cluster. The points show mean values of oblateness and their statistical errors for eight different jet cones. In this and subsequent figures, the minimum pseudorapidity with respect to the jet axis is referred to as "$\eta_\perp$".

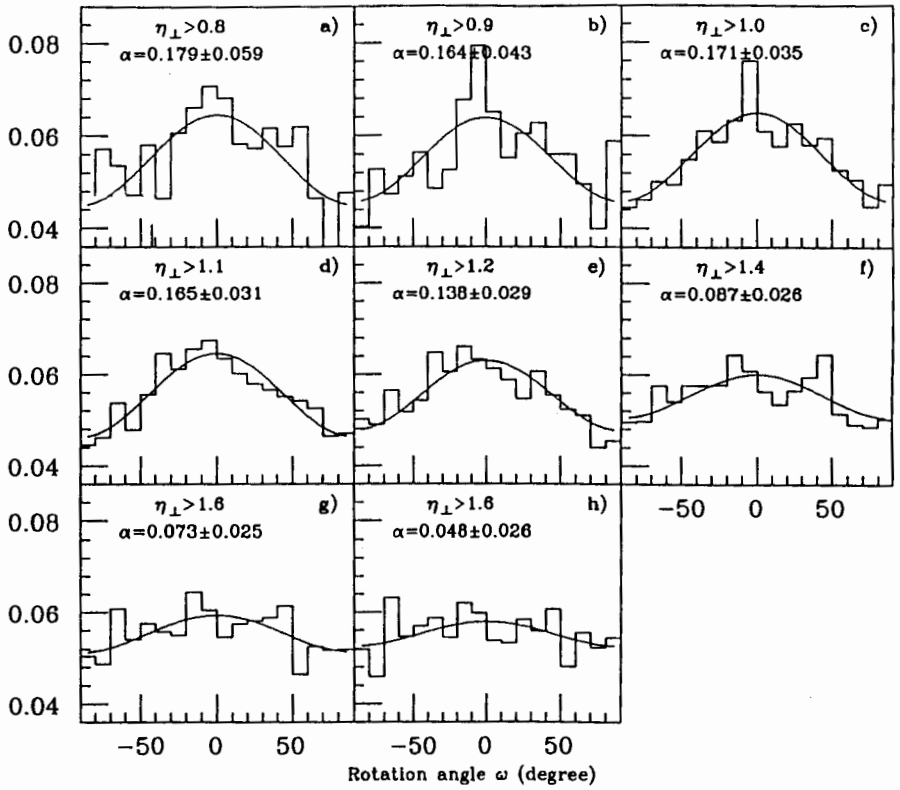

Figure B.7: Distribution of the rotation angle ω, which is an angle between the production plane and the principal axis of jet. The curves are fits of the form $N(\omega) = N_0[1 + \alpha cos\ 2\omega]$ for various size of jet cones. The data are central-central dijet events from 1987 run.

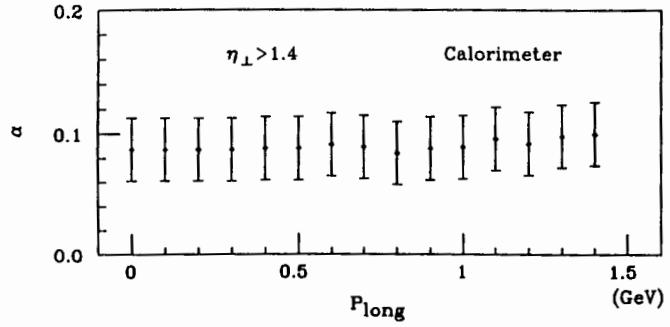

Figure B.8: Dependence of α on the cut on P_{long}, which is momentum of a track along the jet axis. The points show α and their standard deviations.

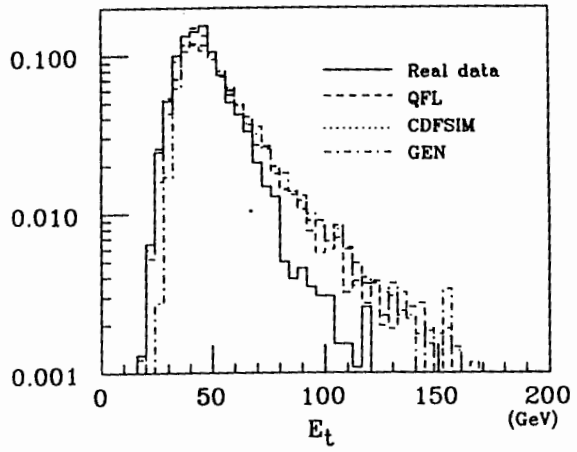

Figure B.9: Distribution of the corrected transverse energy E_t. Data are from central-central dijet events from 1987 run (solid histogram); simulated with QFL (dashed); simulated with CDFSIM (dotted). The uncorrected E_t distribution of the generated events with Herwig is also shown (dot-dashed histogram).

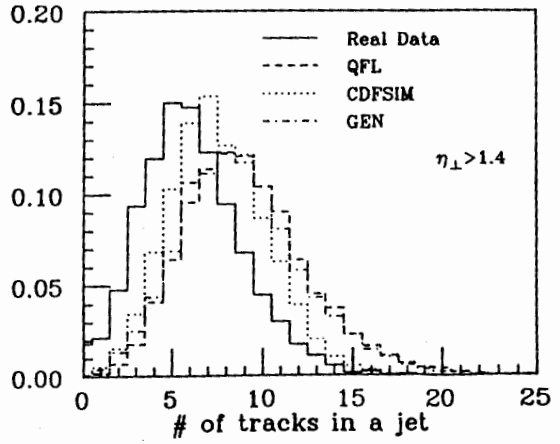

Figure B.10: Distribution of charged particle multiplicities in a jet, The track association with jets uses the track pseudorapidity $\eta_\perp$ with respect to the jet axis. The minimum $\eta_\perp$ was taken to be 1.4.

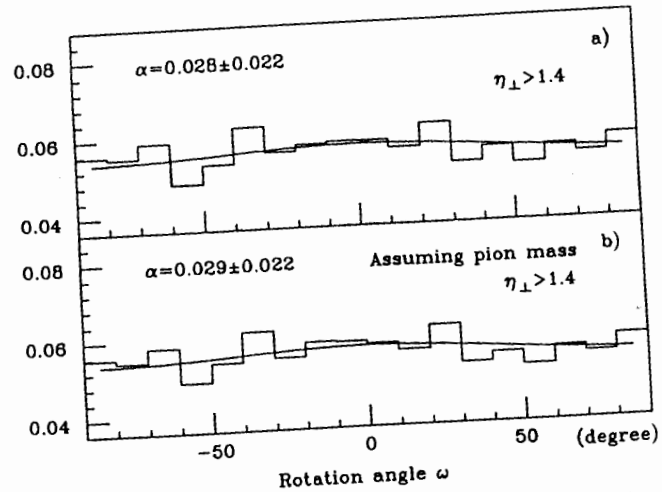

Figure B.11: Distribution of the rotation angle ω. The curves are fits of the form $N(\omega) = N_0[1 + \alpha cos\ 2\omega]$. The data is a Monte Calro sample of pairs of gluon jets, which is generated with Herwig event generator. The calculation of ω is performed, a) taking into account charged particles' contribution only, and b) assuming pion mass.

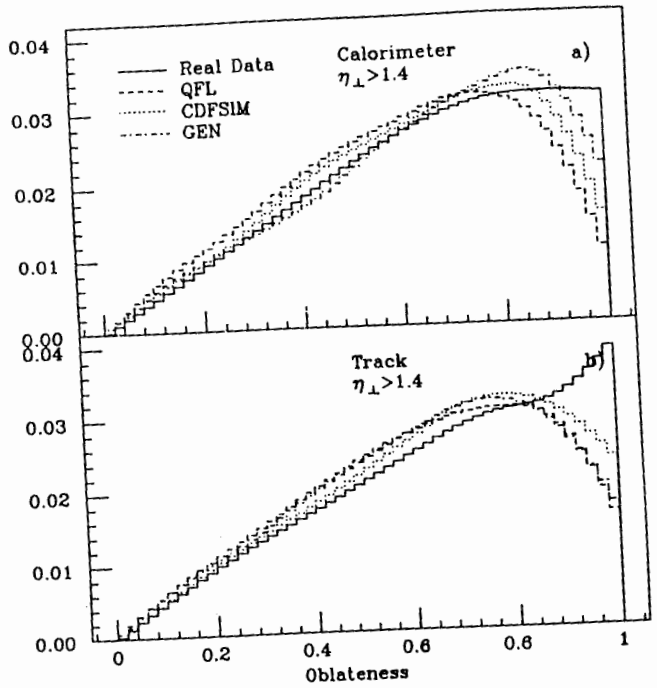

Figure B.12: Normalized and smoothed distribution of oblateness $\frac{d_1-d_2}{d_1+d_2}$, where d_1 and d_2 are given by eq. B.8.

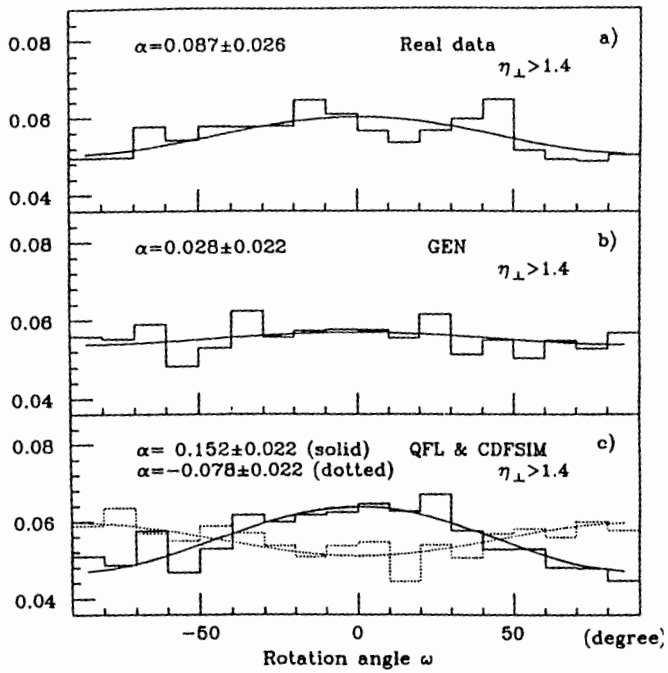

Figure B.13: Distribution of the rotation angle ω. The curves are fits of the form $N(\omega) = N_0[1 + \alpha cos\ 2\omega]$. The data are a) from 1987 run; b) generated with Herwig; c) simulated with QFL (solid histogram) and CDFSIM (dotted histogram).

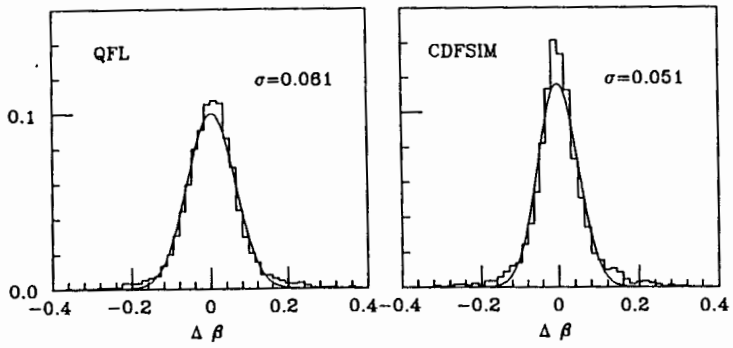

Figure B.14: Uncertainty of the transformation from Laboratory frame to the longitudinal CMS frame for QFL and CDFSIM.

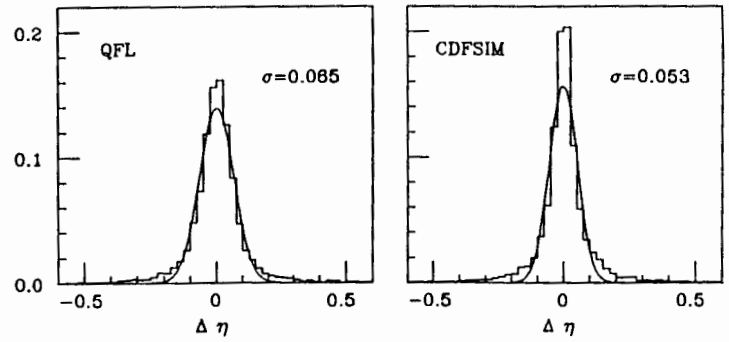

Figure B.15: η difference of jet axes between generation and simulation data.

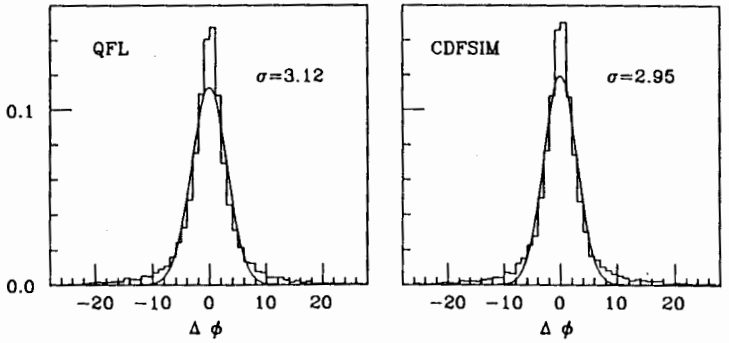

Figure B.16: ϕ difference of jet axes between generation and simulation data.

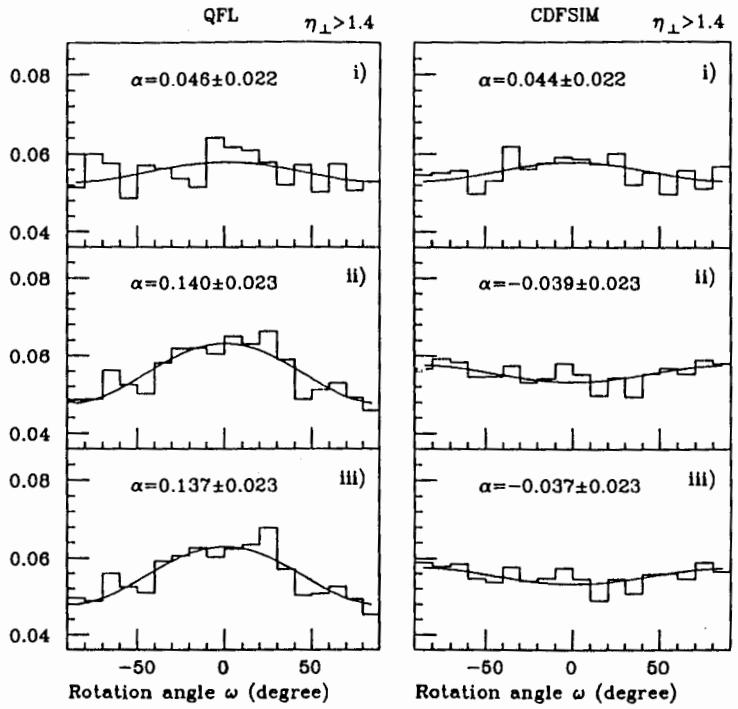

Figure B.17: Distribution of rotation angle ω obtained by the analysis of generation data with information on jet axes and a Lorentz matrix from simulations. The analysis was carried out under the following conditions: we use i) a Lorentz matrix derived from the simulation result only; ii) jet axes of simulated jets only; iii) both jet axis and a Lorentz matrix.

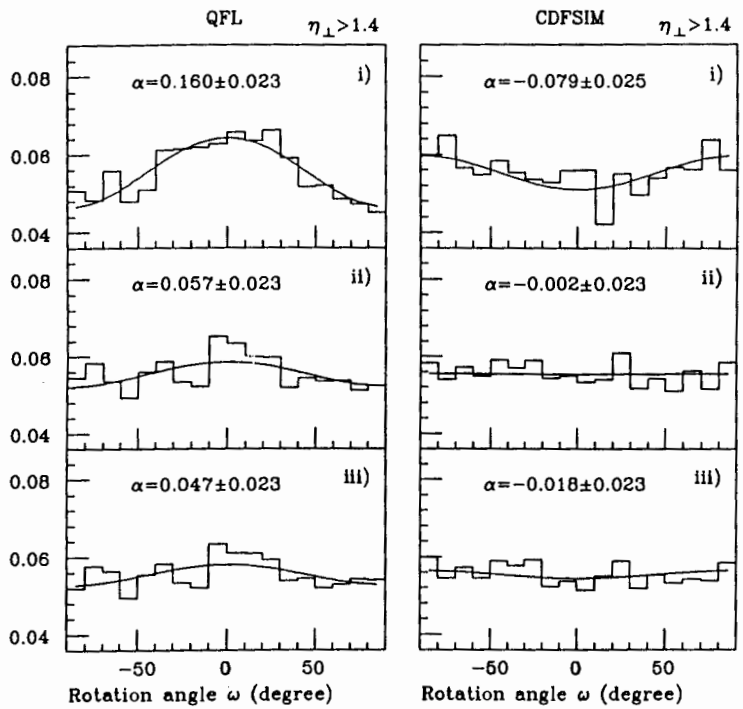

Figure B.18: Distribution of rotation angle ω obtained by the analysis of simulation data with the generation information on jet axes and a Lorentz matrix derived from 4-vectors of parent partons. The analysis carried out under the following conditions: we use i) a Lorentz matrix only; ii) jet axes only; iii) both jet axis and a Lorentz matrix, as the information from generation.

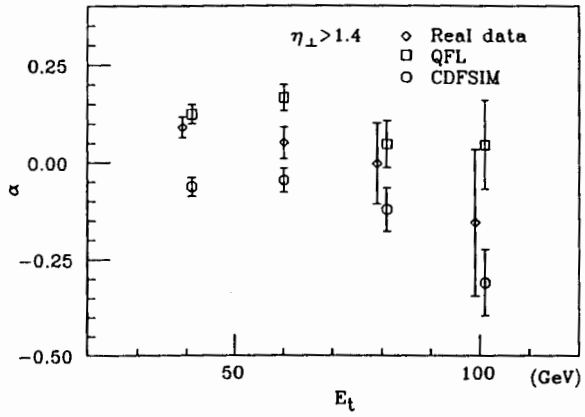

Figure B.19: Dependence of the α on the corrected transverse energy of the jet cluster. The points show mean values of α and their statistical errors.

Appendix C

Correlation in polarization of gluon jets

In this appendix we discuss the correlation in linear polarization of two scattered gluons. Even at the lowest order, the perturbative QCD predicts that the correlation is present, although the asymmetry A defined in eq. B.4 is absent, because the cross section of $ab \to g_\perp g_\perp$ is not equal to that of $ab \to g_\perp g_\parallel$. The correlation of the $gg \to gg$ process, for instance, has a matrix element proportional to

$$\frac{A_{gg} - B_{gg}}{A_{gg} + B_{gg}} = \frac{\lambda^2 + 3}{\lambda^2 + 11 - 16/(1-\lambda^2) + 16/(1+\lambda)^2 + 16/(1-\lambda)^2} , \qquad \text{(C.1)}$$

where $\lambda = cos\theta^*$ cosine of the scattering angle in the rest frame of subprocess and

$$A_{ab} \equiv d\sigma(ab \to g_\perp g_\perp)/d\lambda = d\sigma(ab \to g_\parallel g_\parallel)/d\lambda , \qquad \text{(C.2)}$$

$$B_{ab} \equiv d\sigma(ab \to g_\perp g_\parallel)/d\lambda .$$

We then find the distribution of $\Delta\omega$, which is the difference of the rotation angle ω in two gluon jets

$$\frac{d\sigma}{d\Delta\omega} \propto 1 + (\alpha^2/8)\frac{A_{gg} - B_{gg}}{A_{gg} + B_{gg}} cos\ 2\Delta\omega . \qquad \text{(C.3)}$$

Unfortunately, in the absence of any Monte Carlo's including the polarization correlation effects in the hard process computation, we cannot estimate the resulting

correlations between jets from the simulation study completely. We then decided to compute the polarized cross section of all possible processes, following Y. Hara and S. Sakai. The predicted correlation between jets of the subprocess a) $g\ g \to g\ g$ and b) $q\ \overline{q} \to g\ g$ as a function of η are shown in fig. C.1. At $\eta = 0$, the central region, the correlations of the processes a) and b) attain their maximum and minimum value respectively. Therefore at the central region, it seems more easy to measure the correlation. From the sign of the correlation, we see that the polarization vector of a jet is likely to be parallel to the other in the subprocess a) , while in b) the vector is mainly close to the other. As already remarked in Appendix B, the result obtained from the lowest order QCD calculation could be overestimated, because the parton shower and fragmentation would weaken the correlation, although the higher-order loop diagrams would lead to increased the cross sections which reflect the polarization. We also may expect the existence of the polarization due to another degree of freedom, such as colors which, if confirmed, might change the above results drastically.

Studying the correlation in polarization of two gluon jets, it is perhaps reasonable to boost the particles into the rest frame, rather than the longitudinal rest frame. We can not compare two rotation angle ωs directly in the longitudinal rest frame, because of the acolinearity due to the pointing resolution of the detector and the intrinsic k_t. In the transverse plane of the dijet rest frame, the jet axis of the leading is not necessarily parallel to that of a recoil jets. We require here both jets should have more than 0.4 oblateness. Fig. C.2 shows a scatter plot of the rotation angle ω of the leading jet versus that of the second jet. There is no ω correlation between jets. This is rather unexpected results, because the polarization correlation becomes easier to catch than single gluon polarization discussed before, from a theoretical point of view. In fig. C.3, we show the distribution of $\Delta\omega$ weighted by oblateness and that not weighted. For the sake of comparison, we plot the CDFSIM results

(dotted histograms) too. In both of these cases, the distributions are approximately flat. we also note that there is no significant discrepancies between two histograms. We think that the treatment of acolinearity is sufficiently difficult that no clear conclusions have been reached here. Of course, there remains the question what quantity in the experiment best reflect the polarization of gluons. We are also aware of the various difficulties with the treatment of fragmentations of two jets at a time.

Finally, we study the dependence of the oblateness O and α on charged particle momentum fraction X_p. On the assumption that the polarization of parents parton is mainly transferred to the hadrons with large X_p, one can find much clear signal of the polarization by using hard tracks only. As shown in fig. C.4, the mean oblateness increases gradually, when X_p cut increases. We believe this comes from the reduction of the average multiplicity. In fig. C.5, we see that the α becomes bigger as X_p cut becomes tighter. This behavior of α is not yet complete clear, because of poor statistics. Fig. C.6. shows distributions of $\Delta\omega$ for various X_p cuts. All distributions are consistent with to be flat within a statistics

We have tried to see the correlation of polarization between gluon jets, but as shown in figs. C.2 and C.3, little physical signal have been found. This may be counterintuitive, because QCD predicts that the correlation exists even at the tree level as shown in fig. C.1, and consequently $\Delta\omega$ should have peaked at zero. Concerning the correlation, we think so far that no impressive conclusion can be given.

We have suffered from the lack of knowledge about details of detector characteristics. We then suggest to compare the other $2 \to 2$ process including gluons expected to be strongly polarized with the result in this note. For example, in the W/Z production with a gluon jet, i.e., $q\ \bar{q}' \to g$ W and $q\ \bar{q} \to g$ Z, most of jets are predicted to be polarized perpendicular to the production plane, as shown

in fig. B.1. Therefore if a large amount of W/Z + one jet events were available, one could get the evidence of gluon polarization without this type of worry due to detector originated uncertainties, by comparing the value of α for jets associated W/Z with our result.

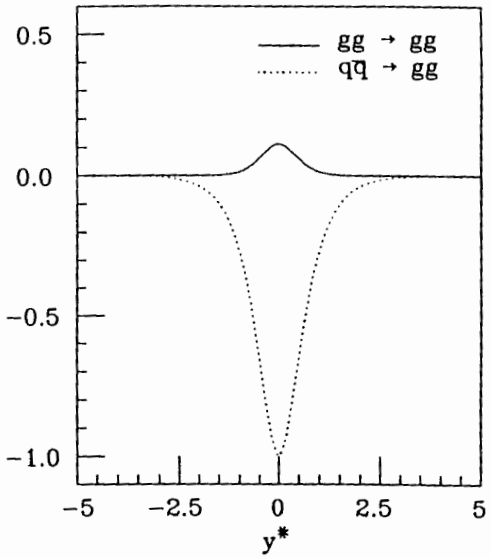

Figure C.1: Predicted correlations between gluon jets as a function of rapidity y^*.

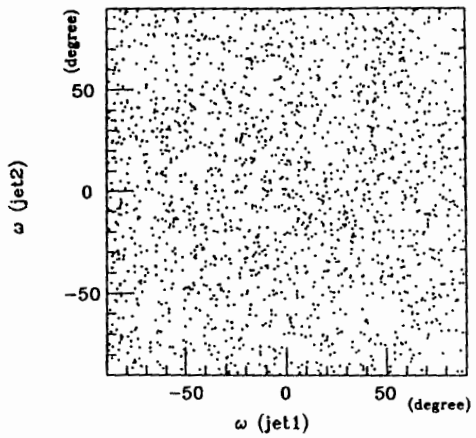

Figure C.2: Rotation angle ω correlation between jets. We required both jets with oblateness $\frac{d_1-d_2}{d_1+d_2} \geq 0.4$.

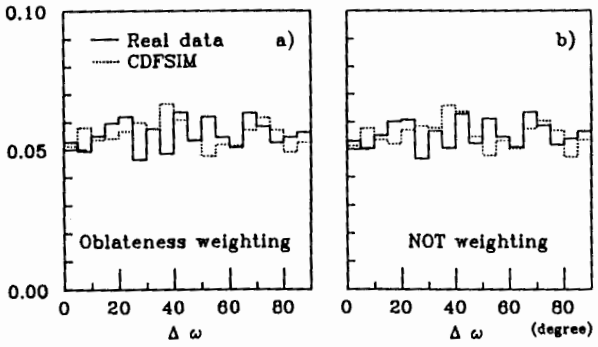

Figure C.3: Distribution of $\Delta\omega$, which is an angle between polarization vectors of dijet. Histogram a) is weighted by the sum of oblateness of jets, b) is equal weight.

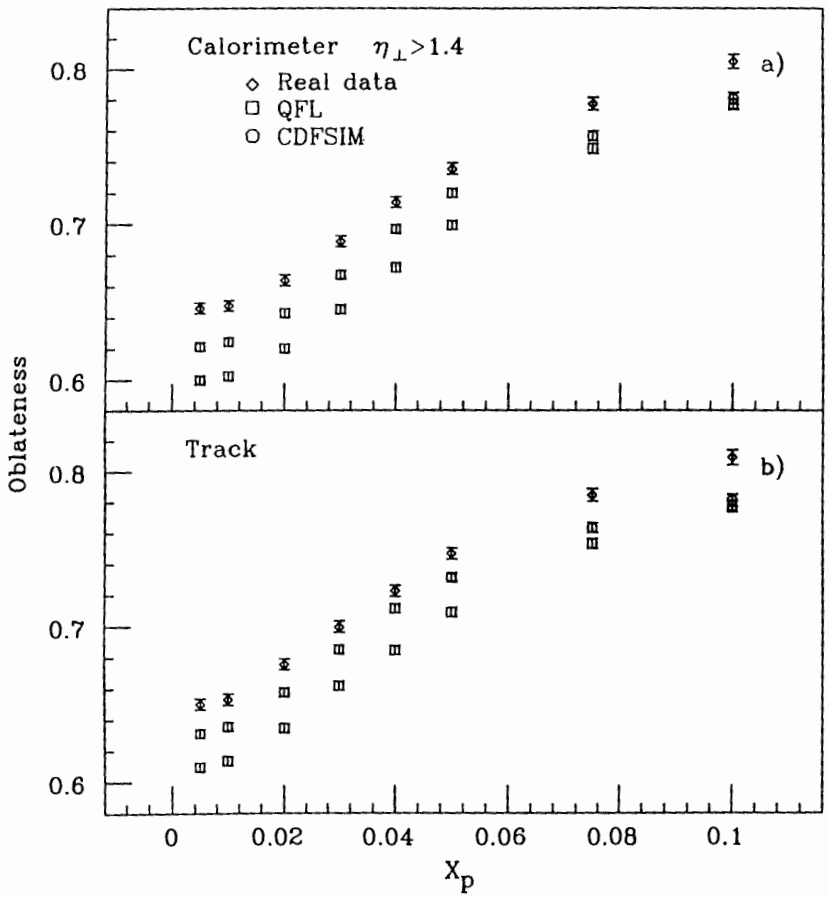

Figure C.4: Dependence of oblateness $\frac{d_1-d_2}{d_1+d_2}$ on the charged particle momentum fraction cut for the real data and two simulations. a) Jet axis is determined by the calorimeter energy centroid ; b) vector sum of the momentum of charged particles associated with a jet.

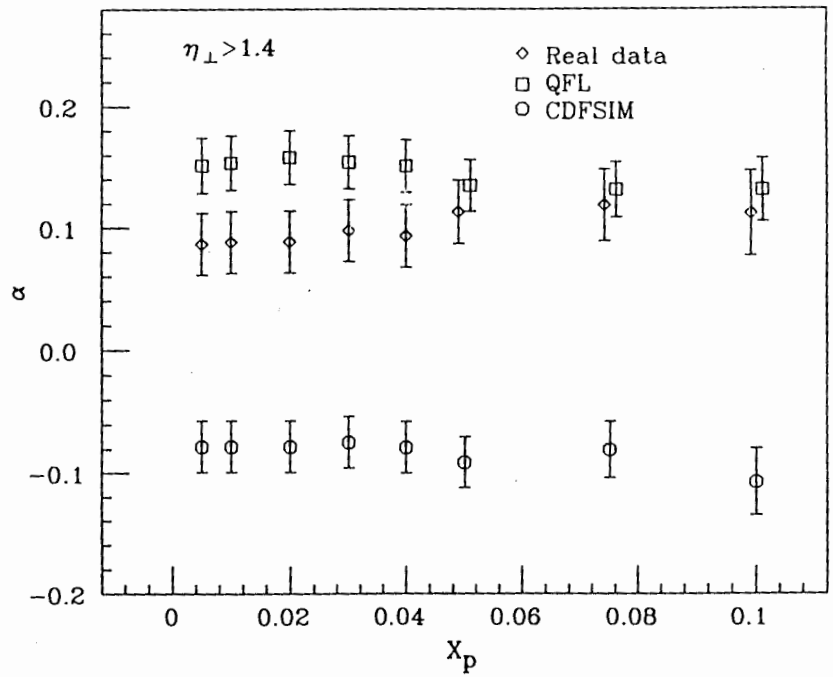

Figure C.5: Dependence of α on charged particle momentum fraction cut. The data are from 1987 central-central dijet events; simulated by QFL and CDFSIM.

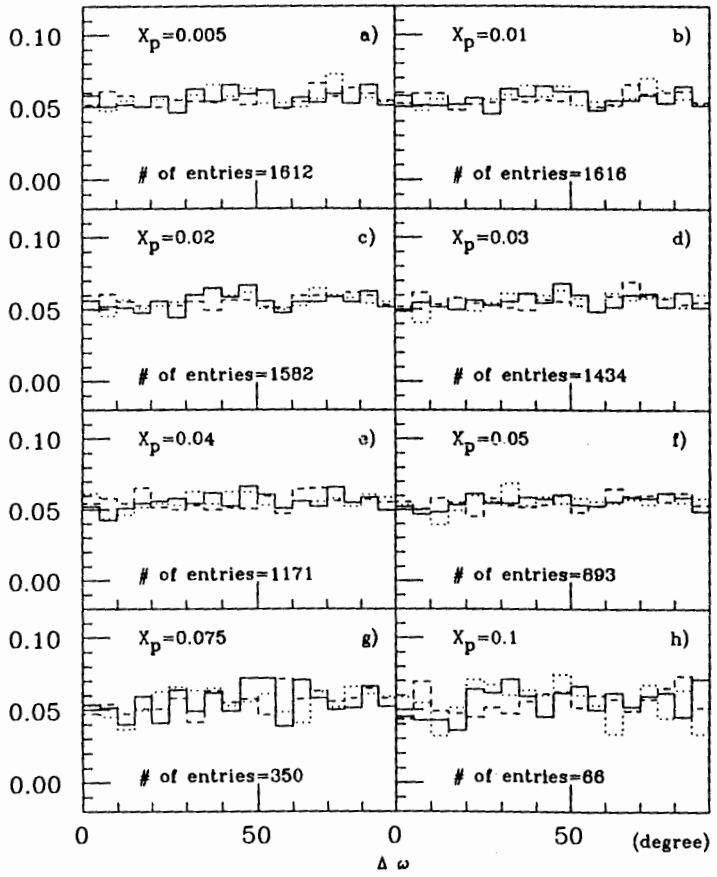

Figure C.6: Distribution of $\Delta\omega$, which is an angle between polarization vectors of two jets. Data from 1987 run, QFL and CDFSIM are shown for eight different conditions of the cut on charged particle momentum fraction X_p. In figures, "# of entries" is the number of real data used.

Bibliography

[1] M. Gell-Mann, Phys. Lett. 8 (1964) 214

[2] M.Y. Han and Y. Nambu, Phys. Rev. 139 (1965) B1006

[3] SLAC-MIT collaboration, Ann. Rev. Nucl. Sci. 22 (1972) 203

[4] J.D. Bjorken, Phys. Rev. 179 (1959) 1547

[5] R.P. Feynman, Phys. Rev. Lett. 23 (1969) 1415

[6] E. Eichten, I. Hinchliffe, K. Lane and C. Quigg, Rev. of Mod. Phys. 56 (1984) 579

[7] D.W. Duke and J.F. Owens, Phys. Rev. D30 (1984) 49

[8] W. Bartel et.al., Z. Phys. C33 (1986) 23

[9] F.E. Paige and S.D. Protopopescu, in Proc. Snowmass DPF summer study (1986)

[10] H.-U. Bengtsson and T. Sjöstrand, Computer Phys. Comm. 46 (1987) 43

[11] T. Sjöstrand , Computer Phys. Comm. 39 (1986) 347;
T. Sjöstrand and M. Bengtsson, Computer Phys. Comm. 43 (1987) 367

[12] B.R. Webber, Cavendish-HEP-88/6, August 1988;
B.R. Webber, Phys. Lett. 193B (1987) 91

[13] R.D. Field and R.P. Feynman, Nucl. Phys. B136 (1978) 1

[14] M.D. Corcoran, Phys. Rev. D32 (1985) 592;
M.W. Arenton et al.(E609), Phys. Rev. D31 (1985) 984

[15] C.de Marzo et al.(NA5), Nucl. Phys. B211 (1983) 375; B234 (1984) 1

[16] S. Wolfram, in Proc. 15th Rencontre de Moriond (1980), ed. J.Tran Thanh Van

[17] G.C. Fox and S. Wolfram, Nucl. Phys. B168 (1980) 285

[18] R.D. Field and S. Wolfram, Nucl. Phys. B213 (1983) 65

[19] T.D. Gottschalk, Nucl. Phys. B214 (1983) 201; B227 (1983) 413

[20] G. Marchesini and B.R. Webber, Nucl. Phys. B238 (1984) 1

[21] B.R. Webber, Nucl. Phys. B238 (1984) 492

[22] T.D. Gottschalk, in Proc. UCLA workshop on SSC physiscs (1986)

[23] Yu.L. Dokshitzer, V.S. Fadin and V.A. Khoze, Phys. Lett. 115B (1982) 242;
Yu.L. Dokshitzer, V.A. Khoze, S.I. Troyan and A.H. Mueller, Rev. of Mod. Phys. 60 (1988) 373

[24] K. Shizuya and S.-H.H. Tye, Phys. Rev. Lett. 41 (1978) 787

[25] M.B. Einhorn and B.G. Weeks, Nucl. Phys. B146 (1978) 445

[26] L.M. Jones, Tsukuba preprint UTHEP-189 (1989)

[27] Z. Fodor, ITP Budapest Report No.465 (1989)

[28] W. Bartel et al., Phys. Lett. 123B (1983) 460

[29] A. Petersen et al., Phys. Rev. Lett. 55 (1985) 1954

[30] M. Derrick et al., Phys. Lett. 165B (1985) 449

[31] Y.K. Kim et. al., KEK preprint 89-44 (1989)

[32] P. Ghez and G. Ingelman, DESY preprint DESY 86-110 (1986);
G. Arnison et al., Nucl. Phys. B276 (1986) 253

[33] S.J. Brodsky and J.F. Gunion, Phys. Rev. Lett. 37 (1976) 402

[34] K. Konishi, A. Ukawa and G. Veneziano, Nucl. Phys. B157 (1979) 45

[35] A.H. Mueller, Nucl. Phys. B241 (1984) 141;
J.B. Gaffney and A.H. Mueller Nucl. Phys. B250 (1985) 109

[36] H. Minemura et al., Nucl. Instr. and Meth. A238 (1985) 18.

[37] F. Snider et al., Nucl. Instr. and Meth. A268 (1988) 75

[38] F. Bedeschi et al., Nucl. Instr. and Meth. A268 (1988) 50

[39] S. Bhadra et al., Nucl. Instr. and Meth. A268 (1988) 92

[40] M. Atac et al., Nucl. Instr. and Meth. A269 (1988) 40

[41] L. Balka et al., Nucl. Instr. and Meth. A267 (1988) 272

[42] R.G. Wagner et al., Nucl. Instr. and Meth. A267 (1988) 330

[43] K. Yasuoka et al., Nucl. Instr. and Meth. A267 (1988) 315

[44] S. Bertolucci et al., Nucl. Instr. and Meth. A267 (1988) 301

[45] Y. Fukui et al., Nucl. Instr. and Meth. A267 (1988) 280

[46] Proceedings of the gas sampling calorimetry workshop II, Fermilab, 1985

[47] G. Brandenburg et al., Nucl. Instr. and Meth. A267 (1988) 257

[48] S. Cihangir et al., Nucl. Instr. and Meth. A267 (1988) 249

[49] G. Ascoli et al., Nucl. Instr. and Meth. A268 (1988) 33

[50] K. Byrum et al., Nucl. Instr. and Meth. A268 (1988) 46

[51] H. Frish et al., CDF Note No.250 (1984); No.416 (1986)

[52] G. Drake et al., Nucl. Instr. and Meth. A269 (1988) 68

[53] E. Barsotti et al., Nucl. Instr. and Meth. A269 (1988) 82

[54] D. Amidei et al., Nucl. Instr. and Meth. A269 (1988) 51

[55] D. Brown et al., CDF Note No.605

[56] D. Brown and R. Carey, CDF Note No.755

[57] B. Hubbard, CDF Note No.824

[58] A. Byon and A. Para, CDF Note No.570; No.571

[59] J. Proudfoot, CDF Note No.633

[60] D. Brown, S. Kannappan and M. Shapiro, CDF Note No.753

[61] S.J. Brodsky, T.A. Degrand and R.F. Schwitters, Phys. Lett. 79B (1978) 255

[62] Y. Hara and S. Sakai, Tsukuba preprint UTHEP

[63] H.A. Olsen, P. Osland and I. Øverbø, Phys. Lett. 89B (1980) 221

[64] A. DeVoto, J. Pumplin, W.W. Repko and G.L. Kane, Phys. Lett. 90B (1980) 436